Title
The assembly dynamics of a divergent member of the ParM actin-like protein family

Author
Rivera, Christopher Richard

Publication Date
2011

Peer reviewed|Thesis/dissertation

The assembly dynamics of a divergent member of the ParM actin-like protein family

by

Christopher Richard Rivera

DISSERTATION

Submitted in partial satisfaction of the requirements for the degree of

DOCTOR OF PHILOSOPHY

in

Biochemistry and Molecular Biology

in the

GRADUATE DIVISION

of the

UNIVERSITY OF CALIFORNIA, SAN FRANCISCO

Dedications and Acknowledgements

This work could not have been completed without the support and help of many individuals.

I would like to thank Dyche for his enthusiasm about science, support for ideas, and understanding about the difficult things in life.

I would like to thank Ethan Garner and Christopher Campbell for introducing me to the wonders of ParM.

I would like to thank my collaborators, Justin Kollman and Jessica Polka. It was fun working with them.

I would like to thank the great friends that I met throughout graduate school, particularly Jason Huff, Alex Plocik, Mathew Lowse, and Bentley Lim. Without their help and inspiration, I would have never made it through.

I would also like to thank my lab mates; particularly Elena Ingerman, Jennifer Hsiao and Lauren Goins. They made lab fun and are like family.

I would like to thank my best friend, Andrew Chang, for always being there for me.

I would like to thank my parents and sister. I am finally done.

Last, I would like to thank Christine Chen, without her this would have not been impossible.

Abstract

The ParM protein, encoded by the *parMRC* locus from plasmid R1, is the best-characterized actin homolog present in prokaryotes. In conjunction with a nucleoprotein complex formed by a DNA binding protein ParR and a DNA centromere *parC*, ParM constructs a simple mitotic spindle that pushes plasmid DNA to opposite poles of a bacterial cell for DNA segregation. Like actin, ParM assembles into ATP-dependent double-stranded, helical filaments via a nucleation condensation reaction. However, unlike actin, it displays three kinetic properties that are essential to its function: rapid spontaneous nucleation, bilateral elongation and ATPase dependent dynamic instability: the stochastic switching between filament elongation and rapid catastrophic shrinkage. In this dissertation, we investigated three questions related to ParM's evolution and function. First, many divergent R1 ParM homologs are encoded by other plasmids, and function in plasmid DNA segregation. We asked whether the filament architecture and assembly dynamics are conserved in a divergent member of the ParM family, the ParM protein from plasmid pB171. Using microscopic and biophysical techniques, we compared and contrasted the architecture and assembly of these related proteins. Despite being only 41% identical, we find that R1 and pB171 ParM polymerize into nearly identical filaments that display similar assembly dynamics, suggesting that structure and function are conserved in the ParM family. Second, we asked whether ParM prefers ATP or GTP *in vitro*. Using biochemical assays and TIRF microscopy, we find that ParM displays similar polymerization kinetics and stability in the presence of either nucleotide, but binds to ATP ten times tighter than GTP. Third, the structural basis for ParM filament

dynamic instability remains poorly understood. Using cryo-electron microscopy to evaluate ParM filaments, we find that the nucleotide binding pocket of ParM protomers exist in an open or closed state, and that ATP hydrolysis shifts the distribution of protomers states; these findings suggest a mechanism for dynamic instability.

Contributions

The presented in this dissertation was done in collaboration with several people. The work in Chapter 3 was done in collaboration with Justin Kollman and Jessica Polka. Jessica Polka collected electron micrographs of pB171 ParM filaments and Justin Kollman performed the structural analysis. The work in Chapter 4 was done in collaboration with members of the Egelman Lab. Vitold E. Galkinand Albina Orlova performed the electron microscopy and structural analysis in figures 1 and 4-8, and the two supplemental figures. I purified the ParM proteins that were used in the study and performed the biochemical and TIRF microscopy experiments in figures 2 and 3. I also contributed to the discussion of the paper.

Table of Contents

List of tables

Chapter 3

List of figures

Chapter 3

Chapter 4

Chapter 1

Introduction

Eukaryotes and prokaryotes rely on a cytoskeleton to dynamically organize their internal architectures and external shape. The cytoskeleton is composed of polymerizing proteins that assemble into filaments, and accessory factors that regulate them. These filaments serve as dynamic scaffolds that mechanically support the cell, and recruit various components to specific intracellular locations. By acting as tracks for molecular motors and as polymerization-based motors themselves, cytoskeletal filaments generate force used for many cellular processes, such as DNA segregation, intracellular transport and cell division (1-3).

The assembly dynamics of Eukaryotic actin and tubulin

Actin and tubulin are the key cytoskeletal forming proteins in eukaryotes, and each binds nucleotides to assemble into distinct structures with many cellular roles. Actin is one of the most abundant and conserved proteins on the planet, and consists of two globular sub-domains connected by a flexible linker with a central ATP binding cleft (2). Actin assembles into ATP dependent double-stranded helical filaments that function in short range cellular transport, cytokinesis, and amoeboid motility (2). αβ-tubulin dimers assemble into GTP dependent microtubules, which are cylindrical tube-like structures consisting of 13-15 proto-filaments, that function in long-range cellular transport, DNA segregation and flagellar-based motility (1, 4).

Despite having entirely different structures, both actin filaments and microtubules assemble via a three-phase nucleation condensation reaction (5-7). In the first phase, actin and tubulin subunits bind their respective nucleotides. In the next, rate-limiting step, actin and tubulin subunits oligomerize into polymer nuclei, which are the smallest oligomers that can function as filament or microtubule ends. During the elongation phase,

actin filaments and microtubules grow sequentially by single subunit addition to their ends (1, 5-8). In both microtubules and actin filaments, protomers face in the same direction relative to the microtubule/ filament axis. This structural polarity results in kinetic polarity; on end of actin filaments and microtubules grows faster than the other end (1, 9). Both actin filaments and microtubule assembly are governed by a subunit critical concentration, above which they grow and below they shrink (1, 8, 9).

In addition to sharing similar assembly schemes, both microtubule and actin filament disassembly are regulated by nucleotide hydrolysis. Polymerization stimulates actin and tubulin subunits to hydrolyze their bound nucleotide and release phosphate. The resulting ADP/GDP bound protomers undergo conformational changes that destabilize actin filaments and microtubules, resulting in faster depolymerization at ADP/GDP bound ends (1, 10).

As a consequence of nucleotide hydrolysis and differences in the relative rates of growth and shrinkage, actin filaments and microtubules display very different kinetic behaviors. At steady state monomer concentrations, actin filaments treadmill, i.e. one end grows at the same rate that the other end shrinks, whereas, microtubules display dynamic instability, which is the stochastic switching between phases of growth and rapid shrinking (1, 8, 9).

Eukaryotes possess accessory factors that regulate virtually every aspect of actin and tubulin assembly and disassembly. For example, the Arp2/3 and gamma tuRC complexes stimulate actin filament and microtubule nucleation, respectively (4, 11); the VASP and XMAP215 proteins accelerate actin filament and microtubule elongation, respectively; while cofillin and MCACK dismantle them (12-14). Accessory factors also

regulate mechanical the properties of filaments by cross-linking them or arranging them into bundles(2).

Finally, eukaryotic cells use actin filaments and microtubules to generate force in two ways. First, motor proteins, such as myosin and kinesin, use ATP hydrolysis to translocate along filaments and microtubules and move organelles and macromolecular complexes throughout the cell (2, 15). Second, actin filaments and microtubules also generate forces by acting as polymerization and depolymerization based motors (8, 16, 17). By regulating the assembly and disassembly of actin and tubulin, eukaryotic cells can produce a diverse set of biological process.

The prokaryotic cytoskeleton

Because of their small size, and lack of obvious internal organization, twenty years ago, prokaryotes were viewed as 'bags' of enzymes that did not need cytoskeletons. This viewpoint was further justified by phylogenetic searches that failed to identify bacterial actin and tubulin homologs (18). However, extensive work over the past twenty years demonstrates that prokaryotes posses an extensive array of cytoskeletal proteins, including actin and tubulin homologs (3). The first two cytoskeletal proteins indentified in bacteria are FtsZ, a tubulin homolog, and MreB, an actin homolog (19, 20). FtsZ is an essential protein that exist in nearly all prokaryotes, where it forms a ring-like structures, in the middle of cells, that drive cytokinesis (21). Structural and biochemical studies demonstrate that FtsZ has a tubulin-like fold, and assembles into single stranded proto-filaments that hydrolyze GTP (3, 22, 23). Additional electron microscopy studies demonstrate that FtsZ filaments undergo structural changes in their curvature (24), and *in*

vitro reconstitution assays establish that FtsZ filaments generate force that can constrict liposomes (25, 26). Like microtubules and actin filaments, multiple accessory factors, such as FtsA and the minCDE complex, regulate the assembly and disassembly of FtsZ filaments, ensuring that FtsZ only forms cytokinetic rings in the middle of bacterial cells (3).

The actin homolog MreB was first identified as a protein essential for rod shape in *E. coli* (3). Using structure based sequence alignments, in 1992 Bork et al. identified multiple putative actin-like protein in prokaryotes, including MreB and the plasmid encoded ParM(27). Van den Ent et al demonstrated in 2001 that MreB from *T. maritima* possesses an actin-like fold and assembled into actin-like filaments in the presence of ATP, despite sharing very low sequence similarity with Actin (20). *In vivo*, MreB forms short filaments located beneath the cell membrane (28, 29), and controls the shape of rod-shaped bacterial cells; deletion or inhibition of MreB induces rod shaped cells to become spherical and then lyse (3). MreB determines cell shape by controlling the localization and activity of cell wall synthesis machinery (28, 29).

Prokaryotes have also evolved cytoskeletal proteins not present in eukaryotes (3). The ParA Walker box ATPases are the most important of the prokaryotic specific cytoskeletal proteins and function in DNA segregation. They are distantly related to the small signaling GTPases present in eukaryotes, and assemble into filamentous structures on DNA (3, 30). Analogous to the GAPs of small GTPases, ParA nucleoprotein filaments are regulated by specific DNA binding proteins that bind to ParA nucleoprotein filaments and induce ATP hydrolysis and disassembly (31, 32).

Large Low copy Plasmids and ParM

To ensure that are not lost during host cell division, large low copy plasmids evolved three component partitioning loci (*par*) that encode a cytoskeletal NTPase, which forms force generating filaments, and a DNA binding protein that binds to a simple centromere (33). Different *par* loci have co-opted homologs of the three major cytoskeletal NTPases present in bacteria: walker box ATPases (ParA), actin homologs, and tubulin homologs (TubZ) (3).

While *par* loci that encode a ParA protein are the most widespread, the ParM encoding *parMRC* loci from plasmid R1 is the best understood (34). In conjunction with a nucleoprotein complex (the ParRC complex) formed by the DNA binding protein ParR and centromere *parC* (35); ParM assembles a simple mitotic spindle that actively pushes R1 plasmids to opposite cell poles (36). Even though ParM shares only ~13% sequence homology with actin, ParM has an actin-like fold, binds to ATP and forms double stranded actin-like filaments via a nucleation condensation mechanism *in vitro* (27, 37, 38). Although, ParM surprisingly acts like actin, its assembly dynamics display three essential kinetic properties that distinguish it from actin: it nucleates spontaneously 200 times faster than actin, it elongates at equal rates at both ends, and it is dynamically unstable (38).

Garner et al proposed that these kinetic properties are vital to ParM's function and remove its dependence on accessory factors for nucleation and disassembly. Based upon *in vivo* experiments that demonstrated that ParM formed long filaments in cells only when ParR and parC were present, they also postulated that the ParRC complex inhibited dynamic instability of ParM filaments, and that components of the parMRC were sufficient to drive plasmid segregation (38). Reconstitution experiments performed by

Garner et al. demonstrated that ParM filaments can push ParRC coated microspheres, and that the ParRC complex inhibits dynamic instability (39).

Although the general mechanism of DNA segregation by ParM has been "solved" (34), many exciting question exist. Inspired by an interest in polymerization kinetics and the awesome work being done by my lab mates, Ethan Garner and Chris Campbell, I chose to work on several separate problems related to ParM and the function of the *parMRC* system. How has do divergent ParM operate? While, actin is extremely well conserved due to its role in essential cellular processes and its regulation by a plethora of accessory factors (2), ParM has only two interaction partners, itself and the ParRC complex, and one biological role, plasmid segregation (34). Therefore the ParM primary sequence has had free reign to diverge; bioinformatic studies have identified a large number of divergent ParM homologs present in other ParMRC like operons (40). To determine how distantly related ParM homologs assemble into filaments, I chose to study the polymerization kinetics of the ParM protein encoded by *par1* operon of plasmid pB171 (40, 41). These studies are presented in chapter 2. How do different nucleotides affect ParM's assembly dynamics? While Actin and ParM both evolved from simple nucleotide binding proteins, actin evolved the ability to distinguish between ATP and GTP, where as ParM will assemble in both nucleotides (18). Because the nucleotide state is important to filament function, I also investigated how GTP and ATP affect ParM polymerization kinetics. These experiments are presented in chapter 4. What is the structural basis of ParM dynamic instability? I collaborated with members of the Egelman lab and Justin Kollmann from the Agard lab to investigate the effects of nucleotide hydrolysis on both R1 and pB171 ParM filament structure, and these results

are presented in chapter 3 and 4. Finally, what is the kinetic basis of dynamic instability, how does the ParRC complex inhibit dynamic instability, and how does the nucleotide state effect ParM filament mechanics? During my last year of graduate, school I established a single filament assay allowing high-speed visualization of ParM dynamics and single ParM filament interactions with ParRC complex. Preliminary experiments and results are discussed in chapter 5.

References

1. Kueh, H. Y., and Mitchison, T. J. (2009) *Science* **325**, 960–963
2. Pollard, T. D., and Cooper, J. A. (2009) *Science* **326**, 1208–1212
3. Cabeen, M. T., and Jacobs-Wagner, C. (2010) *Annu. Rev. Genet.* **44**, 365–392
4. Aldaz, H., Rice, L. M., Stearns, T., and Agard, D. A. (2005) *Nat Cell Biol* **435**, 523–527
5. Voter, W. A., and Erickson, H. P. (1984) *J Biol Chem* **259**, 10430–10438
6. Tobacman, L. S., and Korn, E. D. (1983) *J Biol Chem* **258**, 3207–3214
7. Flyvbjerg, H., Jobs, E., and Leibler, S. (1996) *Proc Natl Acad Sci USA* **93**, 5975–5979
8. Theriot, J. A. (2000) *Traffic* **1**, 19–28
9. Pollard, T. (1983) *Analytical Biochemistry* **134**, 406–412
10. Belmont, L. D., Orlova, A., Drubin, D. G., and Egelman, E. H. (1999) *Proc Natl Acad Sci USA* **96**, 29–34
11. Mullins, R. D., Heuser, J. A., and Pollard, T. D. (1998) *Proc Natl Acad Sci USA* **95**, 6181–6186
12. Andrianantoandro, E., and Pollard, T. (2006) *Molecular Cell* **24**, 13–23
13. Hansen, S. D., and Mullins, R. D. (2010) *J Cell Biol* **191**, 571–584
14. Howard, J., and Hyman, A. A. (2007) *Current Opinion in Cell Biology* **19**, 31–35
15. Friel, C. T., Bagshaw, C. R., and Howard, J. (2011) *Methods in Molecular Biology* (Straube, A., ed.), Humana Press, Totowa, NJ
16. Kovar, D. R., and Pollard, T. D. (2004) *Proc Natl Acad Sci USA* **101**, 14725–14730
17. Dogterom, M., and Yurke, B. (1997) *Science* **278**, 856–860
18. Popp, D., and Robinson, R. C. (2011) *Mol Microbiol*
19. Erickson, H. P. (1995) *Cell* **80**, 367–370
20. van den Ent, F., Amos, L. A., and Löwe, J. (2001) *Nature* **413**, 39–44
21. Bi, E., and Lutkenhaus, J. (1991) *Nature* **354**, 161–164
22. Erickson, H. P., Taylor, D. W., Taylor, K. A., and Bramhill, D. (1996) *Proc Natl Acad Sci USA* **93**, 519–523
23. Erickson, H. P., Anderson, D. E., and Osawa, M. (2010) *Microbiology and Molecular Biology Reviews* **74**, 504–528
24. Lu, C., and Erickson, H. P. (1999) *Cell Struct Funct* **24**, 285–290
25. Osawa, M., Anderson, D. E., and Erickson, H. P. (2008) *Science* **320**, 792–794
26. Osawa, M., Anderson, D. E., and Erickson, H. P. (2009) *EMBO J* **28**, 3476–3484
27. Bork, P. (1992) *Proceedings of the National Academy of Sciences* **89**, 7290–7294
28. van den Ent, F., Johnson, C. M., Persons, L., de Boer, P., and Löwe, J. (2010) *EMBO J* **29**, 1081–1090
29. Garner, E. C., Bernard, R., Wang, W., Zhuang, X., Rudner, D. Z., and Mitchison, T. (2011) *Science* **333**, 222–225
30. Hui, M. P., Galkin, V. E., Yu, X., Stasiak, A. Z., Stasiak, A., Waldor, M. K., and Egelman, E. H. (2010) *Proceedings of the National Academy of Sciences* **107**, 4590–4595

31. Machón, C., Fothergill, T. J. G., Barillà, D., and Hayes, F. (2007) *J Mol Biol* **374**, 1–8
32. Barillà, D., Carmelo, E., and Hayes, F. (2007) *Proc Natl Acad Sci USA* **104**, 1811–1816
33. Gerdes, K., Møller-Jensen, J., Ebersbach, G., Kruse, T., and Nordström, K. (2004) *Cell* **116**, 359–366
34. Needleman, D. J. (2008) *Curr Biol* **18**, R212–4
35. Møller-Jensen, J., Ringgaard, S., Mercogliano, C. P., Gerdes, K., and Löwe, J. (2007) *EMBO J* **26**, 4413–4422
36. Campbell, C. S., and Mullins, R. D. (2007) *J Cell Biol* **179**, 1059–1066
37. van den Ent, F., Møller-Jensen, J., Amos, L. A., Gerdes, K., and Löwe, J. (2002) *EMBO J* **21**, 6935–6943
38. Garner, E. C., Campbell, C. S., and Mullins, R. D. (2004) *Science* **306**, 1021–1025
39. Garner, E. C., Campbell, C. S., Weibel, D. B., and Mullins, R. D. (2007) *Science* **315**, 1270–1274
40. Gerdes, K., Møller-Jensen, J., and Bugge Jensen, R. (2000) *Mol Microbiol* **37**, 455–466
41. Ebersbach, G., and Gerdes, K. (2001) *Proc Natl Acad Sci USA* **98**, 15078–15083

Chapter 2

Background

Over the past 20-30 years, there has been growing interest in how bacterial plasmids are segregated. Because they are genetically tractable and non-essential to the host cell, plasmids serve as excellent models for understanding the relatively mysterious process of DNA segregation in bacteria (1). Plasmids use simple, three component partitioning systems, which include a filament forming NTPase, to construct mitotic-like apparatuses that are conceptually analogous to the mitotic spindle in eukaryotes, making them intellectually accessible. Furthermore, because the filament forming NTPase include divergent actin and tubulin homologs, studying the assembly dynamics and filament architecture of these homologs provides important insights into the evolution of cytoskeletal systems and into the fundamental problem of how proteins assemble into higher order structures (2-4).

To cope with difficult and changing extra-cellular environments, prokaryotes evolved extra chromosomal plasmids that rely on the host machinery to replicate their genomes and synthesize their proteins. In return, plasmids provide the host cell with new metabolic activities (e.g., protection from metal toxicity, ability to cause disease and resist antibiotics) (5). Unlike small, high copy plasmids which can rely on random assortment for efficient partitioning, large, low copy plasmids cannot and evolved mechanisms to ensure that the plasmid is maintained with in the bacterial host cell population (1). These mechanisms involve toxins that kill bacterial cells that lack the plasmid and elegant cytoskeletal based segregation systems ("partitioning systems") that actively pair, separate and partition plasmids prior to cell division (5).

The partitioning systems are encoded by *par* operons located on the plasmid, which almost always include three components: A small NTPase that acts as a motor protein, a DNA binding adaptor protein, and a simple centromere composed of multiple DNA repeats to which the adaptor protein binds (1). Based on the NTPase structure, par loci are divided into three categories: type I partitioning systems, which encode ParA deviant Walker Box ATPases; type II partitioning systems use actin-like ATPases; and type III partitioning systems employ TubZ tubulin GTPase homologs(2-4).

Although the exact molecular details differ greatly between the three types of *par* loci, they use the similar principles to mediate plasmid partitioning. Multiple dimers of

the DNA binding protein bind to and assemble on the *par* encoded centromere located on plasmids, forming a nucleoprotein complex (known as a segresome or partition complex). The NTPase assembles into filaments in the cytosol or on the host cell nucleoid, and these filaments interact with the segresome. Using nucleotide hydrolysis, the filaments generate pulling or pushing forces that first separate sister plasmids (bound to a segresome) and then moves them to different cellular positions (6).

The rest of the chapter provides background information on the recent research into how these fantastic three component machines function. It includes a discussion on the three partitioning systems with an emphasis on two type I loci, the *parMRC* operon from plasmid R1 and the *par1* operon from plasmid pB171. It ends with a discussion of interesting questions on Type II systems

Type I Partitioning loci:

Type I partitioning operons are the most widespread type of partitioning system and are present on large low copy, plasmids and on bacterial chromosomes, where they are essential for DNA organization and/or segregation (7-9). They encode ParA ATPases that are related to the *Escherichia coli cell division* protein MinD and are members of the WACA super-family of ATPases (3). Type I plasmid partition loci are classified into two subgroups (types Ia and Ia), depending on the structure of their ParA proteins. Type Ia ParA proteins have N-terminal DNA binding domains that they use to bind to and repress transcription from their *par* promoter, whereas type Ib ParA proteins lack this domain (2). With few exceptions, par loci from bacterial chromosomes encode ParA ATPase similar to the type 1b ATPases (2).

The dimeric DNA binding ParB proteins are small (<10 kDa) and are divergent, using a variety of folds to bind specifically to their cognate *parS* sites (10). During partition complex assembly, multiple ParB dimers bind to direct repeats located with in the *parS* centromere (10) and spread beyond the direct repeats, allowing the ParB nucleoprotein complex to silence nearby genes (11). *In vitro*, the ParB protein and partition complex can bind to and stimulate the ATPase activity of ParA proteins (12-14).

The ParA ATPases are thought to serve as ATP dependent-motors that drive separation and segregation of par containing plasmids and chromosomes (1). *In vivo*

microscopy experiments reveal that several ParA homologs assemble into dynamic structures that oscillate from one end of the cell to the other (15-17) . This oscillation appears to be restricted to the nucleoid, depends on ATP hydrolysis and on the presence of ParB and *parS*, and is essential for effective DNA segregation mediated by Type I par loci (15-17). Deletion of either ParB, or parS or mutations of key ATP binding residues in the Walker box ATPase motif results in static ParA filaments, and destabilization of par containing plasmids (15-17).

In vitro experiments demonstrate that ParA proteins dimerize upon ATP binding (18), and that several plasmid encoded ParA homologs assemble into ATP dependent filament bundles with frayed tips at one end *in vitro*, leading to speculation that such bundles may generate force for plasmid partition *in vivo* (12, 19). However, chromosomal ParA homologs do not polymerize into ATP-dependent filaments *in vitro* (3), and recent studies indicate that the ParA oligomeric state is controlled by interactions with DNA. For example, DNA antagonizes filament formation by SopA, a ParA homolog, *in vitro*(12)*;* and substitution of residues implicated in non-specific DNA interactions lead to the improper localization of two ParA homologs *in vivo* and decreased their ability to stabilize plasmids (20). Finally, several plasmid and chromosomal ParA homologs only assemble into dynamic left handed helical filaments on DNA. (21, 22).

Despite the extensive research into their function, the mechanism(s) by which par loci drive DNA segregation remains poorly understood. Type I *par* loci are extremely effective at segregating plasmid and chromosome DNA and localizing their plasmids to quarter cell positions(17, 19). Recent experiments demonstrate that par containing plasmids and chromosomal par loci interact with ParA filaments *in vivo*, and that these loci appear to track with depolymerizing filaments (8, 9, 19, 23). A current model postulates that ParA dimers assemble into multiple nucleoprotein filaments along the nucleoid. The plasmid bound segresome binds to the ParA filaments, and stimulates ATP hydrolysis of ParA protomers. This leads to depolymerization of dimers within the nucleoprotein filaments at the end of filaments, which induces the segresome to undergo a forced 2-D diffusion on the ParA nucleoprotein filaments away from filament depolymerization (24, 25).

TubZ and Type III loci:

Type III loci are the most recently discovered class of plasmid segregation systems, and appear to be restricted primarily to plasmids from Bacillus species (4). These loci, called *tubZR*, utilize two proteins to drive plasmid partitioning (TubR and TubZ) (4, 26). TubR is the DNA binding protein, and TubZ is a divergent member of the tubulin GTPase super-family (4, 26).

TubZ is thought to act as a GTP dependent polymerization motor. When expressed in *B. thuringiensis* and E. coli, TubZ assembles into dynamic filaments that have a critical concentration, and display directional elongation and treadmilling *in vivo* (4). These dynamics rely on GTP hydrolysis and are critical to TubZR functioning; mutating a residue implicated in TubZ GTP hydrolysis stabilizes TubZ filaments *in vivo* and destabilizes *tubZR*-containing plasmids (4). *In vitro* experiments largely corroborate the *in vivo* findings; purified TubZ binds GTP tightly (26) and polymerizes into GTP-dependent two stranded helical filaments and higher order bundles via a nucleation condensation mechanism (27, 28). These filaments rapidly hydrolyze GTP, and are destabilized by GDP (28). Although, single filament dynamics have not been observed, 95% of TubZ protomers are GDP bound, suggesting that individual TubZ filaments are dynamically unstable and are stabilized by a GTP cap, similar to microtubules (28). Interestingly, heterologous expression of TubZ in fission yeast demonstrates that TubZ filament polymerization generates enough force to deform the nuclear membrane of yeast (29).

Like ParB, TubR, by interacting with its cognate centromere, is thought to form a functional segresome. The DNA binding protein TubR binds very tightly to its centromere DNA via a novel winged helix-turn helix (HTH) motif (26). Fluorescence polarization experiments demonstrate that TubR nucleoprotein complex binds to TubZ filaments (26).

How does TubZ mediate plasmid partitioning? A simple model proposed by Ni et al postulates that the TubR partitioning complex binds to dynamically unstable treadmilling TubZ filaments *in vivo*, and that the TubR-DNA complex undergoes a forced 2-D diffusion along the depolymerizing filaments (26). This model suggests how

TubZ polymerization dynamics might be coupled to plasmid movement, but does not address how plasmid are paired and localized to specific locations with in the cell.

Type II partitioning loci, ParMRC and pB171:

Introduction:

The *parMRC* operon is the canonical example of the Type II partitioning loci, and is currently the best understood cytoskeletal based plasmid segregation system. *parMRC* encodes for three components that it uses to construct a mitotic spindle: 1) an actin-like ATPase (ParM) that assembles into force generating filaments that bind to a segresome formed by 2) a DNA binding protein (ParR) and 3) a centromere (*parC*). This section provides a semi-historical discussion focusing on the components of the *parMRC* locus and their function.

History of the ParMRC locus:

The *parMRC* operon is encoded by the large, low-copy multi antibiotic resistance plasmid R1(30). Extensive work during the 1980s determined that plasmid R1 contained a DNA element, originally termed *par*, that stabilized it in bacterial populations(30), and Gerdes et al. physically mapped this par element to a 1.6 kb region located on the R1 plasmid by generating truncated derivative R1 mini plasmids that are completely stable (31). By introducing this region into an unstable plasmid, Gerdes et al also demonstrated that this region was sufficient to stabilize low copy plasmids (31).

Sequencing of the 1.6 kb region identified the parMRC operon and determined that it encoded for 2 genes, ParM and ParR, as well as the upstream *parC* region(32). Additional genetic studies showed that deletion of any of the three components resulted in complete loss of parMRC function and that *ParC* was cis-acting whereas ParM and ParR could work in trans (32).

The ParRC complex forms a ring or clamp like structure?:

The ParRC complex is the best-characterized segresome and is composed of multiple ParR dimers that bind to the *parC* centromere(33). Understanding how it functions and assembles is essential to understanding the *parMRC* partitioning mechanism. This nucleoprotein complex plays several important roles in *parMR*C functioning by: 1) acting as a repressor complex that is essential in auto-regulation of the parMRC locus (34); 2) binding to the ParM filaments and acts as a force coupler that allows ParM to push plasmids (35); and 3) regulating ParM filament dynamics (35).

parC consists of ten 11 base pair repeats that are organized into two sets of five repeats that flank the parMRC promoter(34). *parC* acts as repressor DNA element, and full at *parC* repression requires ParR and all 11 *parC* direct repeats (34). ParR is a small adaptor protein, approximately 13 kDa, that dimerizes and binds cooperatively to *parC* with a ~40 nM affinity. Consistent with *in vivo* observations, the strength of the interaction is dependent on the number of direct *parC* repeats; truncation of *parC* results in a reduction of the apparent affinity.

Oligomerization of ten ParR dimers onto *parC* leads to the formation of the ParRC complex. Electron and atomic force micrographs suggest that the ParRC complex forms a ring-like or boomerang-like structure that is capable of pairing pieces of *parC* containing DNA (36-38). The higher order structure of the R1 ParM complex has yet to be determined, however structural work on the ParR and ParC from plasmid pB171 provides some insights into the R1 ParRC higher order structure. These finding are discussed later in the section on the pB171 *par* I locus.

ParM is a bona-fide actin homolog that forms filaments driving plasmid segregation:

The ParM protein from plasmid R1 is the best-characterized actin homolog in bacteria. When it was originally discovered, due to its low sequence similarity to actin, its role in plasmid DNA segregation was unclear. However, bioinformatic studies performed by Bork et al suggested that ParM might be a member of the Actin-Hsp70-Hexokinase family (39), leading to initial speculation that ParM might form actin-like filaments that could physically separate plasmids (32).

Although the sequence identity is low (<15%), extensive structural and biochemical studies confirmed that ParM is a bona-fide actin homolog. ATP hydrolysis assays demonstrated that ParM is an ATPase, and that its activity is cooperative and stimulated by interactions with ParRC (40). Furthermore, specific mutations in residues in the putative ATP binding pocket of ParM disrupted this activity (40). Electron microscopy, sedimentation and light scattering assays conducted by Moller-Jensen et al established that purified ParM rapidly polymerizes into actin-like filaments in an ATP and magnesium chloride dependent manner (41). Their initial observations also indicated that ParM filaments are highly unstable in ADP and are stabilized by ATPγS (41). X-ray crystallography and additional electron microscopy studies demonstrated that the ParM monomer structure closely resembles the actin monomer structure; it consists of two lobe like domains connected by hinge-like region with a central ATP binding pocket, and assembles in two stranded helical filaments (42).

Extensive cell biological work has also demonstrated that ParM forms dynamic ATP dependent filaments that interact with plasmids in the bacterial cell. Initial immuno fluorescence microscopy conducted by Jensen et al. established that ParM co-localized with parMRC containing plasmids and that this localization was dependent on ParM's ability to bind ATP because mutations in residues in ParM's predicted ATP binding pocket disrupted this co-localization (33). Additional microscopy experiments revealed that ParM forms long filament bundles that run from pole to pole of *E. coli* cells only when ParRC was present, indicating that the ParRC complex somehow modulated ParM's filament dynamics (41). Furthermore, ParM's ATP hydrolysis activity was required for normal filament dynamics and for its ability to segregate plasmid DNA; ParM ATPase mutants, which had decreased ATPase activity, formed long static filaments *in vivo* independent of the presence of ParRC, and *parMRC* locus encoding these mutants failed to stabilize their plasmids (41). Finally, immuno-fluorescence experiments localizing both the parMRC containing plasmids and ParM filaments in fixed cells revealed that ParM filaments were always bound to plasmids at each end *in vivo* (43). Based on the findings, Moller-Jensen et al postulated that ParM assembled into actin-like treadmilling filaments *in vivo*, and separated plasmids by an insertional polymerization mechanism that was dependent on ATP hydrolysis (43).

ParM is dynamically unstable and acts as an efficient segregation motor:

In a groundbreaking paper, Garner et al used FRET based assays and total internal reflection microscopy to study ParM assembly dynamics and made several striking observations. Similar to actin, ParM filaments assemble via a nucleation condensation mechanism characterized by a critical concentration and two kinetic phases which include: a slow phase during which monomers assemble into unstable nuclei and a rapid phase during which filaments elongate by addition of monomers to filament ends (44). However, ParM assembly differed greatly from actin in three important ways. Although, ParM filaments elongate at similar rates as actin filaments, 1) they nucleate 200 times faster than actin filaments, 2) elongate at the same rate at both ends, and 3) are dynamically unstable (44).

Based upon elegant biochemical experiments, Garner et al discovered that ParM dynamic instability is regulated by ATP hydrolysis and is a consequence of a large difference between the relative stability of ATP bound and ADP bound filament ends (44). ParM has a steady-state critical concentration of 2.3 μM in ATP and a critical concentration that is greater than 120 μM in ADP (44). In ATP, individual filaments are short and transient due to dynamic instability, however, polymerization of ParM in non-hydrolysable-AMP-PNP results in long stable filaments (44). By generating an ATPase dead ParM mutant (E148A ParM), Garner et al. confirmed that dynamic instability required ATP hydrolysis as the E148A ParM mutants also form long stable filaments with critical concentration of 0.6 μM (44). Finally, combining sub-stoichiometric concentrations of E148A ParM with wild-type ParM lowered the critical concentration from 2.3 to 0.6 μM, suggesting that ParM filaments had an ATP cap (44).

These observations had several important implications for ParM function *in vivo*. Because ParM nucleated rapidly and was dynamically unstable, it required neither a nucleation nor a disassembly factor *in vivo*. Dynamic instability allowed ParM filaments to efficiently search the bacterial cytoplasm for plasmids, and served as an efficient mechanism to regenerate free monomers for efficient polymerization based force generation. And bilaterally elongating filaments can push in both directions (44).

Based on these results and the observation that ParM filaments always had plasmids bound at their ends *in vivo*, Garner et al. hypothesized that the ParRC complex binding to ParM filaments protected the filaments from catastrophe and allowed them to elongate *in vivo* (44). Based on this hypothesis they generated a model: 1) Rapid, spontaneous nucleation by ParM generates many small filaments throughout the cytoplasm. 2) These filaments undergo dynamic instability and are short lived, unless stabilized at both ends. 3). The ParRC complex binds to filaments ends, and prevents catastrophe only at the ends to which it is bound. 4) Filaments that are bound at one end are longer lived but will eventually depolymerize. 5) At some frequency, individual filaments capture plasmids at both ends. 6) Bilaterally elongating filaments push paired plasmids to opposite cell poles via insertional polymerization. 7) Dynamic instability of non-stabilized filaments provides additional monomer for continuous polymerization. All of the information necessary for *parMRC* mediated plasmid segregation was contained solely in the three components of *parMRC* (44).

In an already classic experiment, Garner et al next directly tested their model by reconstituting ParM driven DNA segregation *in vitro* by incubating ParM with ParRC coated microspheres(35). In the presence of ATP, individual beads formed short ParM filaments asters that grew and shrank from the bead surface. When two beads came in to close proximity, their asters interacted, and formed a long ParM spindle that pushed the beads apart, demonstrating that ParM and the ParRC complex are sufficient to generate force for plasmid segregation. Furthermore, placement of the beads into bacterial chambers demonstrated that the spindles can find the long axis of the chamber via a Brownian ratchet type mechanism (35). Their model also predicted that the center of the ParM filaments should be primarily ADP bound and unstable; laser lysis of the spindles resulted in rapid disassembly proving that the ParRC complex must stabilize each filament end (35). Speckle analysis of the spindles also demonstrated that ParM filaments attached to ParRC complexes elongated via insertional polymerization (35). Additionally, ParRC coated beads formed asters when incubated at ParM concentrations 2.3 μM but greater than 0.6 μM, proving that filaments nucleation occurs at 0.6 μM (35). Finally, when the system was incubated in AMP-PNP rather than ATP, spindles formed

between beads but quickly stalled, indicating that ATP hydrolysis and dynamic instability are required for continuous force generation (35).

Live cell fluorescence microscopy visualizing both plasmids and ParM filaments at the same time further supported their model (45). *In vivo*, individual plasmid clusters developed short ParM asters (45). Interestingly, these asters generate a significant amount of force that is able to propel the plasmid clusters through out the cytoplasm (45). Like the bead assay, ParM spindles formed between plasmid clusters and pushed them to the cell poles at rates that were similar to the ones measure in the bead assay. When the plasmid clusters collided with the cell poles, the ParM spindles would stall and then quickly depolymerize (45). Finally, laser cutting of the spindles also resulted in rapid depolymerization from the cut ends (45).

Taken together, the results indicate that ParM is an actin-like polymerization based motor that uses ATP hydrolysis and dynamic instability to effectively partition plasmids, and that the ParRC components are necessary and sufficient for this activity.

The pB171 plasmid and *par1*; two par operons for the price of one:

Although most work on the mechanism of type II DNA segregation focused primarily on R1 parMRC, many closely related *parMRC*-like operons have been discovered by phylogenetic searches (2). While they share similar a genetic organization and encode homologs of ParM and ParR, there are important differences such as variation in the length and number of the direct centromeric repeats (6). An interesting question is how do these divergent *par* systems function in comparison to *parMRC*? To address this, recent work increasingly focuses on the components of alternate *parMRC*-like loci, one of which is the *par1* operon from plasmid pB171.

The 69-kb pB171 virulence plasmid is important in causing potentially fatal diarrheal illness in young children, and originates from Enteropathogenic *Escherichia coli* (EPEC) (46). Initial sequence analysis indicated that the pB171 plasmid encodes for many genes, including virulence factors, and identified a region containing several operons important for plasmids maintenance, including potential type I and type II par loci and a putative toxin-addiction system (46).

Ensuing work confirmed that the pB171 plasmid has a type II ParM encoding *par* locus (*par1*) and a type I ParA homolog encoding *par* locus (*par2*) that actively segregate the pB171 plasmid (17). These loci are arranged in tandem, and transcribed from opposite DNA strands, and share a central regulatory region containing centromeres that are located in close proximity (17). Plasmid stability assays demonstrate that both *par* loci are functional, and required for complete stability of pB171; separately, *par1* and *par2* stabilized plasmids 15-fold and 180-fold respectively, and together they stabilized plasmids 180-fold, indicating that they function semi-cooperatively in plasmid maintenance (17).

Mechanism of par2 promoter:

Although both *par1* and *par2* are functional, most research on these two loci is focused on *par2* (11, 14, 17, 19, 47). *In vitro*, pB171 ParA binds to ATP, displays cooperative ATPase activity, and forms ATP dependent filamentous bundles that interact with the *par2* segresome (14, 19). Purified pB171 ParB dimerizes and cooperatively binds to its cognate *parS* centromere with high affinity, and is capable of paring *parS* containing DNA molecules (11, 47). ParB and *parS* assemble into a segresome that auto-regulates transcription from the *par2* loci and actively silences the *par1* promoter (11). *In vivo*, ParA forms dynamic oscillating filaments over the nucleoid that actively pulls par2-containing plasmids into well-defined quarter cell positions (11, 15, 17, 19). Consistent with *in vitro* results, ParA filament dynamics and force generation are dependent on ATP hydrolysis, and interactions with the ParBS segresome (24).

The par2 operon:

Similar to *parMRC,* the *par1* operon encodes for a ParM homolog (pB171 ParM), ParR homolog (ParR171) and a parC (parC1) centromere that are essential for partitioning (17). Despite their similar genetic organization, there is significant genetic divergence between the components of the two systems; for example, R1 ParM and pB171 ParM share 41% identity and 52% similarity, and the *parC1* centromere consist of two 10-bp direct repeats, where as R1 parC contains ten 11 bp repeats (17).

All mechanistic work on par1 has focused on ParR protein (ParR171) and its interactions with the *parC1*centromere. Purified ParR binds cooperatively to its cognate parC1 (11) with a kd <0.5 uM (11, 37). Similar to R1 ParRC, the pB171 ParR171C1 complex represses transcription from the par1 promoter *in vivo* (11). Structural work demonstrated that ParR171 forms a dimeric ribbon-helix-helix protein that oligomerizes into a spiraled structure; the outer surface of this structure is positively charged, which implied that DNA wraps around this spiral (37).

The importance of having two partitioning loci and the 'evolution of *par1*':

The pB171 plasmid has two par systems that actively stabilize it. This fact leads to several interesting questions such as: Why does it have two systems? How do they cooperate? And, why is par1 so much less effective at plasmid segregation than *parMRC*?

Other than pB171, very few plasmids encoding two active segregation systems have been discovered (17). Both of pB171's partitioning systems contribute to its stability, suggesting that this arrangement is beneficial to pB171. If this is the case, then why are there so few plasmids that contain two segregation systems? The simplest explanation is that recombination events that result in plasmids that encode two *par* loci occur relatively infrequently. The other, slightly less counterintuitive, reason is that having two segregation systems may actually reduce the overall fitness of the plasmid even if they decrease the plasmids stability.

A plasmids net fitness is a function of several factors that are intrinsic to the plasmid, to the host cell, and to the host cell's environment. Factors that are intrinsic to the plasmid include its replication rate, its mutation rate, and its loss rate. A plasmid may increase its replication rate and decrease its loss rate, however this requires the input of the host cell's metabolic energy; Increasing these rates reduces the host cells reproductive rate, which leads to a decrease in the plasmids fitness. Therefore, in order to enhance their total fitness, plasmids must balance their own needs with that of the (5). Partitioning systems most likely are quite metabolic expensive because they require energy for synthesis of their components and ATP to drive filament dynamics. Therefore, having two partition systems may decrease a plasmids loss rate, but decrease it overall fitness rate.

Still this does not explain why pB171 has two functional *par* Loci. Ringgaard et al. suggest that pB171's arrangement of dual operons is an evolutionary snap shot of one partition system replacing another (11). Because walker box ATPase systems are significantly more effective than ParM based systems, they argue that in time, par1's function will be completely lost, due to either pseudogenization or deletion (11). Indeed, Ringgaard et al.'s observations that par2's ParB silences transcription from the par1 promoter argues that the pB171 plasmid does not even use *par1* in most cells (11). Because par2 is so effective and par1 is typically silent, this has allowed *par1* to undergo genetic drift, resulting in a decrease in par1s function. However, the fact that deletion of *par1* does lead to a decrease in pB171's stability argues that *par1* is at least functional part of the time in part of the bacterial host cell population (17).

Another possibility explaining why pB171 has two *par* loci is that it has sub-functionalized the par loci to cope with changes in the host cell's cellular or external environment. Indeed, work on another plasmid, which encodes both a type I and a type II operon, suggests that the activity of the two par operons is dependent on the type of media and temperature the host cells are grown in. Given that pB171 normally reside in Enteropathogenic E. coli, which due to their nature as a diarrhea causing species, indicates that pB171 must cope with large changes in the host cells external environment (46).

Although, such evolutionary arguments may give insights into how the two systems evolved and how they might function differently depending on the external environment, they do not explain mechanistically why *par1* is so less effective than ParRC at stabilizing plasmids; par2 and parMRC stabilize plasmids 15 and 100 fold respectively. Formally, its reduced effectiveness may be explained by alterations in: 1) ParM filament assembly dynamics or architecture, 2) parR171–*parC* interaction strength, 3) the ParR171C1 complex structure, 4) parR171C1 complex's interaction with pB171 ParM filaments or 5) cellular concentrations of the components. Given that *parC1* has a different genetic architecture and that ParR171's affinity for *parC1* is lower than R1 ParR's affinity for *parC*, the reduction in relative stability of the ParR171C complex is the most obvious explanation. In chapter 3 of this manuscript, I discuss experiments that demonstrate that pB171 ParM assembles into remarkably similar filaments as R1 ParM

using similar assembly kinetics indicating that alteration in pB171 ParM's behavior is unlikely to be the cause of par1's reduced function. To address the exact reason, more experiments must be done.

Important remaining questions and avenues of research on type I par function:

Although, there is a thorough understanding of how type 1 par loci function, many questions remain. This part of the chapter focuses on several areas of important research which include: 1) ParM filament structure and the nature of dynamic stability, 2) ParRC interactions with ParM and the mechanism of inhibition of dynamic instability, 3) the molecular architecture and dynamics of the ParMRC apparatus *in vivo* and 4) other actin based type 1 par loci.

Structure of ParM filaments and the mechanism of dynamic instability:

The structure of ParM filaments is particularly interesting because ParM is distantly related to actin, and builds filaments that loosely resemble actin, yet display bilateral elongation and dynamic instability. To understand how ParM filaments assemble bidirectionally, display dynamic instability and generate force for plasmid movement, we must understand how ParM builds filaments, how ATP hydrolysis changes the architecture of protomers in the filament, and the nature of the filament cap.

The initial work by Van den Ent et al. demonstrated that ParM assembles into ATP-dependent double-stranded helical filaments with a rise and pitch that are similar to actin filaments, despite having very different subunit-subunit interfaces. In that report they also solved the crystal structure ParM without nucleotide and in the presence of ADP, and noted that ADP binding to ParM decreased the angle between ParM's two sub-domains, suggesting that ParM undergoes very large conformational changes that are dependent on its nucleotide state. They also suggested that, like actin filaments, ParM filaments were right handed (42). By generating a ParM reconstruction using the iterative helical real-space reconstruction method on electron micrographs of negatively stained ParM filaments, Orlova et al. demonstrated that contrary to Van den Ent's finding, ParM filaments are left handed (48). Furthermore, ParM filaments display significantly more heterogeneity in their protomers twist than actin (48), which might be attributed to larger conformational changes of ParM protomers upon ATP hydrolysis. Additional work by

Popp et al supported the findings that ParM filaments are left handed, however, they argued that GTP is the nucleotide preferred by ParM, and that this preference led to slight alterations present in the GTP-ParM filaments (49).

In chapter four of this manuscript, I present work that demonstrates that the ParM filament architecture displays more heterogeneity than originally proposed, uses ATP as its preferred substrate, and undergoes large conformational changes due to ATP hydrolysis and phosphate release, conformational changes that give insight into the mechanism of ATP hydrolysis.

ParRC complex interactions with ParM filaments:

Biochemical work established that the ParRC complex binds to ParM filament ends and inhibits catastrophe, and that ParM filaments continue to elongate while bound to the ParRC complex via insertional polymerization (35). Three important questions regarding the ParRC interaction are: How does the ParMRC complex physically interact with ParM filaments, how does ParM move the ParRC complex, and how does the ParMRC complex inhibit dynamic instability?

Recent work on ParMRC interactions with ParM filaments focused on the physical interaction using biochemical and structural methods. Using mutagenesis of ParM and pull downs against the ParRC complex, Salje and Löwe have identified regions in both ParM and ParR that are critical for their interaction indicating that important ParM residues are located on the lateral surface of the ParM filament (50). Electron microscopic studies with unlabeled and gold-labeled ParRC indicated that single ParRC complexes are capable of binding single filaments ends (51).

Two models describe the ParRC-ParM interaction. The first model proposes that the ParRC complex attaches like a clamp to the end of ParM filament, where it rocks back and forth in an ATP hydrolysis dependent fashion to allow monomer addition, similar to how formins are thought to bind to actin filaments (50). ATP hydrolysis and monomer addition at the ParM filament end provide the energy to physically push the complex forward. The second model proposes that the ParRC complex binds like a ring or spiral attached to the side of the filaments, and that it is able to detect conformational

changes in the filament architecture, due to ATP hydrolysis, that bias its diffusion in the direction of new ATP-ParM monomer addition (51).

Both models invoke ParRC interactions with the lateral surfaces of the ParM filament, and therefore explain how the ParRC complex can interact with both filament ends. They also provide strong predictions as two where the ParMRC complex can bind relative to the filament end. In the first model, the ParMRC complex will always bind to the filament end (50), whereas the second model predicts that the ParMRC complex might be able to bind to the middle of the filament when ATP hydrolysis is inhibited by either non-hydrolysable ATP analogs or ATPase dead ParM (51). Experiments performed by Salje and Löwe suggest that polymerizing ParM with AMP-PNP does increase the frequency of ParMRC complex side interactions (50), however Choi et al. did not observe this effect (51).

We have little insight into how the ParRC complex inhibits ParM filament catastrophe. Formally the ParRC complex may inhibit catastrophe by acting as a scaffold that physically prevents depolymerization independent of the nucleotide state of terminal protomers, or it may prevent ATP hydrolysis and phosphate release by protomers that it interacts with. Assays monitoring ATP hydrolysis by ParM polymerized in the presence of the ParRC complex suggested that ParRC increases the rate of ParM ATP hydrolysis (40). However, these experiments were performed with ParM below the ATP critical concentration, therefore the observed increase in ATPase activity might be secondary to filament end stabilization and enhanced polymerization rather than true stimulation of ATPase activity. Many additional experiments must be performed to explore these possibilities.

Nature of the in vivo ParMRC mitotic spindle:

Lastly, How does the ParMRC apparatus work *in vivo?* Does it rely on filament bundles, and how much does ParRC DNA pairing play a role? Rather than functioning as single filament-single ParRC complexes, there is plenty of evidence to suggest that the parMRC mitotic spindle consist of multiple filaments interacting with multiple ParMRC complexes at both ends. Although most TIRF microcopy work has focused on ParM's individual filament assembly dynamics, experiments indicate that ParM does form

bundles *in vitro* and *in vivo* (35, 52, 53) , and that bundle formation is dependent on filament length and the presence of molecular crowders, of which there are plenty in the cytoplasm. Such bundles would increase its ability to interact with ParRC complexes *in vivo* by increasing the persistence length of the filaments and increasing the probability that any individual end in the filament would capture an available ParRC complex.

Similarly, electron microscopy and biochemical work demonstrate that the ParRC complex can pair DNA molecules *in vitro* (38), and plasmid DNA exist as clusters *in vivo*. Since rapid ParM nucleation is likely to form many filaments *in vivo*, to make a functional spindle, the ParRC complex must bind to filaments or filament bundles that interact with a ParRC complex at the other end. Having multiple ParRC complexes in close proximity increases the probability that a free ParRC complex will interact with a filament bound to another ParRC complex at its other end. There are many questions to ask and avenues of research remaining on the ParMRC locus.

Non ParM ALPs involved in plasmid segregation:

Two additional actin-like proteins that are encoded by type II-like *par* operons have been identified, and biochemically and structurally characterized. These proteins, pSK41 ParM and AlfA, are from plasmids present in *S. aureus* and *B. subtilis*, function in plasmid stability and share low sequence similarity with ParM (<20%) (54). pSK41 ParM assembles into non-dynamically unstable, single proto-filaments using different surface interfaces that either ParM or actin, and is more structurally related to the archeal actin from *Thermoplasma acidophilum* (54). AlfA polymerizes into double-stranded, left-handed helical filaments that are very different from ParM and have a large tendency to bundle *in vitro* (55). Like, pSK41 ParM, AlfA is not dynamically unstable. These large differences in filament architecture and filament dynamics indicate strongly suggest that their *par* operons use an entirely different mechanism to segregate plasmids in vivo than *parMRC* (55).

Recent bioinformatic searches by the Pogliano lab have identified thirty-five highly divergent ParM present in prokarya, many of which are encoded by plasmid partitioning operons (56). One of them, Alp7A, appears to form dynamically instable bundles *in vivo*, but more work needs to be done (56). The large discovery of the many

ALPs present on plasmids produces some very tantalizing questions: How do these proteins assemble and what are their filament architectures? How do they mediate plasmid partitioning and interact with their segresome? How did they evolve; was there a single recombination event that led to single par ALP ancestor or have there been multiple recombination events? There are many additional questions that must be answered.

References

1. Gerdes, K., Møller-Jensen, J., Ebersbach, G., Kruse, T., and Nordström, K. (2004) *Cell* **116**, 359–366
2. Gerdes, K., Møller-Jensen, J., and Bugge Jensen, R. (2000) *Mol Microbiol* **37**, 455–466
3. Cabeen, M. T., and Jacobs-Wagner, C. (2010) *Annu. Rev. Genet.* **44**, 365–392
4. Larsen, R. A., Cusumano, C., Fujioka, A., Lim-Fong, G., Patterson, P., and Pogliano, J. (2007) *Genes Dev* **21**, 1340–1352
5. Paulsson, J., and Ehrenberg, M. (2001) *Q Rev Biophys* **34**, 1–59
6. Schumacher, M. A. (2008) *Biochem J* **412**, 1–18
7. Lee, P. S., and Grossman, A. D. (2006) *Mol Microbiol* **60**, 853–869
8. Saint-Dic, D. (2006) *J Bacteriol* **188**, 5626–5631
9. Ptacin, J. L., Lee, S. F., Garner, E. C., Toro, E., Eckart, M., Comolli, L. R., Moerner, W. E., and Shapiro, L. (2010) *Nature Publishing Group* **12**, 791–798
10. Fothergill, T., Barilla, D., and Hayes, F. (2005) *J Bacteriol* **187**, 2651
11. Ringgaard, S., Ebersbach, G., Borch, J., and Gerdes, K. (2007) *J Biol Chem* **282**, 3134–3145
12. Bouet, J.-Y., Ah-Seng, Y., Benmeradi, N., and Lane, D. (2007) *Mol Microbiol* **63**, 468–481
13. Barillà, D., Carmelo, E., and Hayes, F. (2007) *Proc Natl Acad Sci USA* **104**, 1811–1816
14. Machón, C., Fothergill, T. J. G., Barillà, D., and Hayes, F. (2007) *J Mol Biol* **374**, 1–8
15. Ebersbach, G., and Gerdes, K. (2004) *Mol Microbiol* **52**, 385–398
16. Ebersbach, G., and Gerdes, K. (2004) *Mol Microbiol* **52**, 385–398
17. Ebersbach, G., and Gerdes, K. (2001) *Proc Natl Acad Sci USA* **98**, 15078–15083
18. Barillà, D., Rosenberg, M. F., Nobbmann, U., and Hayes, F. (2005) *EMBO J* **24**, 1453–1464
19. Ebersbach, G., Ringgaard, S., Møller-Jensen, J., Wang, Q., Sherratt, D. J., and Gerdes, K. (2006) *Mol Microbiol* **61**, 1428–1442
20. Castaing, J.-P., Bouet, J.-Y., and Lane, D. (2008) *Mol Microbiol*, 12
21. Pratto, F., Cicek, A., Weihofen, W. A., Lurz, R., Saenger, W., and Alonso, J. C. (2008) *Nucleic Acids Research* **36**, 3676–3689
22. Hui, M. P., Galkin, V. E., Yu, X., Stasiak, A. Z., Stasiak, A., Waldor, M. K., and Egelman, E. H. (2010) *Proceedings of the National Academy of Sciences* **107**, 4590–4595
23. Fogel, M. A., and Waldor, M. K. (2006) *Genes Dev* **20**, 3269–3282
24. Ringgaard, S., van Zon, J., Howard, M., and Gerdes, K. (2009) *Proc Natl Acad Sci USA* **106**, 19369–19374
25. Vecchiarelli, A. G., Han, Y.-W., Tan, X., Mizuuchi, M., Ghirlando, R., Biertümpfel, C., Funnell, B. E., and Mizuuchi, K. (2010) *Mol Microbiol*, no–no
26. Ni, L., Xu, W., Kumaraswami, M., and Schumacher, M. A. (2010) *Proceedings of the National Academy of Sciences* **107**, 11763–11768
27. Aylett, C. H. S., Wang, Q., Michie, K. A., Amos, L. A., and Löwe, J. (2010)

Proceedings of the National Academy of Sciences **107**, 19766–19771
28. Chen, Y., and Erickson, H. P. (2008) *J Biol Chem* **283**, 8102–8109
29. Srinivasan, R., Mishra, M., Leong, F. Y., Chiam, K.-H., and Balasubramanian, M. (2011) *Cytoskeleton (Hoboken)*
30. Nordström, K., and Molin, S. (1980) *Plasmid*
31. Gerdes, K., and Larsen, J. (1985) *J Bacteriol*
32. Dam, M., and Gerdes, K. (1994) *J Mol Biol* **236**, 1289–1298
33. Jensen, R. B., and Gerdes, K. (1999) *EMBO J* **18**, 4076–4084
34. Jensen, R. B., Dam, M., and Gerdes, K. (1994) *J Mol Biol* **236**, 1299–1309
35. Garner, E. C., Campbell, C. S., Weibel, D. B., and Mullins, R. D. (2007) *Science* **315**, 1270–1274
36. Hoischen, C., Bussiek, M., Langowski, J., and Diekmann, S. (2008) *Nucleic Acids Research* **36**, 607–615
37. Møller-Jensen, J., Ringgaard, S., Mercogliano, C. P., Gerdes, K., and Löwe, J. (2007) *EMBO J* **26**, 4413–4422
38. Jensen, R. B., Lurz, R., and Gerdes, K. (1998) *Proc Natl Acad Sci USA* **95**, 8550–8555
39. Bork, P. (1992) *Proceedings of the National Academy of Sciences* **89**, 7290–7294
40. Jensen, R. B., and Gerdes, K. (1997) *J Mol Biol* **269**, 505–513
41. Møller-Jensen, J., Jensen, R. B., Löwe, J., and Gerdes, K. (2002) *EMBO J* **21**, 3119–3127
42. van den Ent, F., Møller-Jensen, J., Amos, L. A., Gerdes, K., and Löwe, J. (2002) *EMBO J* **21**, 6935–6943
43. Møller-Jensen, J., Borch, J., Dam, M., Jensen, R. B., Roepstorff, P., and Gerdes, K. (2003) *Molecular Cell* **12**, 1477–1487
44. Garner, E. C., Campbell, C. S., and Mullins, R. D. (2004) *Science* **306**, 1021–1025
45. Campbell, C. S., and Mullins, R. D. (2007) *J Cell Biol* **179**, 1059–1066
46. Tobe, T., Hayashi, T., Han, C. G., Schoolnik, G. K., Ohtsubo, E., and Sasakawa, C. (1999) *Infect Immun* **67**, 5455–5462
47. Ringgaard, S., Löwe, J., and Gerdes, K. (2007) *J Biol Chem* **282**, 28216–28225
48. Orlova, A., Garner, E. C., Galkin, V. E., Heuser, J., Mullins, R. D., and Egelman, E. H. (2007) *Nat Struct Mol Biol* **14**, 921–926
49. Popp, D., Narita, A., Oda, T., Fujisawa, T., Matsuo, H., Nitanai, Y., Iwasa, M., Maeda, K., Onishi, H., and Maéda, Y. (2008) *EMBO J* **27**, 570–579
50. Salje, J., and Löwe, J. (2008) *EMBO J* **27**, 2230–2238
51. Choi, C. L., Claridge, S. A., Garner, E. C., Alivisatos, A. P., and Mullins, R. D. (2008) *J Biol Chem* **283**, 28081–28086
52. Salje, J., Zuber, B., and Löwe, J. (2009) *Science* **323**, 509–512
53. Popp, D., Narita, A., Iwasa, M., Maéda, Y., and Robinson, R. C. (2010) *Biochem Biophys Res Commun* **391**, 1598–1603
54. Popp, D., Xu, W., Narita, A., Brzoska, A. J., Skurray, R. A., Firth, N., Goshdastider, U., Maeda, Y., Robinson, R. C., and Schumacher, M. A. (2010) *Journal of Biological Chemistry* **285**, 10130–10140
55. Polka, J. K., Kollman, J. M., Agard, D. A., and Mullins, R. D. (2009) *J Bacteriol* **191**, 6219–6230
56. Derman, A. I., Becker, E. C., Truong, B. D., Fujioka, A., Tucey, T. M., Erb, M. L.,

Patterson, P. C., and Pogliano, J. (2009) *Mol Microbiol* **73**, 534–552

Chapter 3

Architecture and assembly of a divergent member of the ParM family of bacterial actin like proteins

Christopher R. Rivera, Justin M. Kollman, Jessica K. Polka, David A. Agard, and R. Dyche Mullins

Published: Journal of Biological Chemistry. Vol 286(16):14282-14290. April 22, 2011

Summary

Eubacteria and archaea contain a variety of actin-like proteins (ALPs) that form filaments with surprisingly diverse architectures, assembly dynamics, and cellular functions. While there is much data supporting differences between ALP families, there is little data regarding conservation of structure and function within these families. We asked whether the filament architecture and biochemical properties of the best-understood prokaryotic actin, ParM from plasmid R1, are conserved in a divergent member of the ParM family from plasmid pB171. Previous work demonstrated that R1 ParM assembles into filaments that are structurally distinct from actin and the other characterized ALPs. They also display three biophysical properties thought to be essential for DNA segregation: (1) rapid spontaneous nucleation, (2) symmetrical elongation, and (3) dynamic instability. We used microscopic and biophysical techniques to compare and contrast the architecture and assembly of these related proteins. Despite being only 41% identical, R1 and pB171 ParMs polymerize into nearly identical filaments with similar assembly dynamics. Conservation of the core assembly properties argues for their importance in ParM-mediated DNA segregation and suggests that divergent DNA-segregating ALPs with different assembly properties operate via different mechanisms.

Introduction

Prokaryotes were long believed to lack cytoskeletons, but recent work demonstrates that eubacteria and archaea use actin-like filaments, tubulin-related polymers, and intermediate filaments to control cellular shape (1), divide (2), establish order in the cytoplasm (3,4), and move intracellular cargo (5). To understand the evolution of these bacterial cytoskeletal systems, we must understand both their diversity and the structural and functional relationships between them. A recent sequence analysis (6) identified forty-one families of actin-like proteins (ALPs) in eubacteria and archaea. Seven are known to form filaments, and their functions include controlling cell wall synthesis (MreB) (7), segregating DNA (ParM, AlfA, Alp7A, pSK41 ParM) (6,8-10), and aligning organelles (MamK) (3,4). Five ALPs, MreB, ParM, Ta0583, AlfA, and Psk41 ALP, have been studied *in vitro* (11-15). Their architectures and dynamics differ significantly from each other and from conventional actin *in vitro* (11,14-16). A paradigm emerging from this work is that, unlike the eukaryotic actin cytoskeleton, whose architecture and function are determined by accessory factors, each bacterial actin appears adapted to a specific function, with unique properties that reduce its need for accessory factors.

Given the diversity of the ALPs, we asked whether the biochemical properties we proposed to be important for the cellular function of one actin-like-protein, ParM from the R1 plasmid, are conserved across the entire ParM family. R1 ParM is the best understood bacterial actin (17), and it drives plasmid segregation in gram-negative enteric

pathogens by forming a polymerization-based motor (10,18) that pushes plasmids to opposite poles of rod-shaped cells (19). We previously identified three properties that appear to be essential to ParM's cellular function and reduce its requirement for accessory factors. These properties are (1) a stochastic switch between growth and shrinking, called dynamic instability, (2) symmetrical filament elongation, and (3) rapid spontaneous nucleation (18,20).

Two recently characterized bacterial ALPs assemble into structures that look very different from both ParM and conventional actin filaments. The first, an ALP from plasmid pSK41, was initially identified as a potential member of the ParM family (10). Its sequence similarity to R1 ParM (18%), however, is below the 20% cutoff proposed by Derman et al. for defining ALP families (6) and its atomic structure appears more closely related to that of an archeal actin, Ta0583, from *T. acidophilum*. Perhaps not surprisingly, pSK41 ALP assembles into filaments with strikingly different architecture and assembly dynamics than R1 ParM; it forms one-strand helical filaments, which are very different from the two-stranded R1 ParM filaments. Nucleation of these filaments is slower than that of R1 ParM and elongation proceeds from a dimeric, rather than a trimeric, nucleus. Finally, and most interestingly, the pSK41 ALP filaments are not dynamically unstable (15).

The second ALP, AlfA, is also a plasmid-segregating actin with little sequence homology to R1 ParM (15% identity). It also forms unique filaments that bundle spontaneously and lack dynamic instability (14). These findings, especially the differences in polymer assembly dynamics, invite the intriguing conclusion that different ALP families partition plasmid DNA via distinct mechanisms. These results also suggest

an important question: How well conserved are the biochemical and biophysical properties of more closely related ALPs, especially since individual ALP families can be more diverse than the entire family of eukaryotic actins?

To address this question, we purified and characterized an actin-like protein encoded by the StbA gene from the Par1 operon of plasmid pB171 from Enteropathogenic *Escherichia coli* (21,22). R1 ParM and pB171 StbA share 41% identity and 52% similarity. Since this level of conservation is within the cutoff proposed by Derman et al. for prokaryotic ALP families we will refer to StbA as pB171 ParM. This level of conservation is, however, weak compared to that of eukaryotic actins and is more characteristic of the conservation between conventional actin and the eukaryotic actin related proteins (ARPs), which have different activities and cellular functions (23). Using time-resolved light scattering, as well as electron and TIRF microscopy of single filaments, we asked whether the structure and basic biophysical properties of R1 ParM are conserved in pB171 ParM.

Experimental Procedures

Cloning, Expression and Purification-

We PCR amplified the pB171 ParM gene from a mini pB171 plasmid with primers that appended a C-terminal GSKCK tag for later use in maleimide labeling reactions and cloned it into a pET-11a vector (NEB, Ipswich, MA). We transformed *E. coli* BL21 cells with the construct, grew them at 37° C to an optical density of 0.7 at 600 nm and induced with 0.75 mM isopropyl-β-D-thiogalactopyranoside for 3-5 hours. We harvested bacterial pellets via centrifugation and flash froze them in liquid N_2. We purified pB171 ParM-GSKCK using the same protocol as for R1 ParM (20) with the following modification: a 0-20% ammonium cut was used to precipitate the pB171 ParM protein out of the clarified bacterial extract as the initial purification step. R1 ParM-GSKCK was expressed and purified as previously described (20).

Electron Microscopy and Image Analysis-

pB171 and R1 ParM were polymerized with 5 mM nucleotide for 5 minutes, then prepared by negative staining as described (24)**.** Samples were imaged on a Tecnai T12 microscope operating at 120 kV at 62,000X magnification. Images were recorded on a Gatan Ultrascan 4k x 4k CCD camera, at a pixel size of 1.72 Å. The defocus of each micrograph was determined using CTFFIND (25), and the entire micrograph was corrected by phase flipping.

Three-dimensional reconstructions of both pB171 and R1 ParM were performed by iterative helical real space reconstruction, as described (26). A total of 5006 pB171 ParM

filament segments 260Å in length were used in an initial reconstruction. Heterogeneity of the helical symmetry within the dataset was sorted by comparison to a series of references with different helical symmetries, as described for R1 ParM (27). The largest class from this analysis, corresponding to particles with an azimuthal angle of 166.2º, had 1111 helical segments. This class was used in an independent reconstruction, yielding the final structure at 19 Å resolution. The R1 ParM reconstruction used 4799 helical segments, and did not require classification by helical symmetry.

High Speed Sedimentation Assays-

We combined various concentrations of pB171 ParM with 10 mM nucleotide in buffer F (100 mM KCl, 30 mM Tris-HCl pH 7.5, 1 mM $MgCl_2$, 1 mM DTT). For experiments with ATP and GTP, an additional 10 mM $MgCl_2$ was added to the reactions. The reactions were then immediately centrifuged for 15 minutes at 355000 x g at 25° C in a TLA 120.1 rotor. The supernatants were resolved on 4-12% pre-cast gradient NuPage acrylamide gels (Invitrogen, Carlsbad, CA) or on self-cast 13.75% SDS poly acrylamide gels. The gels were stained with SYPRO Red (Invitrogen), scanned with a Typhoon 9400 variable mode imager (GE Healthcare Life Sciences, Uppsala, Sweden), and quantified using ImageQuant TL software (GE Healthcare Life Sciences). The steady state monomer concentration was estimated as the x-intercept of lines fit to a plot of the calculated amount of protein in the pellet versus the total initial protein.

Etheno-ATP Binding And Nucleotide Competition Assays-

Dissociation rate constant: Reaction mixtures containing equimolar pB171 ParM and 1,N6-etheno-ATP (Invitrogen) in buffer Q (100 mM KCl, 30 mM Tris-HCl pH 7.5, 1 mM $MgCl_2$, 1 mM DTT, 200 mM acrylamide) were incubated for 15 minutes at room

temperature, and then combined with equal volumes of 10 mM ATP in buffer Q using a SFA-20 rapid mixer (Hi-tech, Bradford-on-Avon, UK). We monitored the fluorescence at 420 nm (ex: 315 nm) over time with a K2 fluorimeter (ISS, Champagne, IL) and fit exponential decay functions to the data to estimate the dissociation rate constant.

Association rate constant: We mixed equal volumes of 1 μM pB171 ParM in with a range of concentrations of etheno-ATP in buffer Q using the rapid mixer and recorded the fluorescence over time. The observed rate constants were estimated by fitting exponential rise functions to the data and plotted versus the etheno-ATP concentrations. The slope of a line fit to the plot estimated the association rate constant (k_{on}) and the y-intercept provided a second estimate of the disassociation rate constant (k_{off}).

Affinity constants (K_d): A 1.6 μM ParM-etheno-ATP-buffer Q solution was mixed with equal volumes of a range of concentrations of ATP and GTP. Following a 15-minute incubation at room temperature; the fluorescence of the individual reaction mixtures was measured. We fit a 4-parameter logistic function to a plot of the percentage of relative binding versus the concentration of competitor nucleotide to estimate the IC_{50} and converted the IC_{50} values to a K_i using the online IC_{50} to Ki converter tool at http://botdb.abcc.ncifcrf.gov/toxin/kiConverter.jsp(28).

Bulk Polymerization And Phosphate Release Assays-

For the bulk polymerization assays, we rapidly mixed a range of concentrations of pB171 ParM with equal volumes of 10 mM $MgCl_2$-ATP or $MgCl_2$-GTP in buffer F and recorded the right angle light scattering intensity over time with an excitation wavelength of 314 nm. Each trace for a particular concentration is the average of 5 or more runs performed on the same day. For the assays with varied nucleotide, we rapidly mixed 10

μM pB171 ParM in buffer F with equal volumes of a dilution series of ATP or GTP and recorded the right angle light scattering over time. We measured phosphate release by 5 uM ParM polymerized with ATP or GTP in buffer F using the EnzChek Phosphate assay kit (Invitrogen) with an Ultrospec 2100 Pro specto-photometer controlled with SWIFT II software (GE Healthcare Life Sciences). A360 values were converted to inorganic phosphate concentration by using a phosphate standard and parallel right angle light scattering assays were performed on the same day.

pB171 ParM Labeling And TIRF Microscopy-

For labeling reactions, monomeric pB171 ParM was combined with Alexa-488-maleimide (Invitrogen) at a 1:1.6 molar ratio in buffer F lacking DTT for 30 minutes at 4°C. The reactions were quenched by the addition of 10 mM DTT, and the protein was separated from free dye by gel filtration. The labeling efficiency was 80-100%.

To monitor single filament polymerization dynamics, we directly applied 2.7 μL of 25% Alexa-488-labeled pB171 ParM in TIRF buffer (100 mM KCl, 15 mM Tris-HCl, 1 mM $MgCl_2$, 1 mM DTT, 0.8% methyl-cellulose, 0.5% BSA) and 0.3 μL of 100 mM ATP or AMP-PNP to ethanol-base washed cover slips and performed time-lapse TIRF microscopy using a Nikon Eclipse TE2000-E inverted microscope equipped with an Andor iXon + EM digital camera and a 40-mW 488/514 argon ion laser. Data were analyzed with Image J (29).

Sequence alignments and Phylogenetic analysis-

Representative actin and ParM sequence were identified using Blast-p at NCBI. The sequences were aligned using the MUSCLE global alignment algorithm (30) and

Jalview alignment editor (31). Phylogenetic analysis was performed with the MEGA4 software (32) using the Neighbor joining (33) and Bootstrap (34) methods.

Results

Comparing the structures of R1 and pB171 ParM filaments.

Using electron microscopy, we examined negatively stained pB171 ParM filaments polymerized with AMP-PNP, ATP, and GTP. Under all conditions, we observed well-separated, helically wound filaments composed of two strands (Fig. 1A, B, and C). Filaments formed in AMP-PNP (Fig. 1A) were longer than those formed in either ATP or GTP (Fig. 1B and C).

Initial attempts to construct a high-resolution model of pB171 ParM filaments in AMP-PNP using iterative helical real space reconstruction (IHRSR) (26) failed to converge to a stable solution, even after 60 refinement cycles (Fig. S1B). In contrast, R1 ParM filaments assembled in AMP-PNP yielded a stable solution after ~20 iterations (Fig. S1A). The helical twist of R1 ParM filaments has been shown to be somewhat variable (16,27) and we interpret the failure of pB171 ParM images to produce a stable reconstruction as evidence that the variation in angles between protomers in these filaments is even higher.

To deal with these heterogeneities, we performed multi-reference classification of the data set using nine models with different helical symmetries. The largest class, which contained 20% of the entire data set, corresponded to an azimuthal rotation of 166.1° between adjacent protomers. In an independent reconstruction performed using only this class of the data, helical symmetry converged from different initial values to the same solution after ~10 iterations. Following initial convergence, however, the azimuthal

rotations oscillated between 166.0° and 166.25° in subsequent iterations, suggesting some degree of twist heterogeneity even within this class (Fig. S1C). The final structure of pB171 ParM, with an estimated resolution of 19 Å (Fig. S1D), closely resembles both the present and previously reported structures of AMP-PNP R1 ParM filaments (27) (Fig. 2A).

We fit the atomic structure of ADP-bound R1 ParM (12) into our pB171 ParM AMP-PNP reconstruction without steric clashes. The inter- and intra-strand contacts between protomers are nearly identical to the model of Galkin et al (27) (Fig. 2C).

Nucleotide binding and sedimentation assays demonstrate that pB171 ParM binds more tightly to ATP, but is more stable in GTP.

We determined the distribution of pB171 ParM between monomeric and polymeric states using high-speed centrifugation. Similar to other actin-like proteins, assembly of pB171 ParM into filaments required nucleotide triphosphates (either ATP or GTP) and was promoted by $MgCl_2$. ATP-ParM polymerization was reduced in the absence of added $MgCl_2$ and inhibited by 1 mM EDTA. Like other actin-like proteins, pB171 ParM polymerized poorly in the presence of $CaCl_2$. A larger fraction of the pB171 protein pelleted in GTP than ATP in all conditions except buffer containing $CaCl_2$. In this condition, pelleting was identical in ATP and GTP (Fig. S2A and SB).

Actins and the prokaryotic ALPs studied to date bind to and polymerize in the presence of ATP and GTP with varying efficiencies (13-15,27,35-37). Stopped-flow experiments indicate that pB171 ParM binds the fluorescent ATP analog, 1,N6-etheno-ATP with a rate constant of 25.8 ± 1.1 $x10^3$ $s^{-1}M^{-1}$ and the pB171 ParM-etheno-ATP complex disassociated with a rate constant of 0.368± 0.142 s^{-1}, corresponding to a K_d of

14.2±5.5 μM (Fig. 3A). Competition binding experiments between etheno-ATP and either ATP or GTP indicated that pB171 ParM has a significantly higher affinity for ATP (K_d=2.7±1.2 μM) than GTP (K_d=114.4±33.4 μM) (Fig. 3B). Assuming intracellular ATP and GTP concentrations of 9.4 and 4.9 mM, respectively, (38) and ignoring the presence of other nucleotide binding proteins, the measured affinities suggest that, *in vivo*, 98.8% of pB171 ParM is bound to ATP and 1.2% is bound to GTP.

For quantitative comparison of cytoskeletal polymers, we will define three terms: critical concentration, steady-state monomer concentration, and instability ratio. We define a critical concentration only for single-state polymers. Briefly, if polymer assembly is governed by:

$$dP/dt = k_+[m][e] - k_-[e]$$

Where k_+ and k_- are rate constants for monomer association and dissociation and [m] and [e] are concentrations of monomer and filament ends, then the critical concentration is defined as the monomer concentration at which polymer neither grows nor shrinks:

$$[m] = \frac{k_-}{k_+} \qquad (1)$$

Although R1 ParM is normally a two-state (dynamically unstable) polymer, we can convert it into a one-state polymer using point mutants or non-hydrolysable nucleotide analogs. Under either condition, R1 ParM has a critical concentration (0.6 μM) governed by equation (1). We will call this the ATP critical concentration (m_{cc}^{ATP}). R1 ParM is unstable in ADP and has an ADP critical concentration (m_{cc}^{ADP}) greater than 120 μM. Wild type R1 ParM filaments in the presence of ATP can switch from stable elongation

to rapid de-polymerization, and the measured steady state monomer concentration under these conditions is 2.3 μM. Since this monomer concentration reflects the behavior of two filament populations, each with a different critical concentration, we will refer to it simply as the steady-state monomer concentration (m_{ss}) of the polymer. If we assume that the reason m_{ss} is greater than m_{cc}^{ATP} is because at steady state some fraction of filaments (r) have ATP caps at their ends and are governed by Eqn. 1, while the rest (1-r) have ADP-bound protomers at one or both of ends and are catastrophically shortening at a rapid rate (k_s), then the steady state monomer concentration is given by:

$$[m_{ss}] = \frac{k_-}{k_+} + \frac{k_s}{k_+}\left(\frac{1}{r} - 1\right) \qquad (2).$$

Using parameters measured for R1 ParM we calculate that, at steady state, 88% of filaments are stable and 12% are shrinking.

Finally, for polymers whose stability changes upon nucleotide hydrolysis, the ratio of the critical concentration in nucleotide diphosphate (ADP or GDP) over that in nucleotide tri-phosphate (ATP or GTP) is a convenient measure of dynamic instability. We will call this the 'instability ratio' of the polymer. For example, actin, which is not generally considered dynamically unstable, has an instability ratio of 1.6 (39). AlfA, which segregates DNA in Bacillus cells, has a similar instability ratio of 4.2 (14). In contrast, dynamically unstable R1 ParM filaments have an instability ratio greater than 160 (20).

Finally, sedimentation assays indicated that pB171 ParM has a lower steady-state monomer concentration in GTP (m_{ss}^{GTP}=1.1±0.21 μM) than in ATP (m_{ss}^{ATP} 1.5±0.12 μM). We find that like R1 ParM, pB171 ParM has an instability ratio greater than 140 (Table 1), in both adenosine and guanosine nucleotides.

Rapid nucleation and nucleotide hydrolysis by pB171 ParM.

For linear helical polymers such as actin and R1 ParM, filament assembly is governed by several parameters that include nucleus size, nucleation rate, elongation rate, stability of the polymer in sub-saturating nucleotide, and rates of nucleotide hydrolysis and phosphate release. By right angle light scattering, pB171 ParM rapidly assembles in the presence of ATP, suggesting that nucleation is fast. The ATP-pB171 ParM assembly curves have three phases: an initial increase in polymer, followed by a brief decrease, and then a slower approach to steady state (Fig. 4A). pB171 ParM also rapidly assembled in GTP (Fig. 4B). However, the traces lacked the middle phase observed in ATP.

To estimate the nucleus size and nucleation rate, we plotted the intensity-normalized maximum polymerization rate versus the protein concentration on a log-log plot and fit a line to the transformed data (14,20,40). Using this method, we estimate that the size of the nucleus, the last unstable intermediate in the filament assembly pathway, for pB171 ParM filaments is a dimer in ATP and GTP (Fig. 4C). In contrast, assembly of actin and R1 ParM begins with creation of a trimeric nucleus (20,41). Overall, our analysis indicates that pB171 ParM filaments assemble spontaneously much more quickly than actin filaments.

We also used the method of Flyvbjerg et al. (42) to estimate the nucleus size from early time points of our light scattering data. We normalized the amplitudes and times of light scattering curves collected at different concentrations of pB171 ParM and observed that all the ATP data collapsed on to one curve. The GTP data collapsed onto a similar curve, indicating that pB171 ParM assembles via the same mechanism in ATP and GTP (Fig. 4D), but with different rate constants. To estimate the nucleus size, we plotted the

normalized data for the earliest time points on log-log plots. The slope for the earliest time points reflects the number of kinetic steps in nucleation (42). This analysis indicated that nucleus formation occurs in one step in both ATP and GTP further indicating that the pB171 ParM nucleus is a dimer (Fig. S3).

To determine pB171 ParM's stability in limiting concentrations of nucleotide, we polymerized 10 μM ParM in the presence of varying concentrations of ATP and GTP. Following an initial rapid polymerization, pB171 ParM filaments de-polymerized when assembled in limiting concentrations of ATP and GTP (Fig. 5A and 5B). Consistent with our measurements of nucleotide affinity, the initial rates of pB171 ParM polymerization were more sensitive to limiting concentrations of GTP than ATP (Fig. S4E and S4F). These data also suggest that pB171 ParM filaments are more stable in GTP than ATP, because the rate of decay in 40 μM ATP was faster than the rate of decay in 40 μM GTP (Fig. S4G). Similar results were obtained for pB171 ParM polymerized with various concentrations of $MgCl_2$-ATP and $MgCl_2$-GTP (Fig. S4A, S4B, S4C and S4D).

Phosphate release assays indicated that phosphate production lagged behind polymerization in low (0.1 mM) and high (1mM) concentrations of ATP and GTP (Fig. 5C-F) Surprisingly, we observed similar rates of phosphate production in 1 mM ATP (0.577 ± 0.001 μM/s) and 1 mM GTP (0.593 ± 0.006 μM/s) at steady state. Consistent with the difference in measured affinities, steady state pB171 ParM phosphate production was greater in ATP (0.513 ± 0.017 μM/s) than GTP (0.445 ± 0.09 μM/s) at 0.1 mM nucleotide concentrations.

TIRF microscopy of individual filaments confirm that pB171 ParM elongates symmetrically, is dynamically unstable, and that nucleotide hydrolysis is required for dynamic instability.

Using time-lapse TIRF microscopy to monitor individual filaments of 25% Alexa-488 labeled ParM polymerized in ATP, we observed many short individual filaments that diffused rapidly, binding only transiently to the cover glass before detaching. However, all filaments that remained attached to the cover slip surface for an extended period elongated symmetrically from both ends prior to undergoing catastrophic de-polymerization, which appeared to occur primarily from one end. No rescue events were observed; all filaments that we tracked either detached from the slide or completely de-polymerized. We measured the rates of filament elongation (10.6 +/ 4.9 monomers/s) and de-polymerization following catastrophe (22.9 ± 9.4 monomers/s) (Fig. 6A and 6B), which are similar to those we previously measured for R1 ParM (20).

To determine whether nucleotide hydrolysis regulates dynamic instability in pB171 ParM, we performed TIRF microscopy on various concentrations of pB171 ParM polymerized in AMP-PNP. At all concentrations tested, the AMP-PNP filaments appeared to elongate from both ends and attain lengths much greater than ATP filaments (Fig. 6C and 6D). Although filament fragmentation occurred, we observed no examples of catastrophe. We occasionally observed two types of bundling behaviors that appeared to be length dependent: 1) lateral binding of a smaller filament to the center of a longer filament and 2) the collision of two long filament ends that lead to filament zippering. We measured an elongation rate constant in AMP-PNP of 2.3 monomers x $s^{-1}\mu M^{-1}$ per filament end and a non-catastrophic de-polymerization rate constant of 0.6 monomers per

filament end per second (Fig. 6E). Using these parameters, together with the steady state monomer concentrations in ATP and AMP-PNP, we calculate from equation 2 that, at steady state, 89% of the pB171 filaments are stable and growing while 11% are unstable and shrinking when polymerized in ATP. Comparing this steady state behavior to R1 ParM indicates that the two polymers maintain a similar balance between nucleation, growth and catastrophe.

Discussion

Eukaryotic actins are highly conserved, probably due to the large number of conserved binding partners that regulate their assembly and function. Across metazoan species, for example, actin sequences are ~98% identical. The primary sequences of protozoan actins are more variable but the level of sequence conservation is still much greater than that observed in bacterial actin families. Bacterial actin families are, in fact, much less well defined than eukaryotic actins. The majority of known bacterial actins have been identified by genome searches and the homology cutoff proposed by Derman et al. for defining families (6) is more-or-less arbitrary. We were interested in determining whether one particular clade of bacterial actins, the Alp3 or ParM group, represents a bona fide family with conserved structure and activity. As Figure 7 demonstrates, the ParM family is quite divergent in comparison to the eukaryotic actins.

The ParM protein, encoded by the R1 plasmid is, to date, the most well characterized bacterial ALP (17). It polymerizes into left-handed, double-stranded, helical filaments that nucleate rapidly, elongate symmetrically and are dynamically unstable (20). Here, we show that ParM from the par1 locus of pB171, although only 41% identical to R1 ParM, polymerizes via a similar pathway into filaments that have a remarkably similar structure. Using electron microscopy, we found that pB171 ParM monomers build filaments that are more similar to R1 ParM than to actin or any other characterized actin-like protein (MreB, AlfA, or the pSK41 ALP). Light scattering assays demonstrated that pB171 ParM filaments rapidly and spontaneously form filaments in the absence of nucleation factors in both ATP and GTP. Sedimentation assays demonstrated that pB171 ParM does not polymerize in ADP or GDP, and light scattering assays

revealed that pB171 ParM filaments rapidly de-polymerize in limiting amounts of ATP and GTP prior to complete nucleotide hydrolysis. This is consistent with our previous observation that sub-stoichiometric ratios of ADP to ATP (~20%) destabilize R1 ParM filaments, regardless of the total ATP concentration (20). For both R1 and pB171 ParM we attribute this effect to nucleotide exchange on the terminal subunit of the filament, a phenomenon initially observed for actin filaments (43). Finally, TIRF microscopy of labeled pB171 ParM revealed both symmetrical filament elongation and dynamic instability.

In addition to the basic similarities, we also note three minor differences between the biochemical and biophysical properties of ParM proteins from plasmids R1 and pB171. First, the structure of pB171 ParM filaments is more heterogeneous. This is shown mainly as variability in the degree of helical twist of the strands that compose the filament. We hypothesize that this reflects weaker lateral interactions between the strands that permit them to either rotate or slip more freely. Second, we find that pB171 ParM is slightly more stable in GTP than ATP, as evidenced by the lower steady state monomer concentration. Increased stability in GTP may reflect an increase in the rate of polymerization, a decrease in the rate of de-polymerization of stable or unstable filament ends or a decrease in the propensity of GTP filaments to undergo catastrophe due a reduced rate of nucleotide hydrolysis or phosphate release. Although our analysis did not identify the mechanism of the increased stability in GTP, our phosphate release assays suggests that pB171 ParM filaments hydrolyze GTP at similar rates as ATP. Third, the size of the pB171 ParM filament nucleus is a dimer in ATP and GTP, whereas the apparent size of the R1 ParM nucleus is a trimer (20,27). This probably reflects slight

differences in one of the monomer-monomer interfaces. Depending on buffer conditions, the nucleus size of conventional actin ranges from two to four subunits (41). Osawa and Kansai predicted that all linear helical polymers would generally assemble from nuclei in this size range (44).

Popp et al. (15) recently characterized the structure and assembly of a divergent ALP from plasmid pSK41, which was previously identified by Møller-Jensen et al. as a possible member of the ParM family (10). This ALP is, however, only 18% similar to R1 ParM and falls below the proposed cutoff for definition of ALP families. As noted above, however, this sequence similarity criterion is fairly arbitrary and a more rigorous definition of families requires combining sequence similarity with structural and functional information. Filaments formed by the pSK41 ALP protein lack many of the longitudinal monomer-monomer contacts that define the two long-pitch helices found in actin and ParM and these filaments are best described as single-stranded. In addition, they are not dynamically unstable, and they do not elongate symmetrically. Finally, and most intriguingly, the atomic structure of the pSK41 ALP is more similar to the archeal actin Ta0583 from *T. acidophilum* than to R1 ParM (15). Popp et al. argue that the pSK41 protein represents an evolutionary intermediate between a chromosomally encoded ALP and the plasmid-encoded ParM-family proteins and suggested that it promotes plasmid partitioning via a very different mechanism. Our study and that of Popp et al. highlight the importance of careful structural and functional in defining families of bacterial actin like proteins.

References:

1. Jones, L., Carballido-López, R., and Errington, J. (2001) *Cell* **104**, 913-922
2. Erickson, H. P. (1995) *Cell* **80**, 367-370
3. Komeili, A. (2006) *Science* **311**, 242-245
4. Pradel, N., Santini, C.-L., Bernadac, A., Fukumori, Y., and Wu, L.-F. (2006) *Proc Natl Acad Sci USA* **103**, 17485-17489
5. Møller-Jensen, J., Borch, J., Dam, M., Jensen, R. B., Roepstorff, P., and Gerdes, K. (2003) *Molecular Cell* **12**, 1477-1487
6. Derman, A. I., Becker, E. C., Truong, B. D., Fujioka, A., Tucey, T. M., Erb, M. L., Patterson, P. C., and Pogliano, J. (2009) *Molecular Microbiology* **73**, 534-552
7. Daniel, R. A., and Errington, J. (2003) *Cell* **113**, 767-776
8. Becker, E., Herrera, N. C., Gunderson, F. Q., Derman, A. I., Dance, A. L., Sims, J., Larsen, R. A., and Pogliano, J. (2006) *EMBO J* **25**, 5919-5931
9. Schumacher, M. A. (2008) *Biochem J* **412**, 1-18
10. Møller-Jensen, J., Jensen, R. B., Löwe, J., and Gerdes, K. (2002) *EMBO J* **21**, 3119-3127
11. van den Ent, F., Amos, L. A., and Löwe, J. (2001) *Nature* **413**, 39-44
12. van den Ent, F., Møller-Jensen, J., Amos, L. A., Gerdes, K., and Löwe, J. (2002) *EMBO J* **21**, 6935-6943
13. Hara, F., Yamashiro, K., Nemoto, N., Ohta, Y., Yokobori, S.-i., Yasunaga, T., Hisanaga, S.-i., and Yamagishi, A. (2007) *J Bacteriol* **189**, 2039-2045
14. Polka, J. K., Kollman, J. M., Agard, D. A., and Mullins, R. D. (2009) *J Bacteriol* **191**, 6219-6230
15. Popp, D., Xu, W., Narita, A., Brzoska, A. J., Skurray, R. A., Firth, N., Goshdastider, U., Maeda, Y., Robinson, R. C., and Schumacher, M. A. (2010) *Journal of Biological Chemistry* **285**, 10130-10140
16. Orlova, A., Garner, E. C., Galkin, V. E., Heuser, J., Mullins, R. D., and Egelman, E. H. (2007) *Nat Struct Mol Biol* **14**, 921-926
17. Needleman, D. J. (2008) *Curr Biol* **18**, R212-214
18. Garner, E. C., Campbell, C. S., Weibel, D. B., and Mullins, R. D. (2007) *Science* **315**, 1270-1274
19. Campbell, C. S., and Mullins, R. D. (2007) *J Cell Biol* **179**, 1059-1066
20. Garner, E. C., Campbell, C. S., and Mullins, R. D. (2004) *Science* **306**, 1021-1025
21. Tobe, T., Hayashi, T., Han, C. G., Schoolnik, G. K., Ohtsubo, E., and Sasakawa, C. (1999) *Infect Immun* **67**, 5455-5462
22. Ebersbach, G., and Gerdes, K. (2001) *Proc Natl Acad Sci USA* **98**, 15078-15083
23. Dion, V., Shimada, K., and Gasser, S. M. (2010) *Current Opinion in Cell Biology* **22**, 383-391
24. Ohi, M., Li, Y., Cheng, Y., and Walz, T. (2004) *Biol Proced Online* **6**, 23-34
25. Mindell, J. A., and Grigorieff, N. (2003) *Journal of structural biology* **142**, 334-347
26. Egelman, E. H. (2000) *Ultramicroscopy* **85**, 225-234

27. Galkin, V. E., Orlova, A., Rivera, C., Mullins, R. D., and Egelman, E. H. (2009) *Structure* **17**, 1253-1264
28. Cer, R., Mudunuri, U., Stephens, R., and Lebeda, F. (2009) *Nucleic Acids Research* **37,** W441-W445
29. Abramoff, M, and Magelhaes, P. (2004) *Biophotonics International **11, 36-42***
30. Edgar, R. (2004) *Nucleic Acids Research* **32**, 1792
31. Waterhouse, A. M., Procter, J. B., Martin, D. M. A., Clamp, M., and Barton, G. J. (2009) *Bioinformatics* **25**, 1189-1191
32. Tamura, K., Dudley, J., Nei, M., and Kumar, S. (2007) *Mol Biol Evol* **24**, 1596-1599
33. Saitou, N., and Nei, M. (1987) *Mol Biol Evol* **4**, 406-425
34. Felsenstein, J. (1985) *Evolution **39**,783-791*
35. Wen, K., Yao, X., and Rubenstein, P. (2002) *Journal of Biological Chemistry* **277**, 41101
36. Esue, O., Wirtz, D., and Tseng, Y. (2006) *Journal of Bacteriology* **188**, 968-976
37. Popp, D., Narita, A., Oda, T., Fujisawa, T., Matsuo, H., Nitanai, Y., Iwasa, M., Maeda, K., Onishi, H., and Maéda, Y. (2008) *EMBO J* **27**, 570-579
38. Bennett, B., Kimball, E., Gao, M., Osterhout, R., Van Dien, S., and Rabinowitz, J. (2009) *Nat Chem Biol* **5**, 593-599
39. Pollard, T. (1986) *J Cell Biol* **103**, 2747
40. Nishida, E., and Sakai, H. (1983) *Journal of biochemistry* **93**, 1011
41. Cooper, J., Buhle Jr, E., Walker, S., Tsong, T., and Pollard, T. (1983) *Biochemistry* **22**, 2193-2202
42. Flyvbjerg, H., Jobs, E., and Leibler, S. (1996) *Proc Natl Acad Sci USA* **93**, 5975-5979
43. Teubner, A., and Wegner, A. (1998) *Biochemistry* **37**, 7532-7538
44. Oosawa, F., and Kasai, M. (1962) *Journal of Molecular Biology* **4**, 10-21

Figure Legends

Figure 1. pB171 ParM forms filaments in (A) AMP-PNP, (B) ATP, and (C) GTP. pB171 ParM (9.5 μM) was polymerized with 5 mM nucleotide, stained with 0.75% uranyl formate, and visualized by transmission EM. The conditions used were as follows: 100 mM KCl, 30 mM Tris HCl (pH 7.5), 1 mM $MgCl_2$, 1 mM DTT, and 25°C. Scale bar: 50 nm.

Figure 2. EM reconstruction of pB171 ParM filaments. (A) The pB171 ParM filament structure, calculated from a subset of filament segments that converged to helical symmetry of 166.1° rotation and 24.2 Å rise per subunit. The map is filtered to 19 Å, the estimated resolution of the reconstruction. Each filament strand is rendered in a different color. (B) For comparison, a reconstruction of R1 ParM filaments was calculated, with refined helical symmetry of 165.4° rotation and 24.5 Å rise per subunit. C) The crystal structure of R1 ParM was manually fit into the EM structure of the pB171 ParM filament, and the fit along a single strand is shown.

Figure 3. pB171 ParM binds preferentially to ATP over GTP. (A) Pseudo-first order association kinetics of pB171 ParM binding to etheno-ATP. The slope of the line estimates the 2^{nd} order association rate constant and the y-intercept estimates the 1^{st} order disassociation rate constant. The inset shows representative association curves for 75 μM and 13.5 μM 1,N6-etheno-ATP. Buffer conditions: 100 mM KCl, 30 mM Tris-HCL pH 7.5, 1 mM $MgCl_2$, 1 mM DTT and 200 mM acrylamide. (B). Competitive binding experiments of 1,N6-etheno-ATP versus ATP and GTP for pB171 ParM. The data was fit

to a four-parameter logistic curve to estimate the IC_{50}. Buffer conditions were the same as above.

Figure 4. Light scattering assays demonstrate that pB171 ParM nucleates and assembles rapidly in ATP and GTP. (A and B). Rapid assembly of pB171 ParM in 10 mM $MgCl_2$-ATP (A) and 10 mM $MgCl_2$-GTP (B) monitored by light scattering. Buffer conditions for all experiments in this figure: 100 mM KCl, 30 mM Tris-HCl, 1 mM $MgCl_2$, 1mM DTT. (C) Determination of the nucleus size and relative rates of nucleation in ATP and GTP. The log of the maximal rate of assembly (V_{max}) normalized by the maximum light scattering intensity was plotted versus the log concentration of pB171 ParM. The nucleus size (n) is estimated as 2 times the slope of the linear fit and the x-intercept is proportional to the square root of the nucleation rate constant times the elongation rate constant. The error bars are the standard deviation of calculated values from 3 separate experiments. (D) Normalized intensity (I(t)/Imax) plotted versus normalized time ($t/t_{1/2}$) for the highest two concentrations of pB171 ParM in ATP (dark grey) and GTP (light grey). Inset: earliest time points (Triangles: ATP, Circles: GTP).

Figure 5. Light scattering and phosphate release assays demonstrate that pB171 ParM is unstable in limiting concentrations of nucleotide and rapidly hydrolyzes nucleotide and releases phosphate. (A&B). Assembly of pB171 ParM in various concentrations of ATP (A) and GTP (B). (F-I) Phosphate release assays. The amount of phosphate released by 5 μM pB171 ParM polymerized in 1 mM ATP (F), 1 mM GTP (G), 0.1 mM ATP (H) or 0.1 mM GTP (I) are plotted versus time (closed squares). Parallel assembly reactions were monitored with light scattering using the same stock

protein solutions (closed circles). Buffer conditions for all experiments in this figure are the same as those used for the experiment in Figure 4.

Figure 6. Time-lapse TIRF microscopy observing individual filaments demonstrate that pB171 ParM is dynamically unstable when polymerized in ATP and appears to elongate symmetrically. (A) Montage of an individual pB171 ParM filament in ATP. 25% Alexa-488 labeled 2.8 μM B171 ParM was polymerized in the presence of 10 mM ATP and imaged via TIRF microscopy every 2 seconds. Buffer conditions: 100 mM KCl, 30 mM KCl, 1 mM $MgCl_2$, 1 mM DTT, 0.8% methyl-cellulose, 0.5% BSA. Scale bar: 1 um. (B) Length versus time for 6 representative filaments polymerized in ATP. (C and D) Montage of individual filaments polymerized in non-hydrolysable AMP-PNP. 25% Alexa-488 labeled 0.8 μM or 1.0 μM pB171 ParM was polymerized in the presence of 10 mM AMP-PNP. Time interval is 20 seconds between each frame. Buffer conditions are the same as in ATP. Scale bar: 1um. (E). Rate of elongation of AMP-ParM. The rate of elongation was measured at various concentrations of pB171 ParM in AMP-PNP and plotted versus the μM pB171 ParM. The line fit to the data represents the equation: rate of filament elongation $=k_{on}$ x (μM protein)-k_{off}. Inset shows 3 representative filaments growth over time from 0.6 μM, 0.8 μM and 1.0 μM pB171 concentrations.

Figure 7. Evolutionary relationships demonstrate that the ParM family is more divergent than eukaryotic actins. The tree represents a bootstrap consensus tree inferred from 1000 replicate trees generated using the Neighbor-Joining method. The percentage of replicate trees in which the associated taxa clustered together in the bootstrap test is shown next to the branches. The branch lengths are proportional to the relative evolutionary distance, and the scale bar is in units of the number of amino acid

substitutions per site. The GI accession numbers for the sequences and the sequence alignments used to generate this phylogram are provided in the supplementary materials. Evolutionary analyses were conducted in MEGA4.

Table 1	
Nucleotide	Steady State Monomer Concentration μM
ATP	1.5±0.12
ADP	>114
AMP-PNP	0.5±0.04
GTP	1.1±0.21
GDP	>114
GMP-PNP	0.77±0.1

* The steady state monomer concentrations were determined by sedimentation assays.

Figure 1

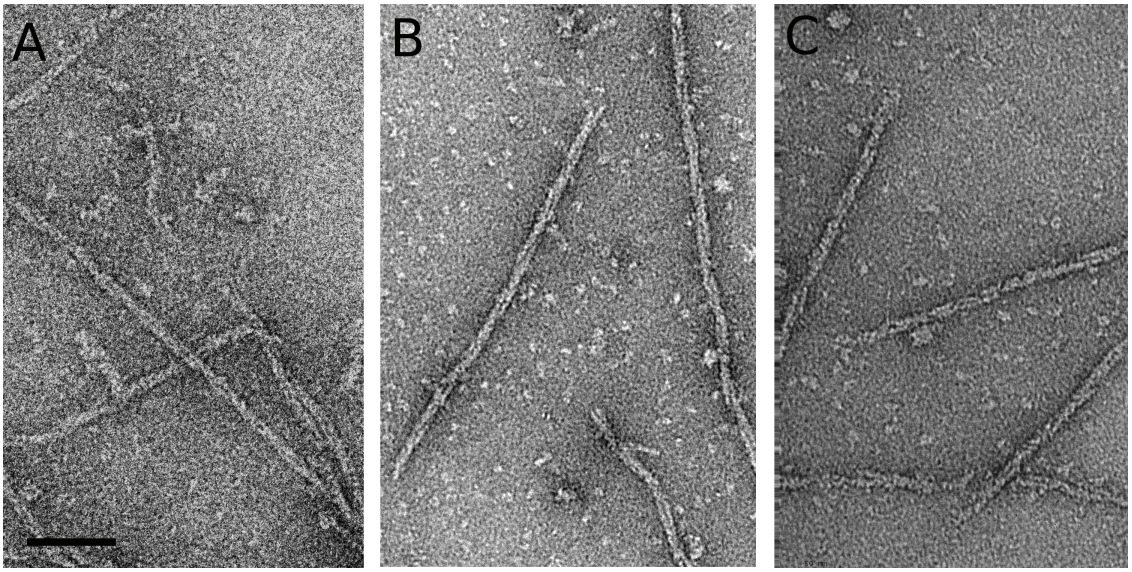

Figure 2

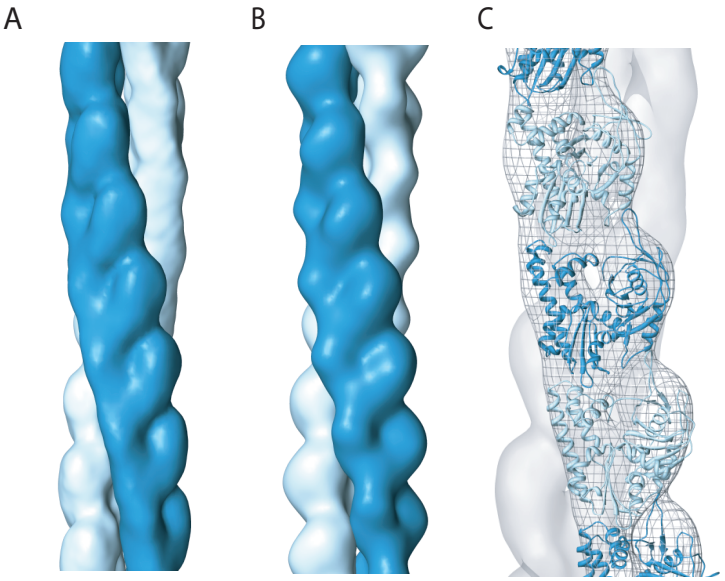

Figure 3

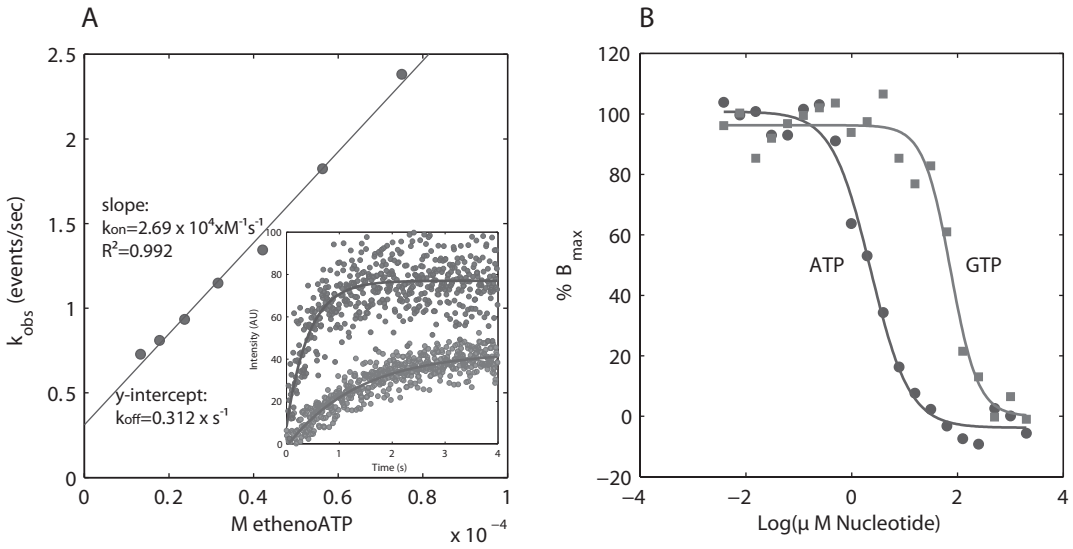
A
B
slope:
kon=2.69 x 10^4xM^-1s^-1
R^2=0.992
y-intercept:
koff=0.312 x s^-1
k obs (events/sec)
M ethenoATP
x 10^-4
Intensity (AU)
Time (s)
% B max
ATP
GTP
Log(µ M Nucleotide)

Figure 4

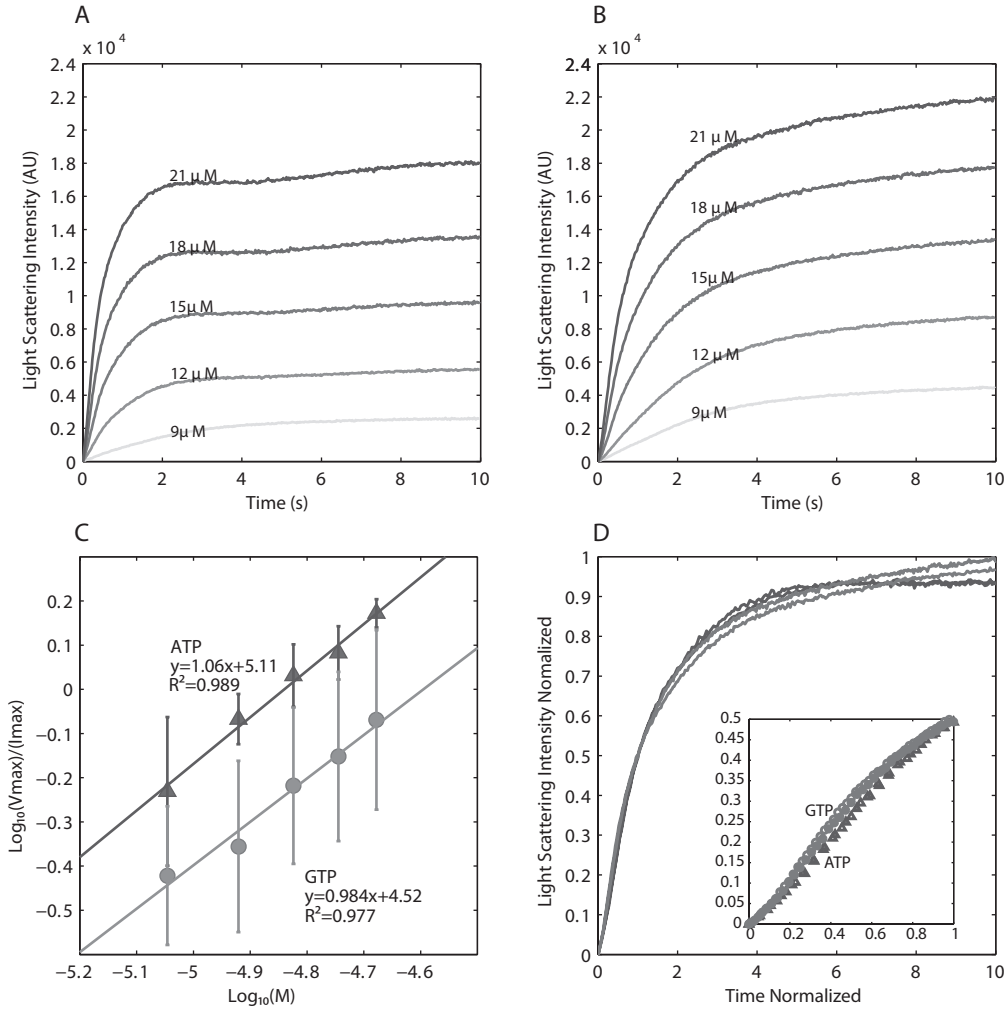
A
x 10^4
Light Scattering Intensity (AU)
21 µ M
18 µ M
15µ M
12 µ M
9µ M
Time (s)
B
x 10^4
Light Scattering Intensity (AU)
21 µ M
18 µ M
15µ M
12 µ M
9µ M
Time (s)
C
ATP
y=1.06x+5.11
R²=0.989
GTP
y=0.984x+4.52
R²=0.977
Log10(Vmax)/(Imax)
Log10(M)
D
Light Scattering Intensity Nomalized
GTP
ATP
Time Normalized

Figure 5

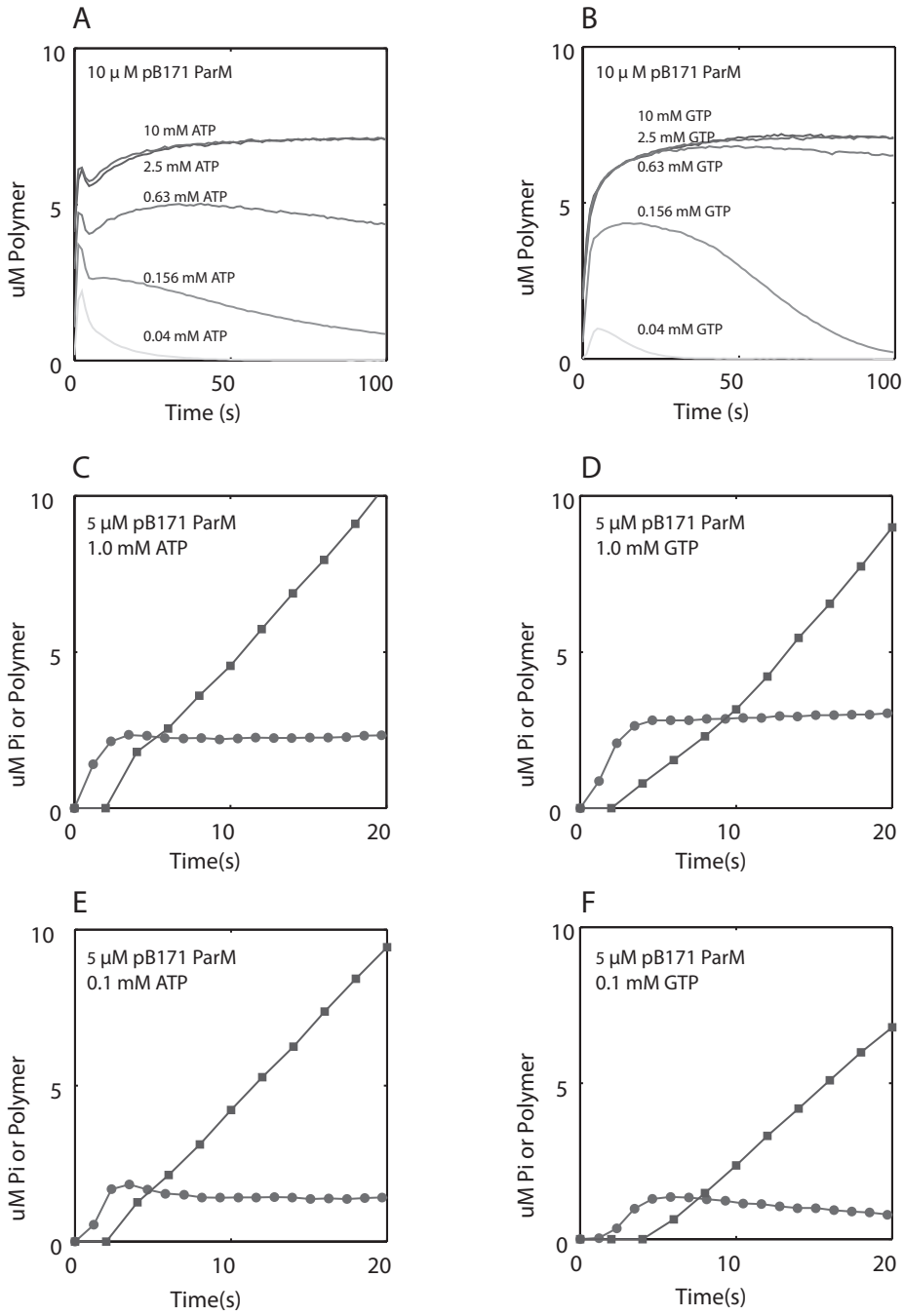
A
10 µ M pB171 ParM
10 mM ATP
2.5 mM ATP
0.63 mM ATP
0.156 mM ATP
0.04 mM ATP
uM Polymer
Time (s)
B
10 µ M pB171 ParM
10 mM GTP
2.5 mM GTP
0.63 mM GTP
0.156 mM GTP
0.04 mM GTP
uM Polymer
Time (s)
C
5 µM pB171 ParM
1.0 mM ATP
uM Pi or Polymer
Time(s)
D
5 µM pB171 ParM
1.0 mM GTP
uM Pi or Polymer
Time(s)
E
5 µM pB171 ParM
0.1 mM ATP
uM Pi or Polymer
Time(s)
F
5 µM pB171 ParM
0.1 mM GTP
uM Pi or Polymer
Time(s)

Figure 6

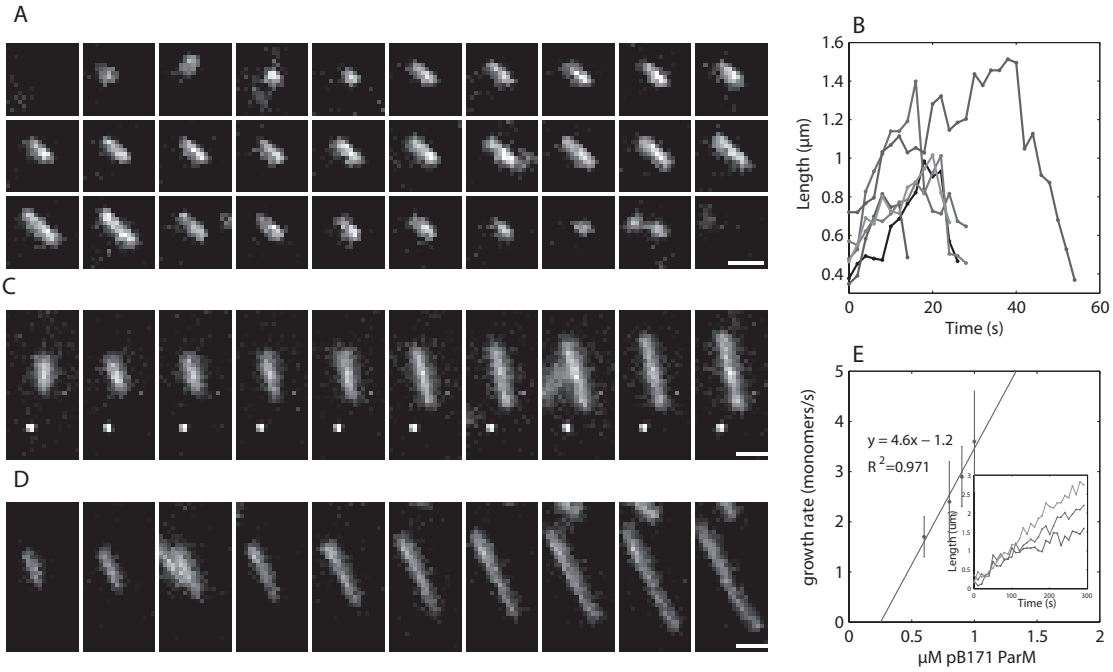
A
B
C
D
E
Length (μm)
Time (s)
growth rate (monomers/s)
μM pB171 ParM
y = 4.6x − 1.2
R 2=0.971
Length (μm)
Time (s)

Figure 7

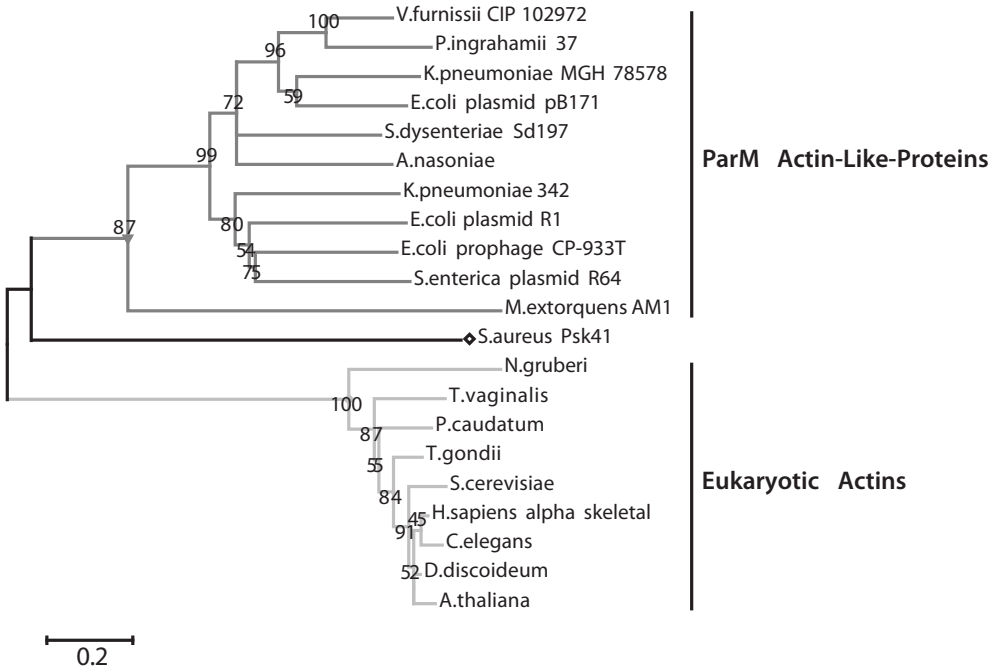
V.furnissii CIP 102972
P.ingrahamii 37
K.pneumoniae MGH 78578
E.coli plasmid pB171
S.dysenteriae Sd197
A.nasoniae
K.pneumoniae 342
E.coli plasmid R1
E.coli prophage CP-933T
S.enterica plasmid R64
M.extorquens AM1
S.aureus Psk41
N.gruberi
T.vaginalis
P.caudatum
T.gondii
S.cerevisiae
H.sapiens alpha skeletal
C.elegans
D.discoideum
A.thaliana
100
96
59
72
99
87
80
54
75
100
87
55
84
45
91
52
0.2
ParM Actin-Like-Proteins
Eukaryotic Actins

Supplementary Information:

The phylogenetic analysis in Figure 7 was performed using the following sequences:

Sequence name: GI accession number.

ParM sequences:

V. furnissii CIP 102972: 260768794

P. ingrahamii 37: 119947163

K. pneumoniae MGH 78578: 152973663

E. coli plasmid pB171:10955418

S. dysenteriae Sd197: 82524481

A. nasoniae: 284008122

K. pneumoniae 342: 206581098

E. coli plasmid R1: 9507578

E. coli prophage CP-933T: 91209978

S. enterica plasmid R64: 32470180

M. extorquens AM: 240141815

PsK41 ALP

S. aureus Psk41: 284793988

Actin Sequences

N. gruberi: 290974733

T. vaginalis: 123444869

P. caudatum: 15212111

T. gondii: 606857

S. cerevisiae: 170986

H. sapiens alpha skeletal: 4501881

C. elegans: 51011295

D. discoideum: 66804711

A. thaliana: 1002533

Note: supplementary Figures 5,6,7 are not mentioned explicitly in the manuscript; however, they are the alignments that were used in the generation of the phylogram in Figure 7.

Supplementary Figure Legends

Supplementary Figure 1: Variability in twist states and filament resolution of pB171 ParM IHRS reconstruction. (A) The global reconstruction of R1 ParM filament in AMP-PNP rapidly converged to a stable solution. (B) The global reconstruction of pB171 ParM AMP-PNP failed to converge to stable solution. (C) A reconstruction based on a single class of pB171 filament particles converged to an oscillating solution. (D) The resolution of the final pB171 ParM AMPPNP reconstruction is estimated to be 19 Å.

Supplementary Figure 2: pB171 ParM polymerization is enhanced by divalent cations and requires nucleotide. (A) High-speed sedimentation assay with pB171 ParM polymerized in different buffer conditions in the presence or absence of either ATP or GTP. The bands are from the supernatant fraction of the sedimentation reaction. Base buffer: 100 mM KCl, 15 mM Tris-HCl 1 mM DTT ± 1mM DTT, $MgCl_2$, or $CaCl_2$. Nucleotide concentration: 1 mM. (B) Quantification of sedimentation experiment from A. Bars: Black: buffer no nucleotide, Grey: buffer + ATP, White: buffer + GTP. Error bars are S.D. from two experiments. (C and D) Quantification of High-speed sedimentation assays measuring the steady state monomer concentration of pB171 ParM in different nucleotides. (C) 10 mM $MgCl_2$ ATP (circles) or 10 mM $MgCl_2$-GTP (triangles). (D) 10 mM AMP-PNP (circles) or GTP (triangles). Buffer conditions: 100 mM KCl, 15 mM Tris-HCl, 1mM $MgCl_2$, 1 mM DTT.

Supplementary Figure 3: Log-Log plots of the initial time points from normalized light scattering data of various concentrations of pB171 ParM polymerized in 10 mM $MgCl_2$-ATP or $MgCl_2$-GTP indicate that the nucleus size is two in both conditions. (A&B) The amplitudes and times of light scattering data from ParM polymerized in (A) ATP or (B) GTP were normalized by the maximum intensity and half times respectively. The initial 20 data points of 15 normalized

data series were combined into a single data series and plotted on a log-log plot. The slope of the line fit to the combined data estimates the number of kinetic steps in nucleus formation; therefore the nucleus size is estimated as the slope+1. (C&D) Determination of the slope at the earliest time points provides an additional estimation of the number of kinetic steps in nucleus formation. The slopes of lines fit to the first n (5-20) data points from each normalized data series from (A) and (B) were determined using the MATLAB poly-fit function. The slopes of the lines were averaged. The average slope was plotted versus the number of points (i.e. the value at 10 points is the average slope of lines fit to the first 10 data points of each series and the value at 11 points is the average slope of lines fit to the first 11 points of each data series). A line was fit to the plot. The slope value when the number of points is extrapolated to 1 estimates the slope at the earliest time points of the reaction. This initial slope is equal to the number of kinetic steps in nucleus formation. Again, the nucleus size is equal to the number of kinetic steps +1. Error bars represent the standard deviation of the slopes calculated for n points.

Supplementary Figure 4: Plots of light scattering data from pB171 ParM polymerized with a range of nucleotide concentrations. (A and B). 10 uM pB171 ParM was polymerized with a range of concentrations of (A) $MgCl_2$-ATP or (B) $MgCl_2$ -GTP. The light scattering intensity was plotted versus time. Buffer conditions are the same as in Figure 5. (C and D). Fast data acquisition of light scattering data from the first ten seconds of the polymerization time courses of the same samples as in (A) $MgCl_2$-ATP and (B) $MgCl_2$ -GTP. (E and F). Fast data acquisition of light scattering data from the first ten seconds of the polymerization time courses of the same samples as in (A) ATP and (B) GTP from Figure 5A and 5B. (G) Rate of disassembly of pB171 ParM polymerized in 40 μM ATP or GTP. The amplitude of the time series data for 40 μM nucleotide from Figure 5A and 5B were normalized by the maximum amplitude and plotted versus time. Circles: ATP and triangle: GTP.

Supplementary Figure 5: Sequence alignment of diverse eukaryotic actins demonstrates a high level of conservation. Residues that are conserved in 25% of the sequence in the alignment are colored using a scheme based on Clustal X.

Supplementary Figure 6: Sequence alignment of representative proteins of the ParM demonstrates less sequence conservation than the actin family. Residues that are conserved in 25% of the sequence in the alignment are colored using a scheme based on Clustal X.

Supplementary Figure 7: Joint sequence alignment of the actin and ParM proteins from supplementary Figure 5 and 6 used to generate the phylogenetic tree in Figure 7**.** Residues that are conserved in 25% of the sequence in the alignment are colored using a scheme based on Clustal X.

Supplemental Figure 1

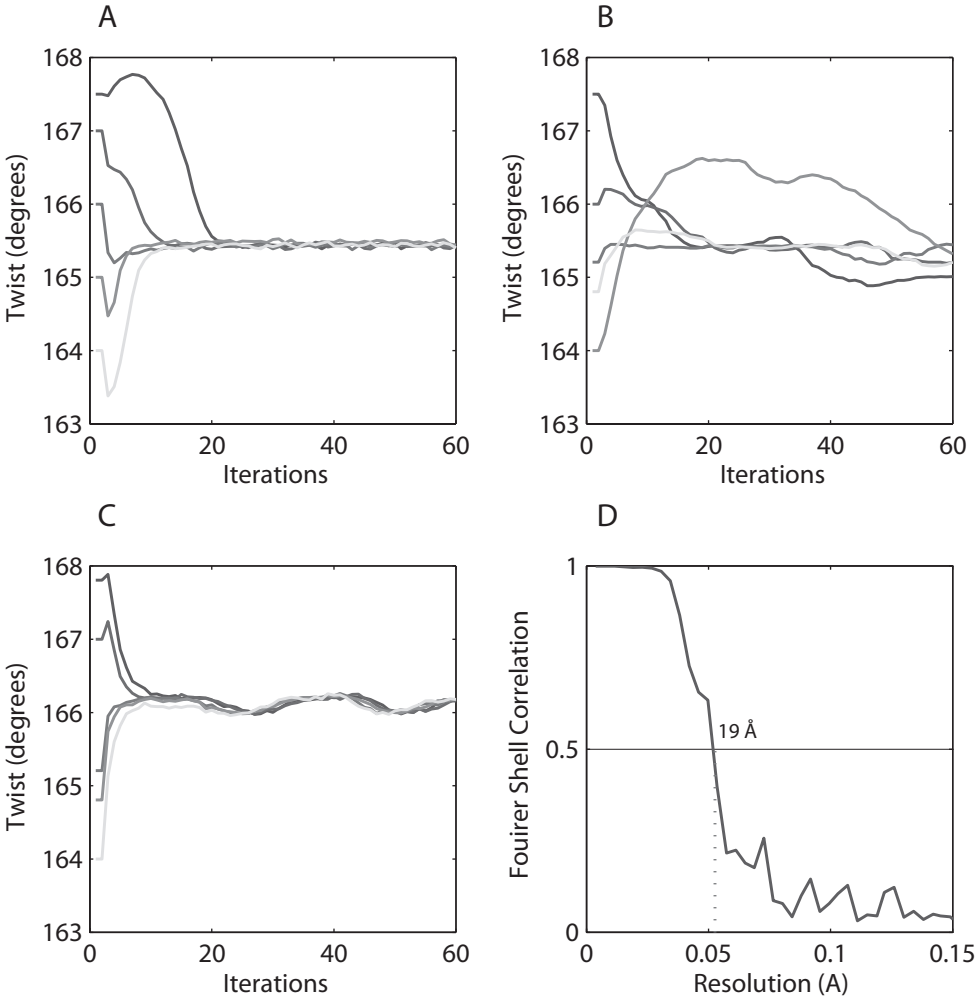

Supplemental Figure 2

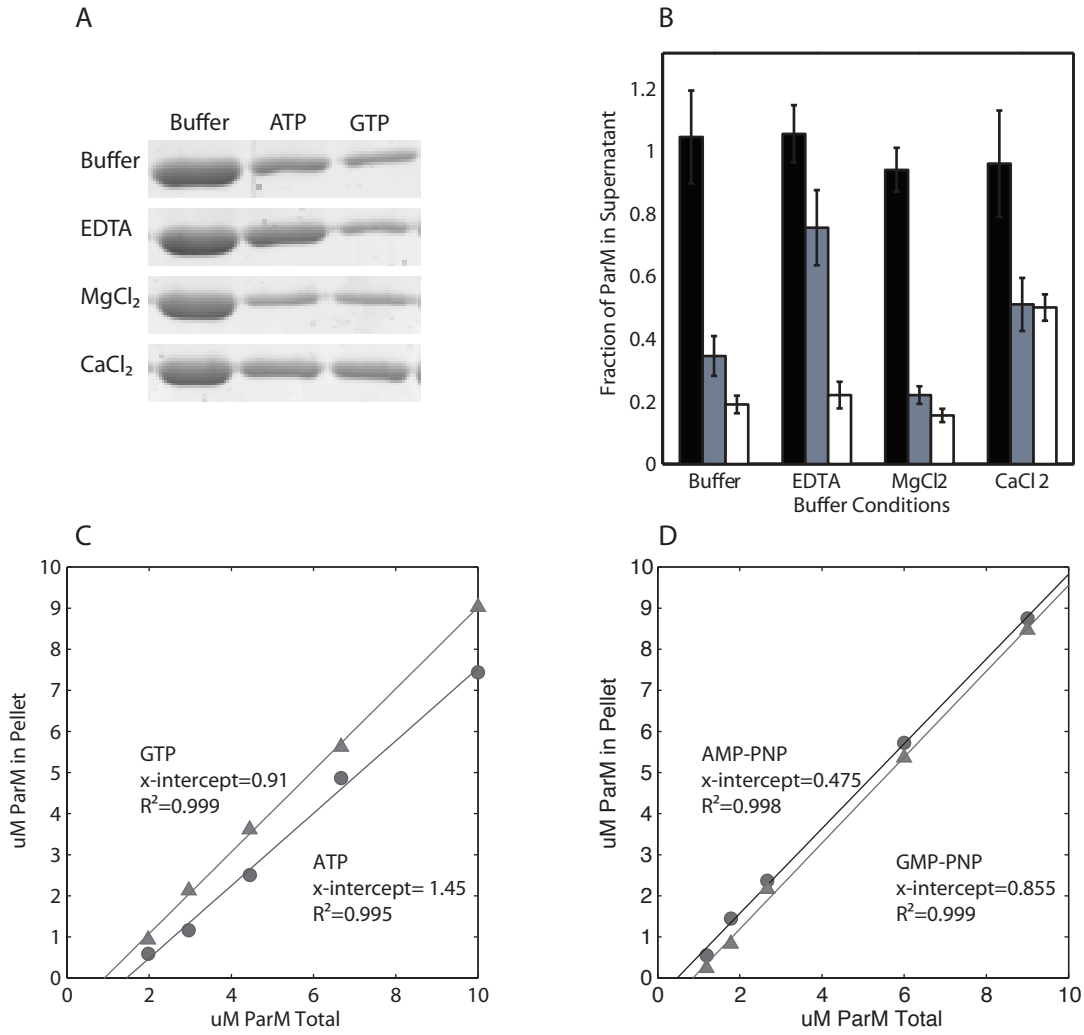

Supplemental Figure 3

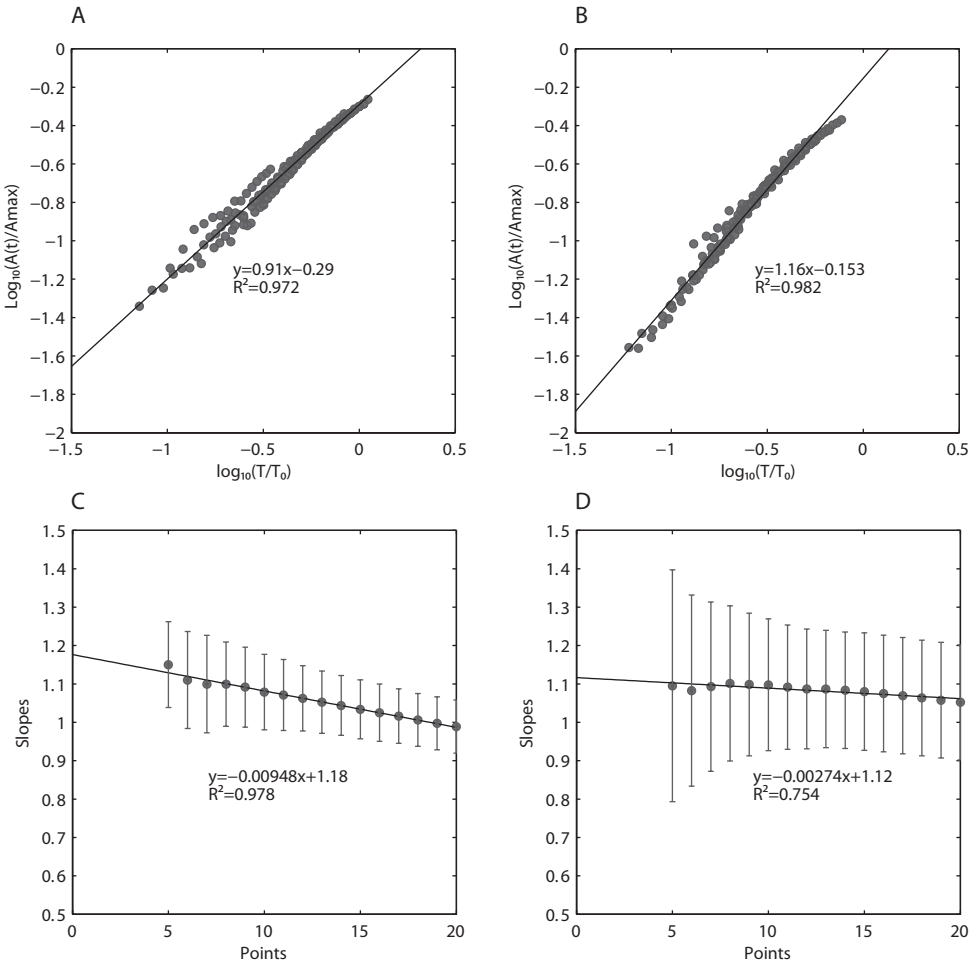

Supplemental Figure 4

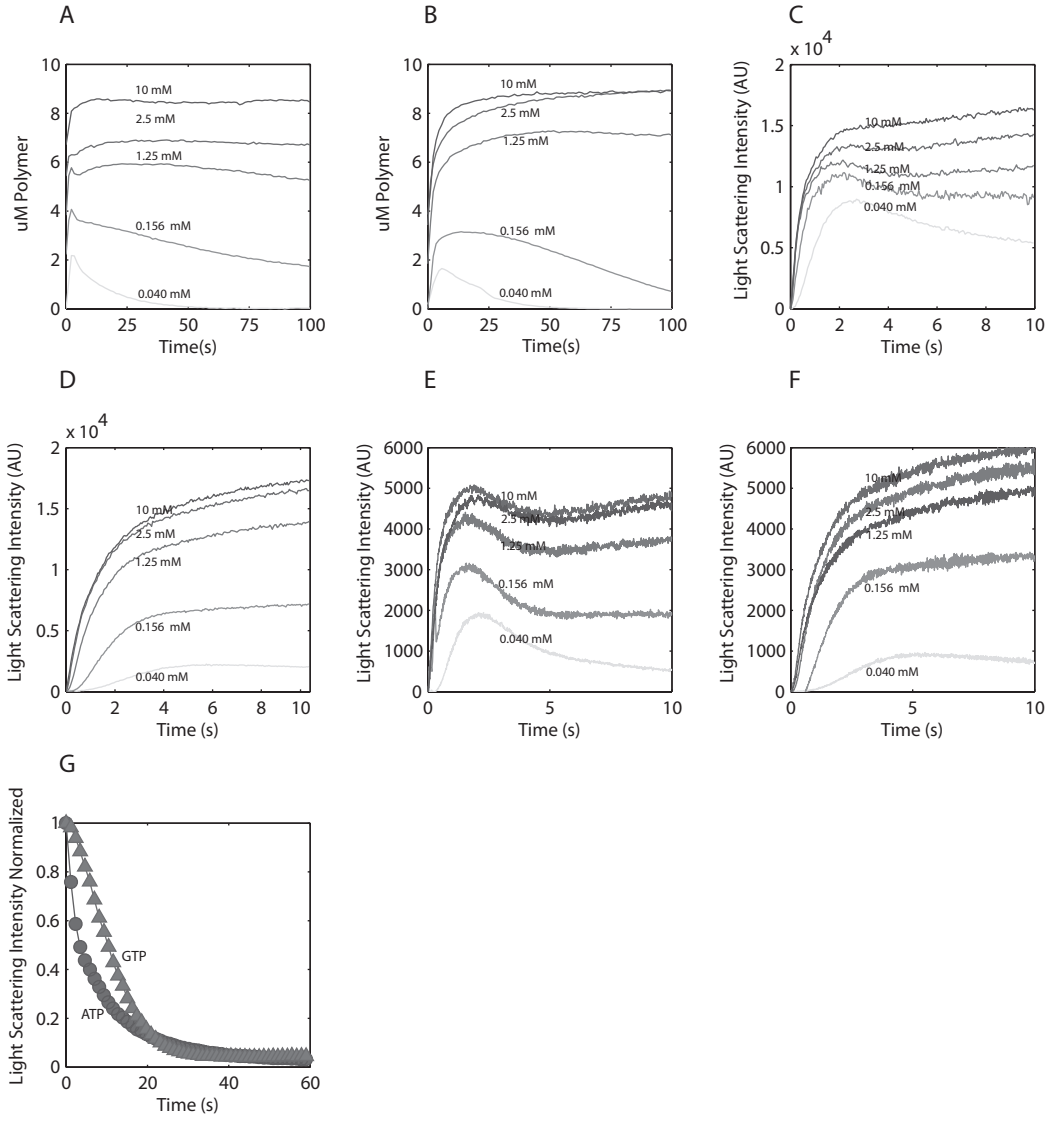

Supplemental Figure 5

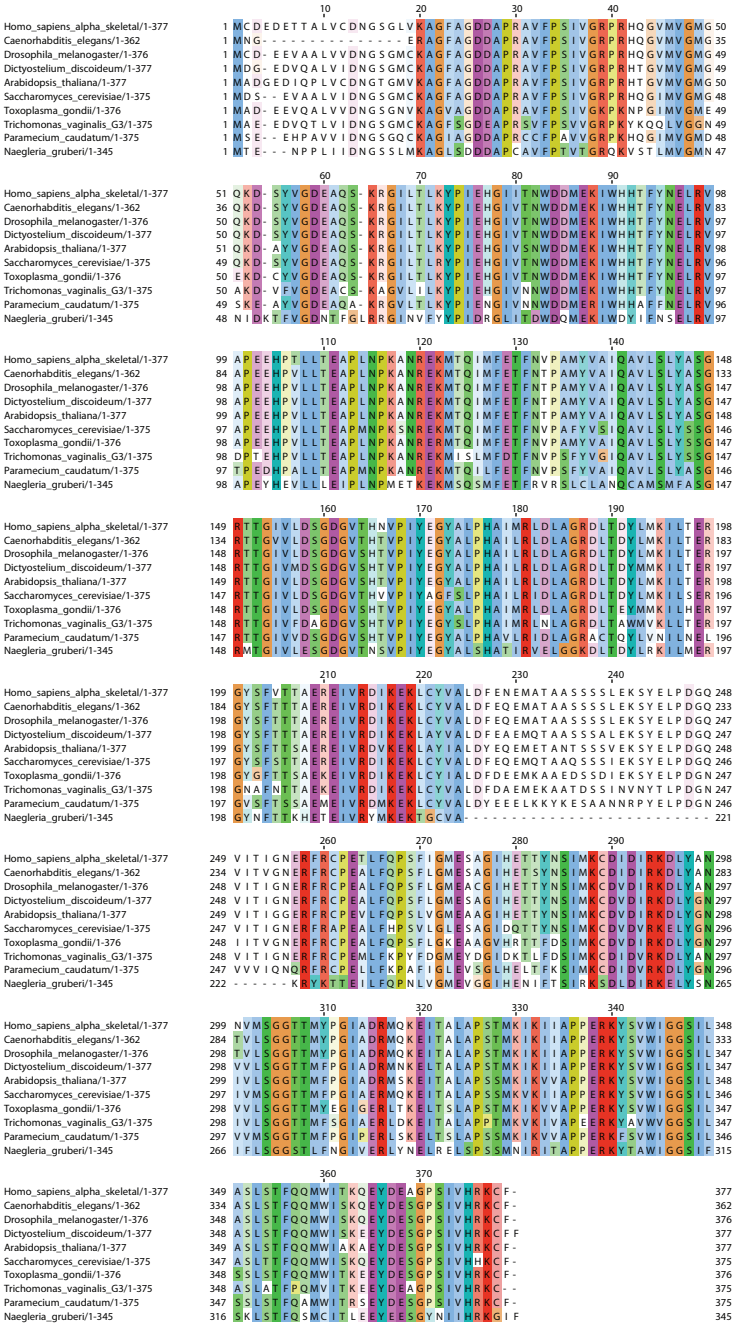

Supplemental Figure 6

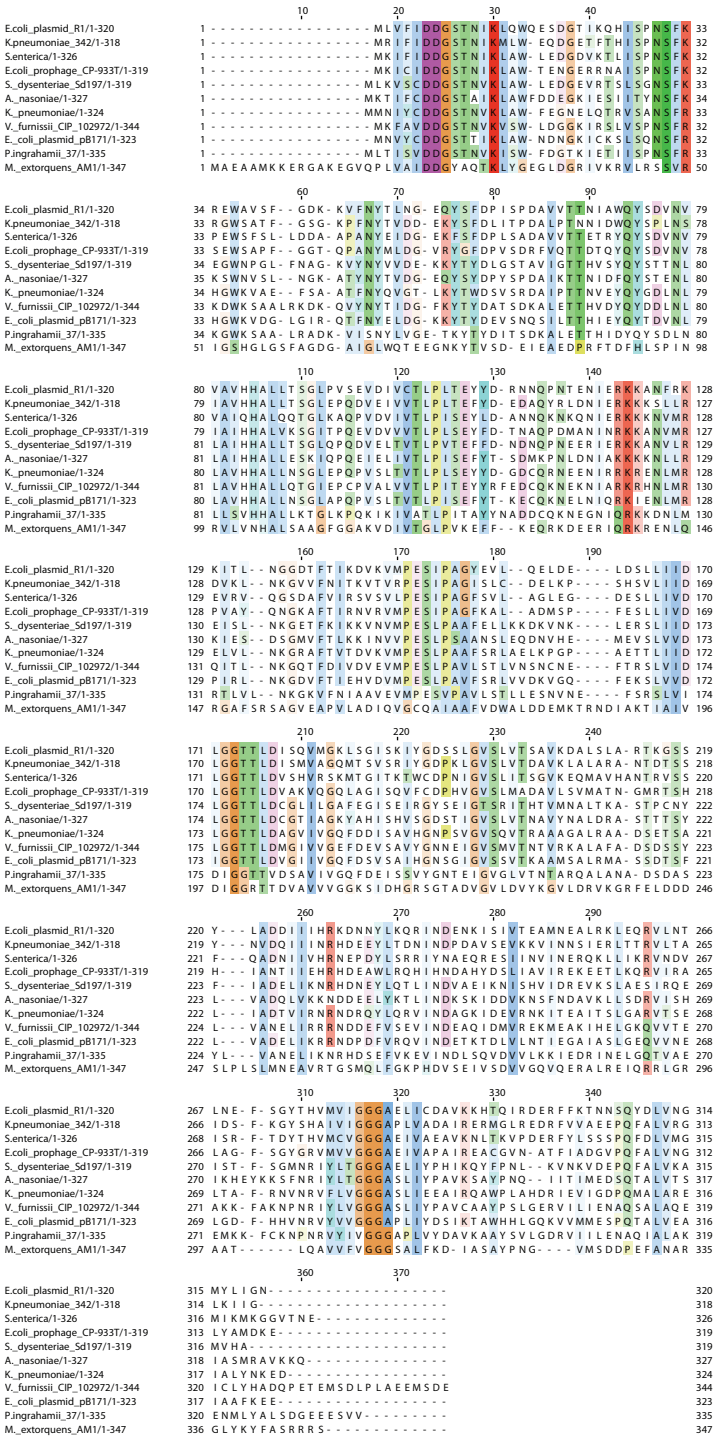

Supplemental Figure 7

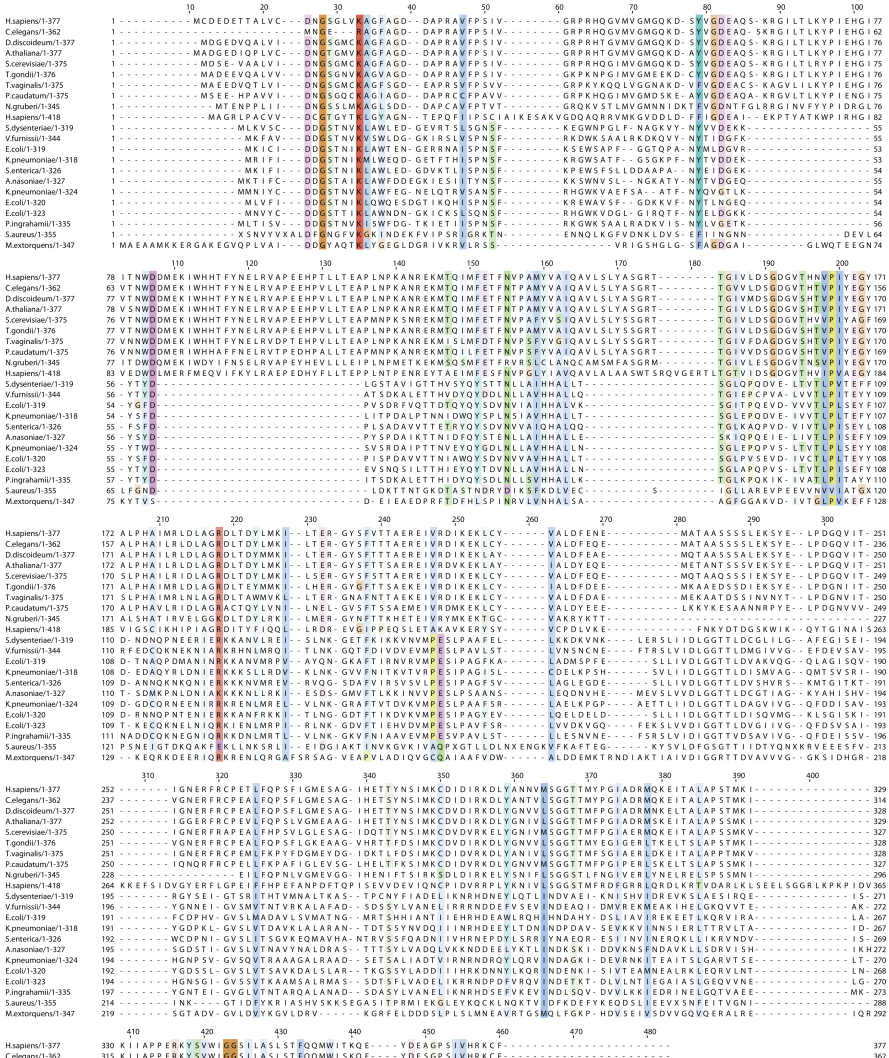

Chapter 4

Structural Polymorphism of the ParM Filament and Dynamic Instability

Vitold E. Galkin, Albina Orlova, Chris Rivera, R. Dyche Mullins and Edward H. Egelman

Published: September 9, 2009, Structure, 17:1253-1264

Contributions

This work was done in collaboration with members of the Egelman Lab. Vitold E. Galkin and Albina Orlova performed the electron microscopy and structural analysis present in figures 1 and 4-8, and the two supplemental figures. I purified the ParM proteins that were used in the study and performed the biochemical and TIRF microscopy experiments in figures 2 and 3. I also contributed to the discussion of the paper.

Summary

Segregation of the R1 plasmid in bacteria relies on ParM, an actin homolog that segregates plasmids by switching between cycles of polymerization and depolymerization. We find similar polymerization kinetics and stability in the presence of either ATP or GTP and a 10-fold affinity preference for ATP over GTP. We used electron cryo-microscopy to evaluate the heterogeneity within ParM filaments. In addition to variable twist, ParM has variable axial rise, and both parameters are coupled. Subunits in the same ParM filaments can exist in two different structural states, with the nucleotide-binding cleft closed or open, and the bound nucleotide biases the distribution of states. The interface between protomers is different between these states, and in neither state is it similar to F-actin. Our results suggest that the closed state of the cleft is required but not sufficient for ParM polymerization, and provide a structural basis for the dynamic instability of ParM filaments.

Introduction

Bacterial survival in an environment containing fungi and heavy metal ions depends on plasmids—extrachromosomal DNA molecules capable of replicating independently of the host genome. High-copy-number plasmids are separated randomly in bacteria, whereas low-copy-number plasmids require an active mechanism of segregation to preserve the maintenance of plasmids in daughter cells following division. Most of our knowledge about plasmid DNA partitioning comes from studies on the large low-copy-number plasmid R1 (Nordstrom et al., 1980). The stability operon par encodes three components sufficient for plasmid segregation: parR and parM genes along with the cis-acting locus, *parC* (Gerdes and Molin, 1986). The current model for type II partitioning assumes that ParR binds cooperatively to several repeats of the *parC* locus, whereas ParM bound to ParR pushes the two newly formed plasmids to the opposite poles of the bacterial cell via ATP-dependent polymerization ([Moller-Jensen et al., 2003], [Salje and Lowe, 2008], [Campbell and Mullins, 2007] and [Choi et al., 2008]). Sequence analysis of ParM (Jensen and Gerdes, 1997) has revealed a set of common conserved residues found in the actin superfamily of proteins (Bork et al., 1992), whereas the crystal structure of ParM unambiguously showed ParM to be a bacterial actin homolog (van den Ent et al., 2002). Nevertheless, alignment of the crystal structures of actin and ParM reveals that regions of actin involved in subunit-subunit interactions within the filament (Oda et al., 2009) are very different from ParM (van den Ent et al., 2002). This coincides with the finding that, in contrast to the F-actin right-handed two-

start helix, ParM forms a left-handed two-start helix ([Orlova et al., 2007] and [Popp et al., 2008]) caused by the different subunit-subunit interfaces. It is likely that the structural differences in filament organization between F-actin and ParM result in the substantial differences observed between the polymerization properties of these proteins. ParM nucleates 300 times faster than actin and grows from both ends with the same rate (Garner et al., 2007). Importantly, ParM filaments are dynamically unstable and, upon ATP hydrolysis, can switch from elongation to rapid shortening (Garner et al., 2004). Such instability is crucial for plasmid partitioning, as ParM mutants with reduced ATPase activity in vitro are nonfunctional in vivo (Jensen and Gerdes, 1997). The filaments capped with the ParR/*ParC* complex are stable and can grow to be long in the cell (Campbell and Mullins, 2007). The ParR/*ParC* complex may bind to the side of ParM and remain attached to the ATP cap of the growing filament, preventing the dissociation of the cap (Choi et al., 2008). Alternatively, the ParR/*ParC* complex may form a protective cap on the end of the filament to maintain its integrity via a processive polymerization mechanism (Salje and Lowe, 2008).

However, the structure of the ParM filament is still controversial, and it has been suggested that the intersubunit contacts in ParM are similar to those in F-actin ([Popp et al., 2008] and [Lowe and Amos, 2009]). We show that the ParM filament has both variable twist and variable axial rise, and subunits can coexist within the same filament in two structural states, with the nucleotide cleft closed or open. These states are not simply related to the bound nucleotide, as both states may be found with the same nucleotide bound. However, the nucleotide biases the distribution of states, with ATP shifting the

distribution toward the closed state while ADP-Pi shifts the equilibrium toward the open form.

Results

Comparison of Negatively Stained and Frozen Hydrated ParM Filaments Formed in the Presence of AMP-PNP and GMP-PNP

A recent paper (Popp et al., 2008) has used X-ray fiber diffraction and negative stain EM to study ParM filaments and arrived at very different results from the cryo-EM structure that we published (Orlova et al., 2007). Since Popp et al. (2008) used GMP-PNP (a nonhydrolyzable analog of GTP) while we used AMP-PNP (a nonhydrolyzable analog of ATP) for our studies, we performed an extensive analysis of the cryo-EM as well as negatively stained ParM filaments formed in the presence of AMP-PNP or GMP-PNP (Figure 1). The overall reconstruction of the ParM-AMP-PNP filaments from cryo-EM (Figure 1B) was very similar to that derived from the negatively stained filaments (Figure 1D). Unexpectedly, we found that the new reconstruction of cryo-EM ParM-AMP-PNP filaments (Figure 1B) was significantly different from the original reconstruction (Orlova et al., 2007). The nucleotide-binding cleft was closed (Figure 1B), similar to that observed in the negatively stained reconstructions (Figures 1D and 1F). An examination of the original data revealed a mistake in the way the Contrast Transfer Function (CTF) was corrected in those images. This led to an error in the phases of the images, resulting in an artifactual reconstruction.

Negatively stained ParM filaments formed in the presence of AMP-PNP (Figure 1C) look similar to the filaments polymerized in the presence of GMP-PNP (Figure 1E), which is consistent with the similarity of the two respective overall reconstructions (Figures 1D and 1F). Both reconstructions are similar to the reconstruction of ParM-

GMP-PNP filaments from Popp et al. (2008). The only difference that we observe between the negatively stained filaments is a slight increase in the twist heterogeneity in the presence of GMP-PNP (Figure 1I), compared with that found in the presence of AMP-PNP (Figure 1H). In the presence of AMP-PNP, we observed a slight increase in the variance of twist in the cryo set (Figure 1G), compared with that found with negative stain (Figure 1H), but this may reflect a lower signal-to-noise ratio in the frozen hydrated sample.

Solution Studies with ATP versus GTP

In agreement with Popp et al. (2008), we find that the addition of GTP induces polymerization of ParM filaments. To rule out any effects of labeling with fluorescent dyes, we used unlabeled ParM and monitored polymerization by light scattering. At steady state, the apparent critical concentrations of GTP and ATP ParM are approximately equal (not shown). To determine the affinities of ParM for ATP and GTP, we performed competition binding experiments using a fluorescent derivative of ATP (etheno-ATP). To prevent polymerization during the experiment, we used a ParM concentration of 0.4 μM, well below the ATP critical concentration. Competition with unlabeled ATP yielded a dissociation equilibrium constant of 0.9 μM, which is somewhat weaker than the affinity we measured for etheno-ATP (Garner et al., 2004). Competition with GTP yielded a value of 11.6 μM, indicating that, as in all other actin family proteins studied to date, the nucleotide binding pocket of ParM accommodates ATP more readily than GTP (Figure 2A).

In rapid mixing experiments at high nucleotide concentrations (5 mM), GTP-ParM filaments assemble rapidly and spontaneously (Figures 2B and 2C) but slightly

more slowly than ATP-ParM filaments. The rate of polymer assembly at early time points and the concentration dependence of the maximum rate of assembly (Figure 2D) both indicate that GTP ParM assembles via the same mechanism as ATP ParM and with the same apparent nucleus size of 3 monomers ([Flyvbjerg et al., 1996] and [Nishida and Sakai, 1983]). The slower rate of assembly of GTP filaments is consistent with a slower rate of spontaneous nucleation or a slower rate of nucleotide association.

In low concentrations of nucleotide (below 0.5 mM), GTP ParM filaments assemble and spontaneously disassemble in a manner similar to ATP filaments (Figure 3), suggesting that they exhibit a similar nucleotide hydrolysis-dependent dynamic instability. To investigate the polymer dynamics of GTP ParM filaments more carefully, we used total internal reflection fluorescence (TIRF) microscopy of Alexa-488-labeled ParM filaments. Under conditions in which we can observe individual filaments, GTP ParM behaves identically to ATP ParM (Figures 3E and 3F). First we remeasured the dynamics of ATP ParM filaments and obtained rate constants for elongation and catastrophic shortening of 2.9 ± 0.8 μM−1 s−1 (n = 7) and 149 ± 63 s−1 (n = 5), respectively. These values are within a factor of two of those we measured previously (Garner et al., 2004). Like ATP filaments, GTP filaments elongate symmetrically with the same rate constant (2.7 ± 0.8 μM−1 s−1; n = 16) at each end. After a period of steady elongation, GTP filaments also switch to a phase of rapid shortening with the same rate of disassembly as that of ATP ParM (135 ± 63 s−1; n = 5) (Figure 3F). Upon switching from elongation to shortening, both ATP and GTP filaments disassemble completely. We never observe rescue of shortening ParM filaments either in the presence of ATP (Garner

et al., 2004) or GTP (present study). These results differ substantially from those of Popp et al. (2008), and we discuss the discrepancies below.

Symmetry of the Filaments

One of the main arguments that Popp et al. (2008) made for our original ParM filament model being wrong is that we assigned a symmetry to our filament model that does not match the observed X-ray fiber diffraction patterns. Popp et al. (2008) describe the symmetry of their ParM filaments as having 37 subunits in 17 turns of the one-start helix. The repeat, the distance needed to translate a subunit along the axis so that it is in register with another subunit, would be 37*(24.5 Å) = 900, where 24.5 Å is the axial rise per subunit. We have argued (Egelman, 2007) that the description of helical symmetry in terms of a repeat is a poor one, as there is no reason that the symmetry of a helical polymer can be best represented by the ratio of relatively small integers. For a helix having a 37/17 symmetry, the rotation between adjacent subunits would be 360°*17/37, or 165.4°. Consider an almost infinitesimal change in the twist of this structure by 0.04° per subunit. The symmetry is now best approximated as having 3,701 subunits in 1,700 turns, with a repeat of 90,675 Å. It is therefore much more useful to simply describe the angle of rotation between subunits, which is a continuously variable parameter.

Popp et al. (2008) state that we assigned a symmetry of 31 subunits in 14 turns (162.6°) to our ParM filament model. This is untrue. The header of the PDB file (2QU4) for our ParM model that we deposited and that they used for their simulations states that the rotation needed to generate a filament is 165.4° (the same rotation that they describe). We stated in the text of our paper that in the ParM filament the rotation between every other subunit "is on average approximately −29°," which would be a rotation of 165.5°

between subunits. The consequence of this error in the description of our filament symmetry was that the R-factor between our model and their observed X-ray fiber diffraction pattern was great (0.68), but much of this R-factor simply arises from comparing diffraction patterns having two different sets of spacings. Attempting to match our new three-dimensional reconstruction and filament model with their observed X-ray fiber diffraction pattern (Popp et al., 2008) has revealed that ParM filaments cannot be described by a single structural state. In fact, we can now show that globally averaged diffraction patterns from ParM filaments, whether from X-ray scattering or cryo-EM, represent a sum of two states.

Subunits in the ParM Filament Can Exist in Two Different Structural States

The global reconstructions of ParM shown in Figures 1B, 1D, and 1F, as well as from the Maeda group (Popp et al., 2008), are best fit by a subunit having a closed nucleotide-binding cleft. Since ParM has been crystallized in both closed and open forms (van den Ent et al., 2002), we designed two reference volumes composed of protomers having their clefts either closed or open and arranged into filaments having the same helical symmetry as the global reconstruction (Figure 1B). Surprisingly, almost 20% of segments had the higher correlation with the model having its cleft open (Figure 4A). The reconstructions derived from these two classes (Figure 4A) validated the sorting—no perturbations from the crystal structures of the closed and open states of ParM were needed to fit the crystals into the closed and the open reconstructions (filtered to 20 Å resolution), respectively. The sorting did not introduce any bias into the reconstructions, as both sets of images after sorting were reconstructed using the Iterative Helical Real Space Reconstruction (IHRSR) method (Egelman, 2000) starting from a featureless solid cylinder as an initial

model. The IHRSR method has been shown to offer many advantages in the three-dimensional reconstruction of helical polymers that are disordered or heterogeneous (Egelman, 2007). We checked whether segments classified as being in different states came from different filaments, or could be found within the same filaments, by examining the ten longest filaments in our images (data not shown). The conclusion was that all variation (within statistical sampling) was within filaments, and not between filaments.

Previously, we showed that, like F-actin (Egelman and DeRosier, 1982), ParM filaments have a variable twist (Orlova et al., 2007). Surprisingly, sorting by the twist did not improve the resolution of the closed ParM reconstruction (data not shown), suggesting that, in addition to the variable twist, ParM may have other sources of heterogeneity, such as a variable axial rise. The power spectrum of the closed ParM set had a very strong n = 3 layer line (Figure 4E, red arrow), while the reflections from the right and left handed one-start helices were significantly weaker (Figure 4E, blue and green arrows respectively). The power spectrum from the projection of the reconstruction, however, showed significantly stronger one-start layer lines (Figure 5E, blue and green arrows), revealing a discrepancy with the power spectrum from the images used to generate the reconstruction (Figure 4E). A reasonable explanation is that the pitch of the three-start helix is less variable than the pitch of the one-start helices, and such variability would blur the reflections in the averaged power spectrum. The fall in the intensities of layer lines due to the helical disorder has been quantitatively described for F-actin and other helical filaments (Egelman and DeRosier, 1982). Reconstructing with the IHRSR method, on the other hand, would tend to align the one-start helices in spite of

their variability, accounting for the discrepancy. To check this possibility, we designed five models with a fixed three-start helical pitch, but with both variable twist and axial rise (see Experimental Procedures). The frequency distribution from such a sorting is shown in Figure 4B. The classes 2, 3, and 4 were used in the IHRSR procedure and converged to the expected symmetry parameters (Figures 4C and 4D). To validate the sorting independently from the IHRSR method, we calculated the power spectra for these three classes (see Movie S1 available online). As expected, the position of the three-start helix layer line in each power spectrum was fixed, whereas n = 1 and n = −1 layer lines positions moved as predicted. A power spectrum from the largest single class (Figure 4F) shows an enhancement of these one-start layer lines when compared to the average of the five classes (Figure 4E), as expected. Thus, there is a very strong correlation between the twist and the axial rise (Figure 4D), and both show significant variation in ParM filaments.

An obvious question is whether the variability in axial rise could actually be coming from variations in magnification, or from filaments that are tilted out of the plane of the image. If changes in magnification were responsible, then we would see filament reconstructions with different diameters, and we would see shifts in the radial positions of layer line peaks in the power spectra (Movie S1). Such changes are not seen. Further, the determination of twist is independent of magnification, so we would see no correlation between twist and axial rise, but we see a strong correlation, eliminating the possibility that our results can be explained by variable magnification. If the differences in axial rise were due to out-of-plane tilt, then a tilt of 23° would be needed to explain a change in axial rise from 25.5 Å to 23.5 Å. Since the filaments are imaged after adsorption to a

carbon support film and do not lie over holes, this possibility seems extremely unlikely. Our results unambiguously show that, in addition to the variable twist, ParM has a variable axial rise, and that the twist and the axial rise are coupled. We therefore used this new sorting to generate an improved three-dimensional reconstruction of the closed state of the ParM filament, using the largest class (class3, n = 3,116 segments). We did not attempt to sort out the helical heterogeneity in the open ParM state because of the more limited number of total segments (n = 3,374).

The two reconstructions are shown as transparent surfaces in Figures 5A and 5G. To determine the resolution of the map in each case, we used a procedure described in (Galkin et al., 2008), which returned the most pessimistic estimation of the resolution of 17.2 Å for the closed state reconstruction (after sorting for the variable twist and rise) and 19.5 Å for the open state (no sorting for twist and rise). No perturbations of the crystal structure of ParM in the apo-state (PDB 1MWK) were required to dock it into the reconstruction of the open state at the available resolution (Figure 5G). To get a better fit of the ParM crystal structure into the map of the closed state (Figure 5A), we cleaved the apo-crystal structure of ParM across the hinge region into the two major domains (domains I and II), breaking the bonds at the regions where the large change between the ADP and apo states occur (see Experimental Procedures). The best fit was achieved when the two domains were moved toward each other around the hinge by 25° (Figure 5B). Exactly the same closing of the cleft was observed between the apo and ADP (PDB 1MWM) states (Figure 5C) (van den Ent et al., 2002). We found that the docking of separate domains from the apo-crystal produced a slightly better fit than when the unperturbed ADP-state crystal structure was used.

Comparisons of the power spectra of the raw images with those obtained from the reconstructions (Figures 5D, 5E, 5H, and 5I) show good matches, and it can be seen that the power spectrum from the segments classified as closed is different from that obtained from the segments classified as open. For the closed ParM segments, the n = 3 layer line (Figure 5D, red arrow) is more prominent than the n = ± 1 layer lines (Figure 5D, blue and green arrows), while for the open ParM segments, all three layer lines have nearly equal intensity (Figure 5H, red blue and green arrows). This can be measured quantitatively, and the ratio of intensities between the n = 3 and n = 1 layer lines is 2.1 in the closed state (Figure 5D) and 1.0 in the open state (Figure 5H). A similar approach was used to validate our atomic models—the power spectra generated from both atomic models matched well the power spectra of the raw images as well as the power spectra derived from the reconstructions used for the modeling (Figures 5D, 5E, 5F, 5H, 5I, and 5J). To evaluate how well the atomic models reflect the features of the reconstructions we calculated the Fourier Shell Correlation (FSC) between the maps and the atomic models (Figure S1). The FSC curves reached a value of 0.5 (an arbitrary but conservative measure of the resolution limit) at almost exactly the same values that we previously determined for the resolution of these maps, giving further credibility to these resolution estimates.

In our previous work, we showed that there is no nucleotide exchange after ParM polymerization (Orlova et al., 2007), and under the conditions used, AMP-PNP should always be bound in the cleft. Despite the fact that in the presence of GMP-PNP ParM was shown to have its cleft closed (Popp et al., 2008), we observe 20% of segments having the cleft open. We suggest that there is an equilibrium between the closed and the open

state within the ParM filament. When either AMP-PNP or GMP-PNP is bound, the equilibrium is shifted toward the closed state, but a fraction of segments can still be found in the open state.

A detailed comparison of the atomic models of the closed and open states of the ParM filament (Figure 6) shows how protomer interfaces change between these two states. In the closed state, each ParM promoter makes three longitudinal contacts and one lateral contact with its neighbors (Figures 6A and 6B). In the open state (Figures 6C and 6D), the residues 161–164 and 271–274 of the upper protomer and the residues 212–217 of the lower protomer move away from each other (Figures 6A and 6C, red arrows). Also, the contact between the residues 298–300 of the upper protomer and residues 239–341 of the lower protomer is broken in the open state (Figures 6A and 6C, green arrows). Our atomic models predict that, upon opening of the nucleotide binding cleft, the ParM filament would be less stable than when it is in the closed state.

Both atomic models are in agreement with the recent mutagenesis data. It has been shown that point mutations of residues 33, 34, 36, and 40 completely abolish ParM polymerization (Salje and Lowe, 2008). In both ParM states, these residues lie at the interface between protomers (Figure 6, residues are marked as spheres). Mutation of residue K123, which is located in helix 4 of domain I of ParM (van den Ent et al., 2002), does not affect ParM polymerization but abolishes the interaction of ParM with the ParR/*ParC* complex. In our atomic models, this residue is located at the side of the filament (Figures 6A–D, red arrow heads), which would explain why this mutation does not alter ParM polymerization and why binding of ParR/*ParC* complex does not interfere with ParM polymerization. Both atomic models also show that the interfaces between

protomers are completely different from that found in F-actin. This is consistent with the fact that there is no correspondence of secondary structural elements between ParM and actin (Figure 6E) in the regions of the actin subunit that are known to be involved in the filament interface. For example, mutation of actin residues 204 and 243 has been shown to abolish polymerization (Rould et al., 2006), but there is no structural similarity between ParM and actin in this region of the actin subunit (Figure 6E). Similarly, the "hydrophobic plug" in actin (residues 262–274) has been shown to be essential for filament formation (Reisler and Egelman, 2007), but this element is completely missing from ParM (Figure 6E).

The Opening of the Cleft Is Coupled with ATP Hydrolysis

To elucidate the role of the two structural states of ParM filaments found, we imaged ParM filaments under several other conditions (Figure 7). We first determined that negative stain can be used to visualize the two different states. Although we found a smaller fraction of the open state of ParM in the negatively stained AMP-PNP-ParM (Figure 7A) sample (10%), compared with the frozen hydrated filaments (20%), the negatively stained reconstructions of the open (Figure 7H) and closed (Figure 7G) states of ParM were very similar at the available resolution to the cryo-EM reconstructions (Figures 5A and 5G, respectively).

When ParM was polymerized in the presence of a large molar excess (5.0 mM) of ATP (Figure 7B), we observed long and quite ordered filaments. These filaments disappeared over time as the ATP was consumed (Figure 7C). Image analysis revealed that over 20% of these ordered segments were in the open conformation (Figure 7I), suggesting that the opening of the nucleotide-binding cleft in ParM was associated with

ATP hydrolysis (since 10% of these segments had an open cleft with the nonhydrolyzable AMP-PNP). Using a lower concentration of ATP (0.5 mM) resulted in shorter filaments after 5 min of polymerization (Figure 7D), and almost no filaments were observed after 30 min (Figure 7E). The addition of BeF_3^-, used to mimic the ADP-Pi state in F-actin (Combeau and Carlier, 1988), rescues ParM filaments from depolymerization (Garner et al., 2004). When BeF_3^- was added shortly after polymerization at low ATP concentration (see Experimental Procedures), even after 30 min we observed long ParM filaments (Figure 7F). Interestingly, in comparison to AMP-PNP-filaments (Figure 7A), or ATP-filaments after short times (Figure 7B), BeF_3^-filaments (Figure 7F) had a quite different appearance, similar to the "ragged" morphology of F-actin after short times of polymerization ([Steinmetz et al., 1997] and [Orlova et al., 2004]). Cross-correlation sorting revealed that the majority of these segments were in the open state (Figure 7I), and showed that BeF_3^- stabilized the open conformation of the ParM subunits in the filament.

Discussion

Nucleotide Preference of ParM

ParM is a member of the actin superfamily, which includes eukaryotic actins, actin-related proteins (ARPs), prokaryotic actin-like proteins (ALPs), chaperones (Hsc70 and DnaK), and sugar kinases (e.g., hexokinase). The family is defined by a shared nucleotide-binding motif called the "actin fold" (Bork et al., 1992) which, in all known cases, prefers ATP over GTP. For some family members, this preference is not strong. DnaK and some forms of hexokinase, for example, are only two- to four-fold more selective for ATP over GTP (Liberek et al., 1991). Most conventional eukaryotic actins bind 500–1000 times more tightly to ATP than GTP, although some actins are less discriminating. The best studied example of a weakly discriminating actin is that of budding yeast, which has only nine-fold greater affinity for ATP. In the presence of GTP, yeast actin assembles into filaments indistinguishable from ATP filaments, with a critical concentration only five-fold higher than in the presence of ATP (Wen et al., 2002). The difference in nucleotide selectivity between yeast and animal actins is due, in large part, to a single amino acid difference in the nucleotide binding pocket (Phe versus Tyr at position 305), a substitution that is widely conserved among fungi and plants and suggests a selective advantage for the ability to utilize GTP. van den Ent et al. (2002) also showed that the bacterial actin like protein MreB will polymerize in both ATP and GTP but did not determine nucleotide binding preference.

Popp et al. (2008) recently showed that ParM can also polymerize in the presence of GTP. Although these authors did not measure the relative affinities of ParM for different nucleotides, they suggested that, unlike other members of the actin superfamily, ParM prefers GTP over ATP and is "a predominantly GTP-driven molecular switch." To determine whether this is the case, we measured the affinities of ParM for ATP and GTP by competition binding and found that, similar to yeast actin, ParM has a 10-fold higher affinity for ATP. Thus, at cellular ratios of ATP to GTP (generally >1.0), ParM will be predominantly ATP bound.

Popp et al. (2008) also report that, while ATP ParM filaments undergo dynamic instability, rapid shortening of filaments is often terminated by "rescue," and the filaments rarely or never completely disassemble. In contrast, they report that, upon switching from elongation to shortening, GTP ParM filaments disassemble completely. We also compared the assembly dynamics of ATP and GTP ParM using bulk light scattering assays and TIRF microscopy. In agreement with Popp et al. (2008), we find that the apparent critical concentrations of ATP and GTP ParM are identical, suggesting that the filaments have a similar stability, and by use of TIRF microscopy, we find no difference in the behavior of individual GTP and ATP ParM filaments. Both elongate bidirectionally and, upon switching to disassembly, both depolymerize completely. Some discrepancies between our results and those of Popp et al. (2008) are likely due to the fact that Popp et al. (2008) performed TIRF experiments on large filament bundles generated by a crowding agent, polyvinyl alcohol. The difference in the state of the protein under the two different imaging conditions is dramatic. Under our conditions, almost all observed filaments are short (<3 μM), uniform in intensity, unbranched, and highly

dynamic. Electron microscopy of filaments prepared under these conditions confirms that fewer than 2% are associated with other filaments ([Garner et al., 2004] and [Choi et al., 2008]). In Popp et al. (2008), almost all observed filaments are >5 μm in length, of variable fluorescence intensity, and often display branching or fraying at the ends, typical of filament bundles. Lateral interactions within a large bundle could act to stabilize filaments, and it is possible that GTP filaments have a lower propensity to form tight bundles than ATP filaments. This, however, cannot explain all the discrepancies between our results. In a previous study, we used methylcellulose to form long, stable bundles of ATP ParM filaments between particles coated with ParR/*parC* complexes. When we cut the bundles in the middle to expose ADP filament ends, both halves of the bundle completely disassembled, despite the presence of the crowding agent. Another potential source of difference could be our fluorescent labeling protocols. Popp et al. (2008) use ParM labeled randomly with multiple rhodamine molecules on surface-exposed lysines. In our hands, rhodamine-labeled ParM has a dramatically enhanced tendency to bundle, even in the absence of crowding agents (data not shown). In our TIRF experiments, we used ParM labeled with a single Alexa-488 on an engineered C-terminal cysteine. Our data disagree with the view that ParM is "a predominantly GTP-driven molecular switch" and support the idea that, like other members of the actin superfamily, ParM is a preferential ATPase with the capacity to bind GTP, albeit with a lower affinity.

Equilibrium Between Open and Closed States of the ATP-Binding Cleft Is Common to Proteins of the Actin Superfamily

A number of papers have proposed an atomic model of the ParM filament ([van den Ent et al., 2002], [Orlova et al., 2007] and [Popp et al., 2008]). We think that the

structural heterogeneity within the ParM filament precludes the formulation of a single atomic model for the ParM filament. The majority of segments in the presence of AMP-PNP have subunits with a closed cleft, and the atomic model derived from this state is consistent with the recently published ParM model (Popp et al., 2008). The second structural state, where protomers have their cleft open to the same extent as seen in the apo crystal structure of ParM (van den Ent et al., 2002), is also present in filaments, even though the same nucleotide (AMP-PNP) is believed bound to both states. The evidence for a bound nucleotide in both states comes from the observation (Orlova et al., 2007) that there is no appreciable exchange of nucleotide in these filaments. The notion that a bound ligand may bias a distribution of states of a protein, rather than simply determining the conformation, has been described in many other systems. For example, it has been shown that there is an equilibrium between the discrete positions of tropomyosin on F-actin that is shifted by Ca2+, as opposed to being directly linked to the divalent cation (Pirani et al., 2005).

The two structural states of ParM that we observe are very similar to the two states previously visualized by crystallography (van den Ent et al., 2002), and support the notion that all members of the actin superfamily can undergo large domain-domain motions (Bork et al., 1992). Recent observations of another bacterial actin homolog, AlfA, suggest that the subunits within the AlfA filament are mainly in an open conformation (Polka et al., 2009). It has been suggested that the opening of the nucleotide binding cleft in F-actin is coupled with ATP hydrolysis (Belmont et al., 1999). Within crystals of G-actin, the binding of ATP or ADP does not change the opening of the cleft (Rould et al., 2006), but it is possible that crystal-packing interactions may trap actin in

the closed state. We have found both states of an actin subunit coexisting in actin filaments—the canonical state has the ATP-binding cleft closed (Galkin et al., 2008), while in the tilted state of F-actin the cleft is open ([Galkin et al., 2002] and [Orlova et al., 2007]). This suggests that in the mature actin filament, containing ADP-bound protomers, there is an equilibrium between the two states. While this equilibrium is shifted toward the closed state, ADP-protomers having their cleft open can still be found in actin filaments.

The Closed State of the Cleft Is Required but Not Sufficient for ParM Polymerization

Actin can form filaments in presence of ATP, ATP analogs, ADP, and even without any nucleotide bound, so modifications to impair its ability to polymerize, or cocomplexes with other proteins, are required for the crystallization of actin. This is consistent with the very small differences between the nonpolymerizable ATP-bound and ADP-bound crystals of actin that mainly involve subtle movement of the sensor loop (Rould et al., 2006). Is the opening of the ATP-binding cleft in ParM coupled with ATP hydrolysis? In contrast to actin, ParM can polymerize only in the presence of NTP, or NTP analogs such as AMP-PNP or GMP-PNP. This suggests that ParM monomers that have ATP bound are structurally different from ADP-ParM monomers. A crystal structure of nonpolymerizable ATP-ParM is required to understand what precludes ADP-ParM from forming filaments.

It was shown that BeF_3^- stabilizes actin filaments by mimicking the ADP-Pi state of the filament (Combeau and Carlier, 1988). Interestingly, BeF_3^- can rescue ParM filaments from the fast depolymerization that occurs upon ATP hydrolysis but does not

promote filament elongation (Garner et al., 2004). Our EM observations show the stabilization of the preformed ParM filaments by BeF_3^- after the depletion of ATP (Figures 7D–7F). Together, these results imply the existence of at least two structural states of the ParM monomers—one structural state allows them to polymerize, while the other state can occur only in the preformed filament, and monomers in this state can not spontaneously polymerize. We found that in the presence of BeF_3^- after the depletion of ATP the majority of segments had the cleft widely open (Figure 7I). This strongly suggests that the open state of the ParM filament is the dominant form in the ADP-Pi state, but monomers with the open cleft can not support elongation or form new filaments. The closed state of the cleft is required but not sufficient for ParM polymerization.

In the model proposed by Popp et al. (2008), both the GTP- and GDP-bound ParM monomers in a filament adopt a similar "closed" conformation. When GDP ParM monomers are exposed at the end of a filament, the loss of nucleotide causes a change in conformation from the "closed" to the "open" state and promotes monomer dissociation. That is, catastrophic shortening requires that the terminal ParM monomer in the filament be in the nucleotide-free or apo form. The requirement that the rapidly dissociating monomers are nucleotide-free appears to be based entirely on the fact that in the crystal structures solved by the Lowe group, ADP ParM appears in a closed conformation while apo ParM is open. We find that ParM filaments contain monomers in both the open and closed form and that the relative amounts in each form depend on the nucleotide bound. Thus, there is no need to invoke the existence of apo ParM monomers to explain a conformational change-driven increase in the rate of monomer dissociation from filament

ends. Furthermore, we previously (Garner et al., 2004) found that addition of exogenous ADP to preformed ParM filaments increased their rate of disassembly. The best explanation for this observation is that, as in conventional actin (Teubner and Wegner, 1998), the terminal monomers of a ParM filament can exchange bound nucleotide with nucleotides in solution. If ADP ParM monomers were more stable than apo monomers, the addition of excess ADP should slow down dissociation rather than accelerate it.

The Opening of the ATP-Binding Cleft May Be Required for Phosphate Release

After short times of polymerization, when F-actin hydrolyzes ATP and releases the inorganic phosphate, filaments have a ragged morphology that evolves over time into more ordered filaments ([Steinmetz et al., 1997] and [Orlova et al., 2004]). This ragged morphology coincides with the increased number of actin protomers in the tilted state ([Galkin et al., 2002] and [Orlova et al., 2004]). In the tilted state, F-actin has its cleft open and lacks one of its longitudinal contacts ([Galkin et al., 2002] and [Orlova et al., 2004]). These observations explain why young actin filaments are less stable than aged ones (Kueh et al., 2008). In the mature frozen hydrated actin filaments, the majority of segments are in the closed state (Orlova et al., 2007), which is consistent with the closed cleft observed in the crystal structure of ADP-G-actin (Rould et al., 2006). This suggests that in F-actin the opening of the cleft is coupled with ATP hydrolysis, and once this process is completed the cleft closes.

Stabilization of ParM filaments with BeF_3^- provides insight into what happens to protomers upon ATP hydrolysis. We show here that ParM protomers in the ADP-Pi state (mimicked by BeF_3^-) are mainly in the open form. Importantly, ParM filaments that are stabilized with BeF_3^- after ATP depletion a have ragged morphology (Figure 7F) similar

to that observed in young actin filaments. Since actin and ParM have a substantial structural homology in the ATP-binding cleft region, we suggest that the opening of the ATP-binding cleft in the tilted state of F-actin, similar to what is seen with ParM, reflects the ADP-Pi state.

Why is ParM, in contrast to F-actin, dynamically unstable? We may speculate that once the inorganic phosphate is released, the cleft in F-actin closes and it returns to the stable conformation. ParM is structurally homologous to actin only in the core region, while it is very different from F-actin in the regions of subunit-subunit contacts within the filament. This explains why ParM forms left-handed two-start helices with contacts between the protomers that are absolutely unrelated to the contacts observed in F-actin (Figure 6). It is possible that because of this difference, the cleft in ParM can not be closed upon phosphate release, and protomers can not switch back to the closed state. The open conformation of ParM that we describe as the ADP-Pi state is an intermediate state between the stable ATP-filament and highly unstable ADP-filament. ParM filaments shrink from the ends (Garner et al., 2004). The structural alterations in the ParM filament that arise from the opening of the cleft in the ADP-Pi state preclude the addition of ATP-bound protomers to the ends of the filament, and thus prevent the formation of the protective ATP caps (Figure 8). The structural changes in ParM that accompany Pi release are inconsistent with filament existence.

Implications for ParR/*ParC* Binding

Atomic models derived from both open and closed states are consistent with the mutagenesis data (Salje and Lowe, 2008) and place the ParR/*ParC*-binding site on the side of the ParM filament. We suggest that alteration of the side of the filament upon

ATP hydrolysis allows the ParR/*ParC* complex to sense the nucleotide state of the filament and remain attached to subunits within the ATP cap. Since filaments capped with the ParR/*ParC* complex are stable and can grow to be long in the cell (Campbell and Mullins, 2007), it is likely that interaction of the ParR/*ParC* complex with the side of the filament may stabilize the ATP cap.

Experimental Procedures

Sample Preparation and Electron Microscopy

ParM protein was overexpressed and purified as described elsewhere (Orlova et al., 2007). ParM in 30 mM Tris-HCL (pH 7.5), 0.1 M KCL, 2 mM $MgCl_2$, and 1 mM DTT was diluted to 3–-4 μM, and polymerized by the addition of AMP-PNP (5 mM) or GMP-PNP (5 mM); after 5–10 min incubation, 5 μl was applied to glow-discharged carbon-covered 300-mesh copper grids. Alternatively, polymerization was started by the addition of 100 μM–5 mM ATP. For ADP-Pi state, 1 mM BeSO4 and 5 mM NaF were added after 2–4 min of polymerization. The mixture was incubated up to 15–30 min at room temperature.

The grids were either negatively stained with 1% (w/v) uranyl acetate or blotted and plunged into liquid ethane. Images were collected on film using a Tecnai 12 (80 kV and ×30,000 magnification) for negatively stained samples or a Tecnai 20 FEG (200 kV and ×50,000 magnification) for frozen-hydrated samples. The 31 different images used for the cryo-EM reconstruction had defocus values ranging from 2.0 to 4.0 μm. Films were scanned on a Nikon Coolscan 8000 with a sampling of 4.16 Å per pixel for negative-stain images and 2.38 Å per pixel for cryo-EM.

Image Analysis

The SPIDER package (Frank et al., 1996) was used for most image processing, but the BSOFT package (Heymann and Belnap, 2007) was used to determine the defocus values in the micrographs while EMAN (Ludtke et al., 1999) package was used to extract filament images from micrographs.

Image Analysis of Frozen Hydrated AMP-PNP-ParM-Filaments

All cryo-EM images were multiplied by the theoretical CTF to correct for phase reversals and to optimize the signal-to-noise ratio. Final reconstructions were then divided by the weighted sum of the squared CTFs and corrected for the envelope function of the EM with the use of negative B-factors. The segments were classified as shown in Figure 4A. First, a global reconstruction was generated using all segments (n = 18,870). The crystal structure of the closed state of ParM (PDB entry 1MWK) was docked into the global map using the UCSF Chimera software (Pettersen et al., 2004), and subsequently used to generate a model filament in the closed state. The ParM crystal structure in the open state (PDB entry 1MWK) was used to generate a model filament having the cleft open. The position of the first domain of ParM in the closed and the open states models were identical, so the only difference was the opening of the cleft and the breakage of the contact between the protofilaments (Figure 6, red and green arrows). These models were used as references for an initial sorting (Figure 4A). These two reference volumes were scaled to 4.76 Å per pixel and projected into 100 × 100-pixel images with an azimuthal rotational increment of 4°, generating 180 reference projections (2 × 90). The ParM segments were down-sampled to 4.76 Å per pixel and cross-correlated with the 180 reference projections. Reconstructions were independently generated from the two classes of segments—closed (n = 12,523), and open (n = 3,374). The validity of the sorting was confirmed by two independent means. First, power spectra of segments from both classes were indistinguishable from the power spectra of the 3D reconstructions (Figure 5). Second, we used the IHRSR approach (Egelman, 2000) to show the convergence of the two classes to their unique solutions independently form the starting

point (Figure S2). The 3D reconstruction of the open set yielded symmetry of 165°/24.2Å and was used to build up an atomic model of the ParM filament in the open state (Figures 6C and 6D). The closed set was sorted by the twist and the axial rise. Five model volumes were created by imposing five corresponding symmetries on the crystal structure of ParM in the closed state (PDB entry 1MWM). The symmetries were chosen to keep the pitch of the three-start helix fixed at 1/194 Å−1 as follows: 160.7°/21.87Å, 163°/23.11Å, 165.2°/24.3Å, 167.5°/25.51Å, and 169.7°/26.73Å. These five volumes were scaled to 4.76 Å per pixel and projected into 100 × 100-pixel images with an azimuthal rotational increment of 4°, generating 450 reference projections (5 × 90). The ParM segments were down-sampled to 4.76 Å per pixel and cross-correlated with the 450 reference projections. The power spectra of segments from three largest bins were calculated (Movie S1), and behave exactly as predicted by the twist and axial rise values shown in the histogram (Figure 4B). Second, we used the IHRSR approach to separately reconstruct these three bins, and each class converged to the expected symmetry (Figures 4C and 4D). The reconstruction form the largest class number 3 (n = 3,611) iterated at the original scale of 2.38 Å per pixel yielded the symmetry of 165.2°/24.3Å, and was used to build up an atomic model of the ParM filament in the closed state (Figures 6A and 6B).

To validate our maps, we iterated each set from the two very different symmetries to check the convergence of the set to the same solution (Figure S2). We observed a nice convergence to the same solution within each set. Our extensive work with IHRSR package proved that heterogeneous sets would never generate the same 3D reconstruction if iterated from the different starting points. Also, to avoid model biasing, both sets were reconstructed starting from a features solid cylinder (Figure S2).

The conservative FSC = 0.5 criterion was used for resolution determination. A widely used approach has been to split an aligned data set into two halves yielding two volumes for FSC comparison, but this method can yield an overly optimistic resolution value due to alignment of noise. To avoid that, we divided the images into two sets and then used the IHRSR procedure on these two sets starting each from a different helical symmetry. The two structures converge to a common symmetry, and the resultant volumes did not have noise aligned to a common reference. However, the smaller number of images present in each half data set would underestimate the resolution in the combined reconstruction, under conditions where the resolution was likely to be limited by the number of particles. Thus, the 17.2 Å resolution that was measure by this method in our closed map, and the 19.5 Å resolution determined for the open state, were the most pessimistic resolution estimations.

Image Analysis of Negatively Stained Samples

We extracted 10,181 overlapping segments of negatively stained AMP-PNP ParM filaments, and 11,173 segments prepared in presence of GMP-PNP, each 416 Å in length. First, a global reconstruction of each set was generated using all segments. After 60 cycles of IHRSR refinement, the AMP-PNP set yielded a stable solution of 165.2°/24.7 Å (Figure 1B, gray surface), while the GMP-PNP set converged to 165.3°/24.7 Å (Figure 1C, gray surface). This global reconstruction of the AMP-PNP set was then deformed into nine different twist states ranging from 157 to 173° with a step of 2°, and these models were used as references for the twist sorting (Figures 1G–1I).

We selected 4,726 segments of ParM formed in the presence of 0.5 mM ATP after 5 min of polymerization. Similarly to the frozen hydrated sample, segments were divided

into the two classes on the basis of the opening of the nucleotide binding cleft. The majority of segments (n = 3,680) had the better correlation with the closed cleft reference, and yielded an IHRSR reconstruction shown in (Figure 7G) with the symmetry of 165.2°/24.7 Å. The smaller set that represented the open state subset (n = 1,046) converged to 164.8°/24.8 Å symmetry.

Filaments formed in presence of 0.5 mM ATP and subsequently stabilized with the addition of 2 mM BeF_3^- possessed a ragged morphology (Figure 7F). We selected only segments that were straight within the 416 Å long box, which was the length of the segments used in IHRSR procedure. Thus, only 1,070 segments were selected and sorted into two classes on the basis of the structural state. More than half of the images (n = 599) were assigned to the open state class and yielded a reconstruction shown in (Figure 7H), having the symmetry of 165.4°/24.7 Å. The smaller subset that represented the closed state converged to 164.8°/24.9 Å symmetry.

References

1. Belmont, L.D., Orlova, A., Drubin, D.G., and Egelman, E.H. (1999). A change in actin conformation associated with filament instability after Pi release. Proc. Natl. Acad. Sci. USA 96, 29–34. Bork, P., Sander, C., and Valencia, A. (1992). An ATPase domain common to prokaryotic cell cycle proteins, sugar kinases, actin, and hsp70 heat shock proteins. Proc. Natl. Acad. Sci. USA 89, 7290–7294.
2. Campbell, C.S., and Mullins, R.D. (2007). In vivo visualization of type II plasmid segregation: bacterial actin filaments pushing plasmids. J. Cell Biol. 179, 1059–1066. Choi, C.L., Claridge, S.A., Garner, E.C., Alivisatos, A.P., and Mullins, R.D. (2008). Protein-nanocrystal conjugates support a single filament polymerization model in R1 plasmid segregation. J. Biol. Chem. 283, 28081–28086. Combeau, C., and Carlier, M.F. (1988). Probing the mechanism of ATP hydrolysis on F-actin using vanadate and the structural analogs of phosphate BeF_3^- and A1F-4. J. Biol. Chem. 263, 17429–17436.
3. Egelman, E.H. (2000). A robust algorithm for the reconstruction of helical filaments using single-particle methods. Ultramicroscopy 85, 225–234. Egelman, E.H. (2007). The iterative helical real space reconstruction method: surmounting the problems posed by real polymers. J. Struct. Biol. 157, 83–94. Egelman, E.H., and DeRosier, D.J. (1982). The Fourier transform of actin and other helical systems with cumulative random angular disorder. Acta Crystal- logr. A 38, 796–799.
4. Flyvbjerg, H., Jobs, E., and Leibler, S. (1996). Kinetics of self-assembling microtubules: an ‘‘inverse problem’’ in biochemistry. Proc. Natl. Acad. Sci. USA 93, 5975–5979. Frank, J., Radermacher, M., Penczek, P., Zhu, J., Li, Y., Ladjadj, M., and Leith, A. (1996). SPIDER and WEB: Processing and visualization of images in 3D electron microscopy and related fields. J. Struct. Biol. 116, 190–199.
5. Galkin, V.E., Orlova, A., Cherepanova, O., Lebart, M.C., and Egelman, E.H. (2008). High-resolution cryo-EM structure of the F-actin-fimbrin/plastin ABD2 complex. Proc. Natl. Acad. Sci. USA 105, 1494–1498. Galkin, V.E., VanLoock, M.S., Orlova, A., and Egelman, E.H. (2002). A new internal mode in F-actin helps explain the remarkable evolutionary conserva- tion of actin’s sequence and structure. Curr. Biol. 12, 570–575.
6. Garner, E.C., Campbell, C.S., and Mullins, R.D. (2004). Dynamic instability in a DNA-segregating prokaryotic actin homolog. Science 306, 1021–1025. Garner, E.C., Campbell, C.S., Weibel, D.B., and Mullins, R.D. (2007). Reconsti- tution of DNA segregation driven by assembly of a prokaryotic actin homolog. Science 315, 1270–1274.
7. Gerdes, K., and Molin, S. (1986). Partitioning of plasmid R1. Structural and functional analysis of the parA locus. J. Mol. Biol. 190, 269–279.

8. Heymann, J.B., and Belnap, D.M. (2007). Bsoft: image processing and molecular modeling for electron microscopy. J. Struct. Biol. 157, 3–18.
9. Jensen, R.B., and Gerdes, K. (1997). Partitioning of plasmid R1. The ParM protein exhibits ATPase activity and interacts with the centromere-like ParR-*parC* complex. J. Mol. Biol. 269, 505–513.
10. Kueh, H.Y., Brieher, W.M., and Mitchison, T.J. (2008). Dynamic stabilization of actin filaments. Proc. Natl. Acad. Sci. USA 105, 16531–16536.
11. Liberek, K., Skowyra, D., Zylicz, M., Johnson, C., and Georgopoulos, C. (1991). The Escherichia coli DnaK chaperone, the 70-kDa heat shock protein eukaryotic equivalent, changes conformation upon ATP hydrolysis, thus trig- gering its dissociation from a bound target protein. J. Biol. Chem. 266, 14491–14496.
12. Lowe, J., and Amos, L.A. (2009). Evolution of cytomotive filaments: The cytoskeleton from prokaryotes to eukaryotes. Int. J. Biochem. Cell Biol. 41, 323–329.
13. Ludtke, S.J., Baldwin, P.R., and Chiu, W. (1999). EMAN: semiautomated software for high-resolution single-particle reconstructions. J. Struct. Biol. 128, 82–97.
14. Moller-Jensen, J., Borch, J., Dam, M., Jensen, R.B., Roepstorff, P., and Gerdes, K. (2003). Bacterial mitosis: ParM of plasmid R1 moves plasmid DNA by an actin-like insertional polymerization mechanism. Mol. Cell 12, 1477–1487.
15. Nishida, E., and Sakai, H. (1983). Kinetic analysis of actin polymerization. J. Biochem. 93, 1011–1020.
16. Nordstrom, K., Molin, S., and Agaard-Hansen, H. (1980). Partitioning of plasmid R1 in Escherichia coli. I. Kinetics of loss of plasmid derivatives deleted of the par region. Plasmid 4, 215–227.
17. Oda, T., Iwasa, M., Aihara, T., Maeda, Y., and Narita, A. (2009). The nature of the globular- to fibrous-actin transition. Nature 457, 441–445.
18. Orlova, A., Garner, E.C., Galkin, V.E., Heuser, J., Mullins, R.D., and Egelman, E.H. (2007). The structure of bacterial ParM filaments. Nat. Struct. Mol. Biol. 14, 921–926.
19. Orlova, A., Shvetsov, A., Galkin, V.E., Kudryashov, D.S., Rubenstein, P.A., Egelman, E.H., and Reisler, E. (2004). Actin-destabilizing factors disrupt filaments by means of a time reversal of polymerization. Proc. Natl. Acad. Sci. USA 101, 17664–17668.
20. Pettersen, E.F., Goddard, T.D., Huang, C.C., Couch, G.S., Greenblatt, D.M., Meng, E.C., and Ferrin, T.E. (2004). UCSF Chimera–a visualization system for exploratory research and analysis. J. Comput. Chem. 25, 1605–1612.
21. Pirani, A., Xu, C., Hatch, V., Craig, R., Tobacman, L.S., and Lehman, W. (2005). Single particle analysis of relaxed and activated muscle thin filaments. J. Mol. Biol. 346, 761–772.
22. Polka, J., Kollman, J.M., Agard, D.A., and Mullins, R.D. (2009). The structure and assembly dynamics of a plasmid actin, AlfA, imply a novel method of DNA segregation. J. Bact., in press.
23. Popp, D., Narita, A., Oda, T., Fujisawa, T., Matsuo, H., Nitanai, Y., Iwasa, M., Maeda, K., Onishi, H., and Maeda, Y. (2008). Molecular structure of the ParM polymer and the mechanism leading to its nucleotide-driven dynamic instability. EMBO J. 27, 570–579.

24. Reisler, E., and Egelman, E.H. (2007). Actin structure and function: what we still do not understand. J. Biol. Chem. 282, 36133–36137.
25. Rould, M.A., Wan, Q., Joel, P.B., Lowey, S., and Trybus, K.M. (2006). Crystal structures of expressed non-polymerizable monomeric actin in the ADP and ATP states. J. Biol. Chem. 281, 31909–31919.
26. Salje, J., and Lowe, J. (2008). Bacterial actin: architecture of the ParMRC plasmid DNA partitioning complex. EMBO J. 27, 2230–2238.
27. Steinmetz, M.O., Goldie, K.N., and Aebi, U. (1997). A correlative analysis of actin filament assembly, structure and dynamics. J. Cell Biol. 138, 559–574.
28. Teubner, A., and Wegner, A. (1998). Kinetic evidence for a readily exchangeable nucleotide at the terminal subunit of the barbed ends of actin filaments. Biochemistry 37, 7532–7538.
29. van den Ent, F., Moller-Jensen, J., Amos, L.A., Gerdes, K., and Lowe, J. (2002). F-actin-like filaments formed by plasmid segregation protein ParM. EMBO J. 21, 6935–6943.
30. Wen, K.K., Yao, X., and Rubenstein, P.A. (2002). GTP-yeast actin. J. Biol. Chem. 277, 41101–41109.

Figure Legends

Figure 1. EM Images of ParM Filaments in the Presence of AMP-PNP and GMP-PNP with Corresponding Global Reconstructions and Twist Distributions (A) Frozen hydrated and (C) negatively stained ParM filaments polymerized in the presence of AMP-PNP. (E) Same as (C), but with GMP-PNP rather than AMP-PNP. The global 3D reconstructions derived from the segments in (A, C, and E) are shown as solid surfaces in (B, D, and F), respectively. Twist distributions of frozen hydrated (G) and negatively stained (H) AMP-PNP ParM filaments. (I) Twist distribution of the GMP-PNP negatively stained ParM. The scale bar in (E) is 1,000 A .

Figure 2. ParM Accommodates ATP and GTP

(A) Competition of etheno-ATP away from ParM by ATP and GTP. The affinity of ParM for ATP (Kd = 0.9 mM) is more than 10-fold higher than for GTP (Kd = 11.6 mM). The experiment was performed three times with identical results. Conditions: Buffer: 100 mM KCl, 1 mM MgCl2, 10 mM HEPES (pH 7.0). Temperature: 24 C. (B) Assembly of five different concentrations of R1 ParM initiated by addition of 5 mM ATP. (C) Assembly of the same concentrations of ParM initiated by addition of 5 mM GTP. Polymerization was monitored by right angle light scattering and the ampli- tude of the light scattering signal normalized to the value at plateau. Time scales were normalized to the time required to reach 10% of the plateau value. Insets: raw data before normalization. The similarity of the slopes of the curves at early time points indicates that, in each case, the nucleation mechanism is the same at all concentrations tested. (D) Log-log plot of the normalized maximum velocity of polymerization versus ParM concentration. The identical slopes

argue that the mechanism of nucleation is the same in both cases. The offset between the lines suggests that spontaneous nucleation is slightly faster in the presence of ATP.

Figure 3. Effects of Varying Nucleotide Concentration on Assembly and Stability of R1 ParM Filaments

Polymerization of 10 mM R1 ParM was initiated by addition of varying amounts of ATP (A, C) or GTP (B, D). For all concentrations between 0.05 mM and 5 mM, polymer content reached its maximum value within 10 s (A, B). The initial phase of assembly was less sensitive to variations in the concentration of ATP (A) compared to GTP (B), suggesting that the association of GTP is slower than that of ATP. Once assembled, ParM polymer has similar stability at the same concen- trations of ATP and GTP (C, D). In 5 mM ATP (C) or GTP (D), the polymer content remains constant for many minutes. At concentrations below 0.5 mM, the polymer content decreases significantly within 150 s, and, at concentrations below 0.1 mM, polymer completely disappears within 120 s. TIRF microscopy of ParM fila- ments assembled in ATP (E) or GTP (F). The rates of elongation and disassembly of individual filaments are identical under the two conditions.

Figure 4. Sorting of Frozen Hydrated ParM Filaments by Both the Structural State and the Helical Symmetry (A) Closed crystal structure (red ribbons, PDB 1MWM) and the open crystal structure (blue ribbons, PDB 1MWK) were used to generate two reference models (solid surfaces). These models were used to sort out short segments of ParM into classes based on the opening of the nucleo- tide-binding cleft (yellow bins). (B) Five reference models were designed (see Experimental Procedures) to classify closed-cleft segments on the basis of their twist and axial rise. Frequency counts of observed filament seg- ments are shown as gray bins, while black circles represent the

corresponding class symmetry. (C) Convergence of classes of images from (B) in the IHRSR procedure validates the sorting shown in (B). (D) The stable solutions after convergence (C) show a strong coupling between the twist and the axial rise. Power spectrum of all closed-cleft segments (E) is compared with the power spec- trum from class3 (F), the largest class in (B). Three layer lines are marked with arrows: n = 3 is red, n = 1 is blue, and n = 1 is green. The layer lines from the one-start helices are stronger in (F) than they are in the global average (E), due to reduced heterogeneity after the symmetry sorting.

Figure 5. The Two Pseudo-Atomic Models of the ParM Filament

(A) Reconstruction of the ParM filament in the closed state is filtered to 17 A resolution, and the corresponding atomic model is shown as red ribbons. (B) The two domains of the APO crystal structure of ParM (blue ribbons) have to be moved toward each other by 25 (red ribbons) to achieve a better fit to the closed state filament (see text for details). (C) The same closing of the nucleotide-binding cleft is observed between the APO (blue ribbons) and ADP-bound (green ribbons) crystal structures. (D–F) Power spectra generated from the raw images (D), and projections of either the three-dimensional reconstruction (E) or the corresponding atomic model of the closed filament (F). Three layer lines are marked with arrows: n = 3 is red, n = 1 is blue, and n = 1 is green. (G–J) (G) Three-dimensional reconstruction of the ParM filament in the open state is filtered to 19 A resolution, and the corresponding atomic model is shown as blue ribbons. Power spectra generated from the raw images (H), and projections of either the three-dimensional reconstruction (I) or the corresponding atomic model of the open filament (J). Three layer lines are marked with arrows as in (E).

Figure 6. Detailed Views of the Two Structural States of the ParM Filament (A and B) Pseudo-atomic model of the closed state is shown as ribbons, and the corresponding view of the model filtered to 10 A resolution is shown as a transparent surface. The two views are related by 90 rotation around the helical axis. (C and D) Pseudo-atomic model of the open state of the ParM filament. Red arrows mark the distances between residues 161–164 and 271–274 of the upper protomer, and the residues 212–217 of the lower protomer in both closed and open states. Green arrows mark the distances between residues 298–300 of the upper protomer, and residues 239–341 of the lower protomer in both structural states. Residues 33, 34, 36, and 40, which are crucial for filament maintenance, are shown as spheres in (A–D). Residue 123, involved in the interaction with ParR/ParC complex, is indicated in (A–D) with red arrow- heads. (E) A comparison between actin (cyan) and ParM (red) shows that while the cores of the two subunits are fairly well conserved, the peripheral regions in actin at the four ‘‘corners’’ of the subunit (responsible for protomer-protomer contacts in F-actin) have no correspondence with the secondary structural elements of ParM in these regions. Two residues (204 and 243) that have been implicated in actin polymerization (Rould et al., 2006) can be seen to be in a region that has no structural similarity in ParM. The hydrophobic plug on actin involves residues 264–273.

Figure 7. Structural Polymorphism of the ParM Filaments Depends on the Polymerization Conditions

EM micrographs of negatively stained ParM filaments formed at different conditions (A–F). Long filaments are formed in presence of AMP-PNP, and these filaments are stable even after several hours (A). In the presence of 5 mM ATP, shorter filaments are

observed after 5 min of polymerization (B), and very few filaments along with aggregates are present after 30 min (C). After 5 min of polymerization in the presence of 0.5 mM ATP, ParM forms short filaments that tend to form bundles (D), while after 30 min, when all ATP is depleted, only amorphous aggregates are seen (E). Addition of 1 mM BeF_3^- to 0.5 mM ATP preserves some filaments even after 30 min incubation (F). Two structural states are found in negatively stained filaments—closed (G) and open (H). These states are shown as gray transparent surfaces with docked crystal structure of ParM in the closed (G, red ribbons) or open (H, blue ribbons) states. The frequency of these states within the filaments shown in (A), (B), and (F) is shown in (I).

Figure 8. Model for the Dynamic Instability of ParM Filaments

ParM filament is shown as a stack of circles, where each circle represents a ParM protomer. Black circles represent ParM-ATP; gray circles represent ParM-ADP, and black circles with deleted center stand for the intermediate ParM-ADP-Pi state. Shortly after polymerization, ParM filament is composed of ATP subunits (A), which over time turn into ADP-Pi state (B) followed by the ADP state (C). The integrity of the filament in (A–C) is preserved by the ATP-cap. Inorganic phosphate release inhibits the formation of the protective ATP-cap (D). Finally, the ADP subunits are exposed (E), and the filament de-polymerizes (F).

Figure 1

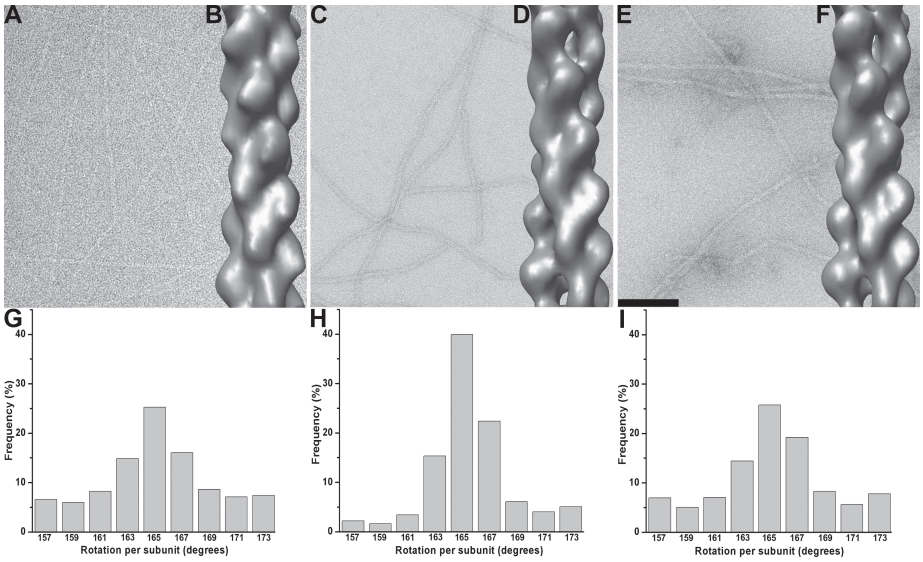
A
B
C
D
E
F
G
H
I
Frequency (%)
Rotation per subunit (degrees)
157 159 161 163 165 167 169 171 173
0 10 20 30 40

Figure 2

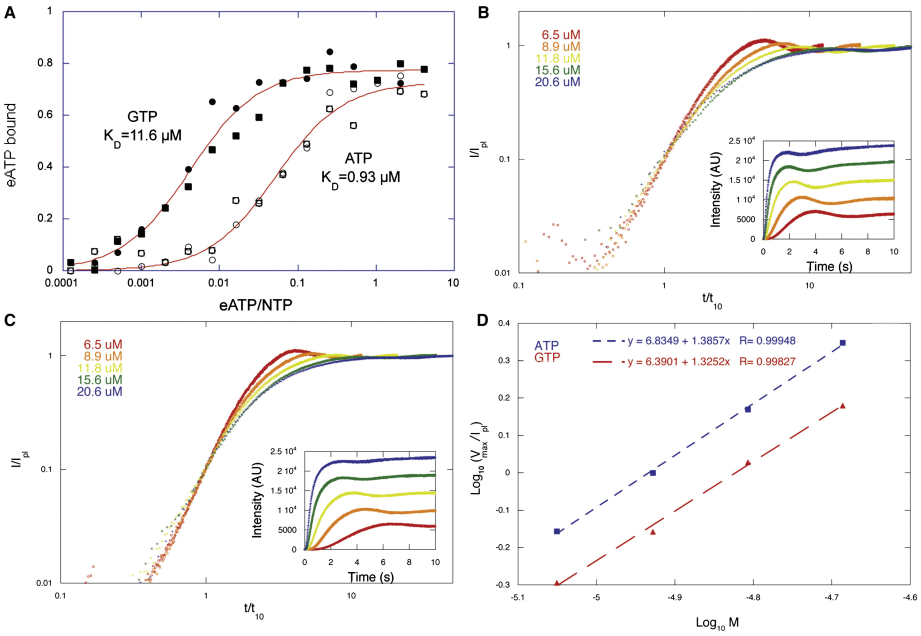
A
eATP bound
GTP
K_D=11.6 μM
ATP
K_D=0.93 μM
eATP/NTP
B
6.5 uM
8.9 uM
11.8 uM
15.6 uM
20.6 uM
I/I_pl
Intensity (AU)
Time (s)
t/t_10
C
6.5 uM
8.9 uM
11.8 uM
15.6 uM
20.6 uM
I/I_pl
Intensity (AU)
Time (s)
t/t_10
D
ATP
GTP
y = 6.8349 + 1.3857x R= 0.99948
y = 6.3901 + 1.3252x R= 0.99827
Log10 (V_max /I_pl)
Log10 M

Figure 3

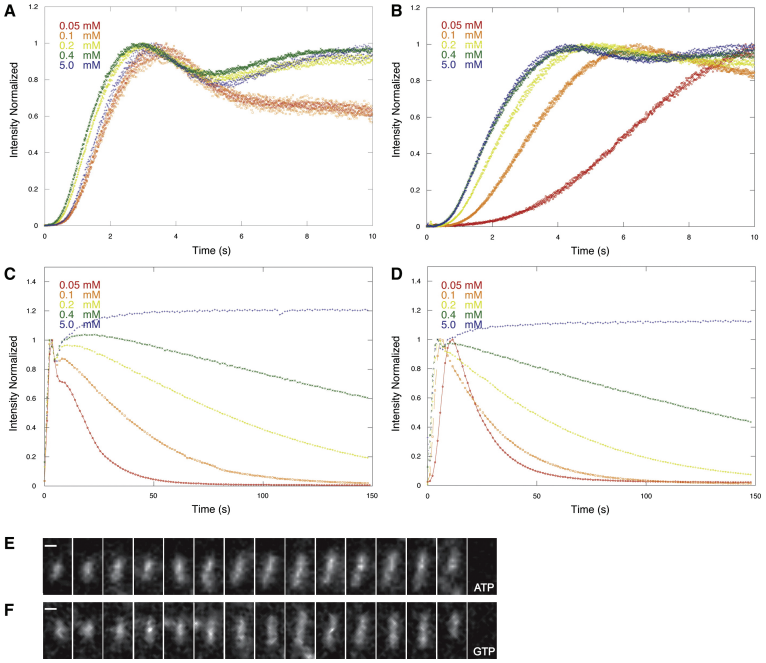
A
B
C
D
E
F
0.05 mM
0.1 mM
0.2 mM
0.4 mM
5.0 mM
Intensity Normalized
Time (s)
ATP
GTP

Figure 4

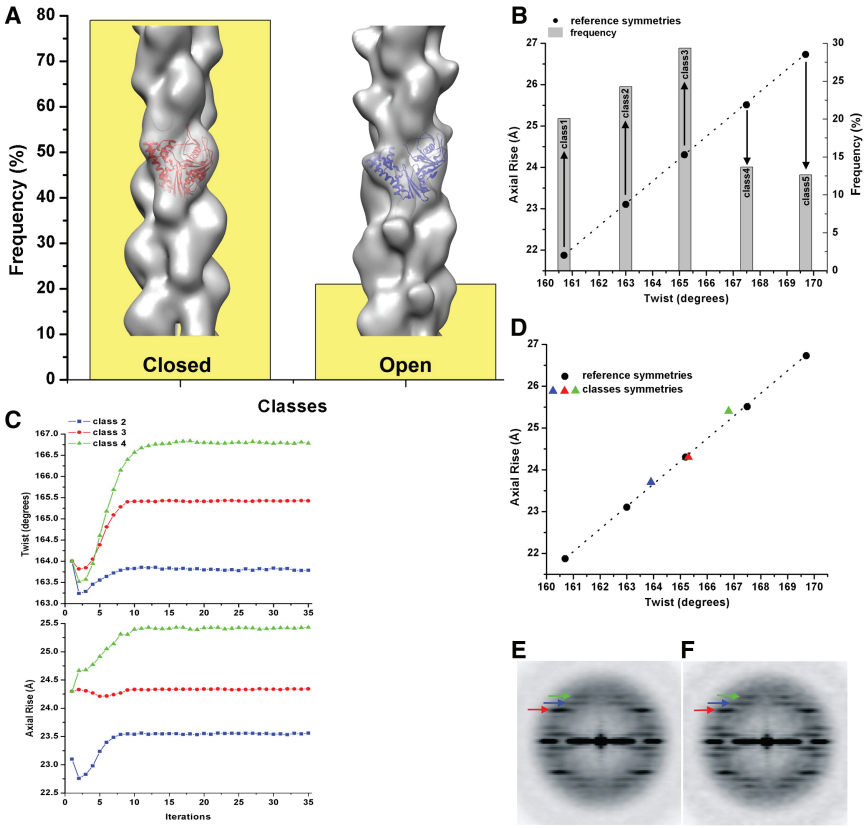
A
Frequency (%)
Closed
Open
Classes
B
reference symmetries
frequency
Axial Rise (Å)
Frequency (%)
Twist (degrees)
class1
class2
class3
class4
class5
C
class 2
class 3
class 4
Twist (degrees)
Axial Rise (Å)
Iterations
D
reference symmetries
classes symmetries
Axial Rise (Å)
Twist (degrees)
E
F

Figure 5

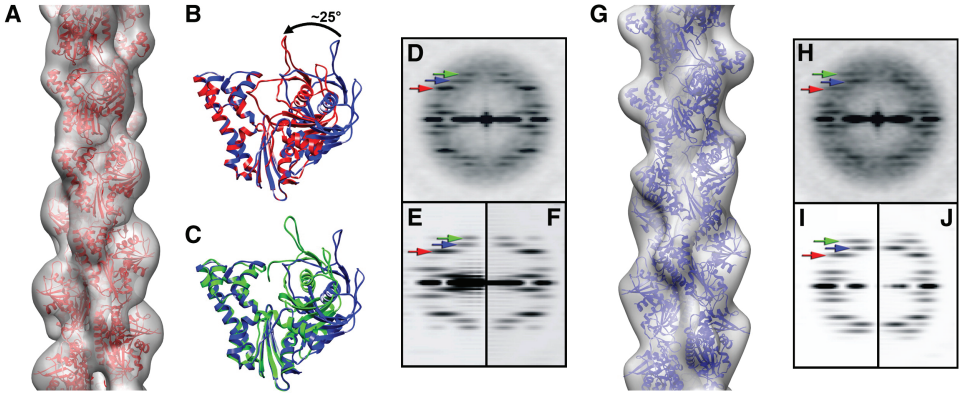

Figure 6

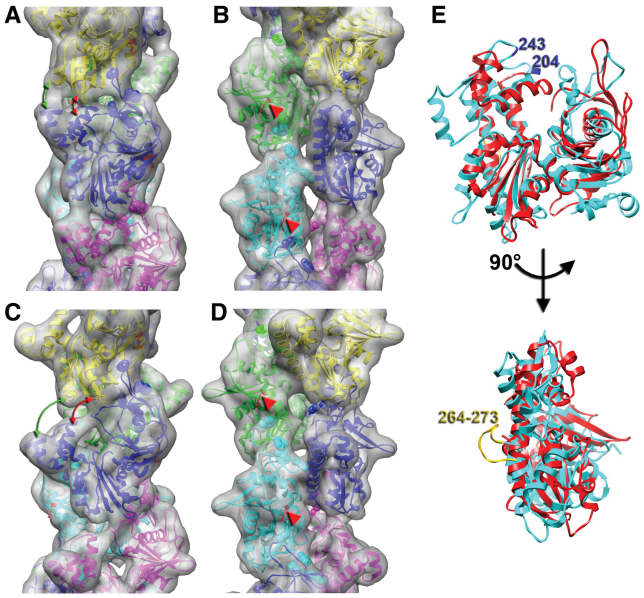

Figure 7

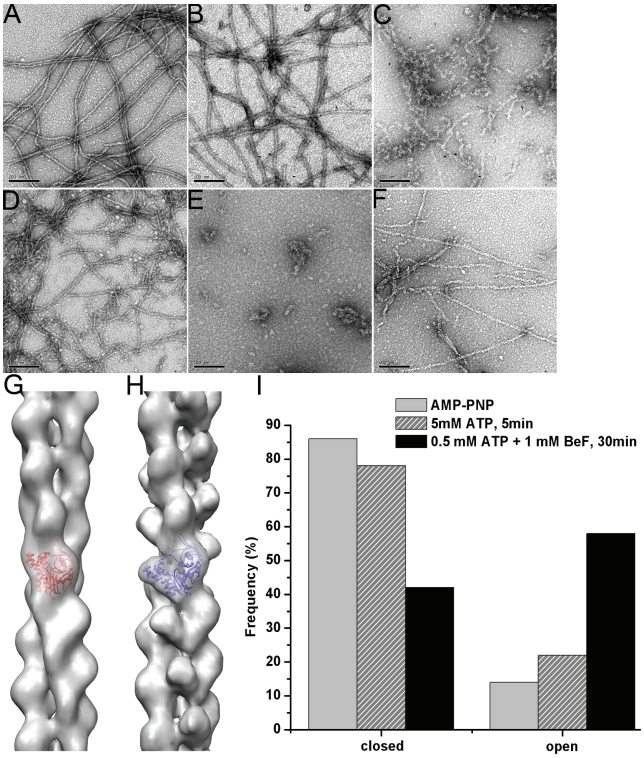
A
B
C
D
E
F
G
H
I
AMP-PNP
5mM ATP, 5min
0.5 mM ATP + 1 mM BeF, 30min
Frequency (%)
0
10
20
30
40
50
60
70
80
90
closed
open

Figure 8

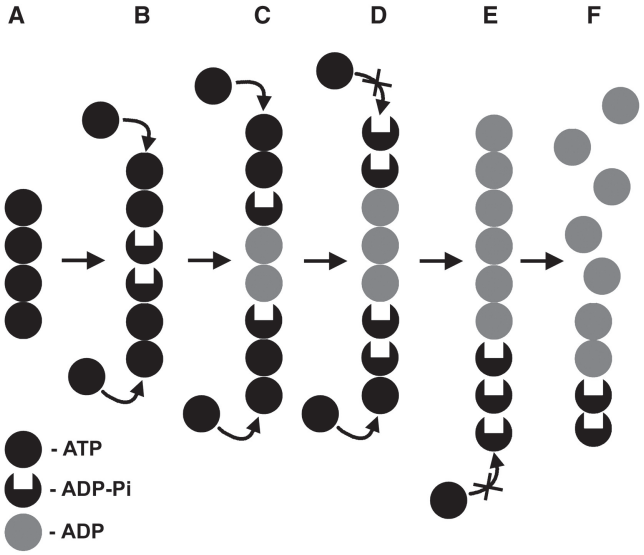

Supplemental Figure Legends

Figure S1.

The resolution of the closed state (A) and the open state (B) was determined using a conservative 0.5 criterion in the FSC approach (black curves). The similarity between the3D-reconstructions and the corresponding atomic models was assessed using FSC 0.5criterion (red curves). The drop in the correlation between the atomic models and the maps in the spatial frequencies of ~ 1/25 Å-1 arises from the drop in the contrast transfer function at the defocus values used for imaging (C, red asterisk).

Figure S2.

Convergence of the closed (top), and open (bottom) sets of ParM segments to their common solutions is robust. The result of the reconstruction procedure does not depend on either the starting model, or the starting symmetry, used in the iterative procedure.

Supplemental Figure 1

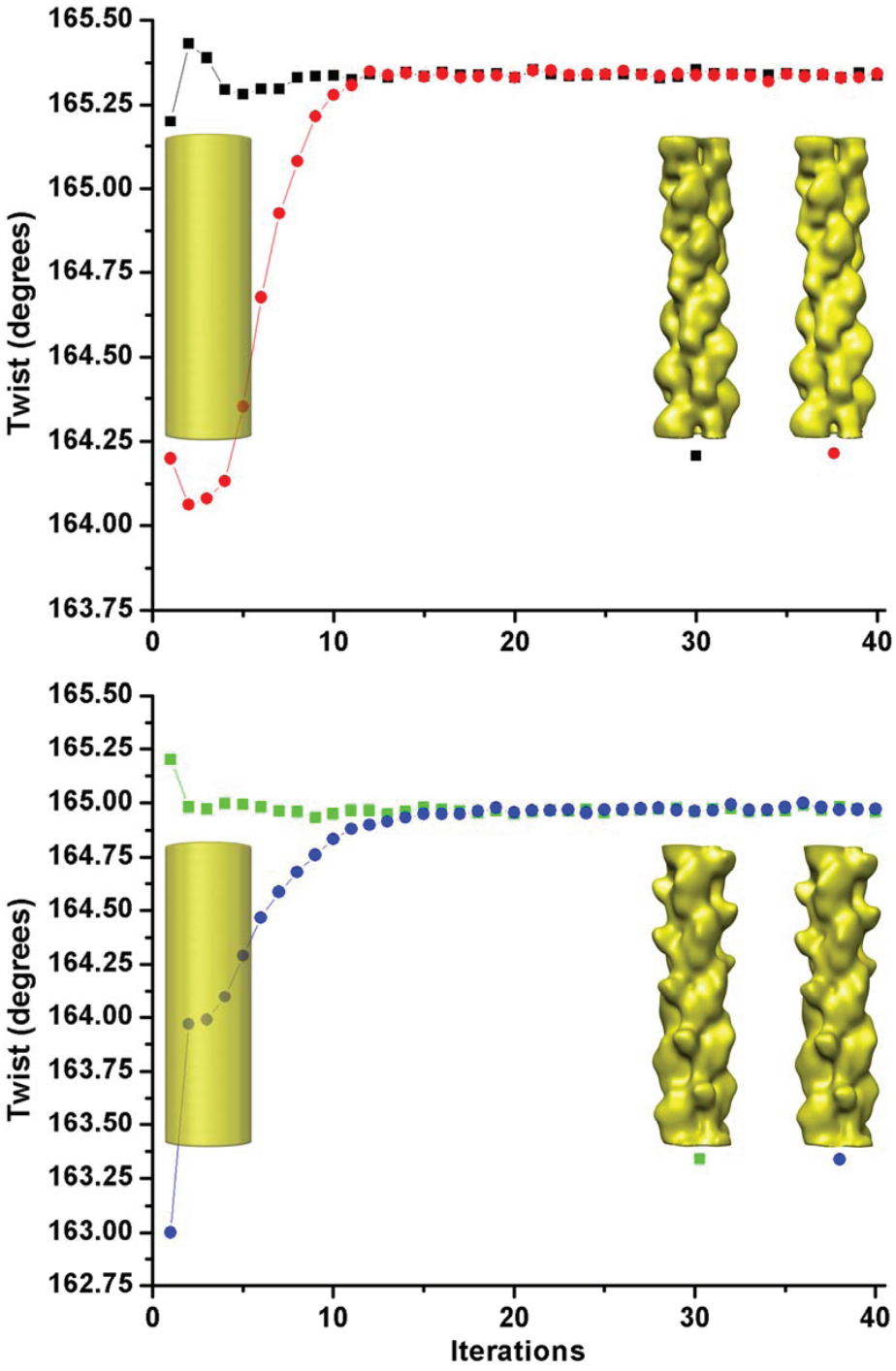

Supplemental Figure 2

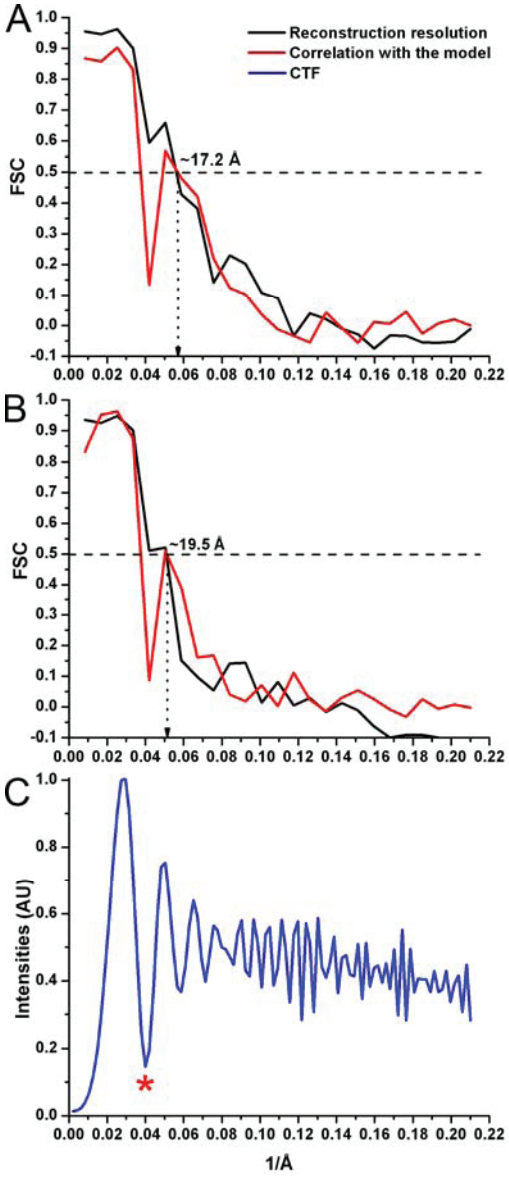

Chapter 5

Questions and Future Directions

Introduction

The intension of this chapter is to discuss current questions that we have been pursuing over the past year, the development of a single filament assay, preliminary results and future directions.

Reconstitution assays demonstrate that ParM and the ParRC complex form a very efficient mitotic spindle that is capable of separating beads *in vitro* and DNA *in vivo* (1, 2). Effective force generation relies on several properties that are intrinsic to the system: ParM filaments nucleate rapidly, elongate bilaterally and are dynamically unstable. ParM can bind to and push the ParRC complex via insertional polymerization, and the ParRC complex inhibits dynamic instability(2). The reconstitution assay demonstrates that these properties are essential, but does not explain how these properties work at a molecular level, therefore, several fundamental questions remain regarding the function of the system.

During the my last year of graduate school, in conjunction with my professor, I have been developing a new TIRF based assay to monitor single filament ParM dynamics and ParM filament-ParRC complex interactions with higher precision and higher temporal resolution. Briefly, in this assay, we attach biotinylated E148A ParM seeds to PEG:PEG-biotin passivated cover-glass using streptavidin, and polymerize monomeric ParM off these seeds, in the presence or absence of the ParRC complex. The remaining sections of the chapter discuss specific questions this assay is being used to address and some preliminary results.

What is the kinetic basis of ParM dynamic instability? How dynamic are the filaments? What are the polymerization and depolymerization rates of wild-type and E148A ParM filaments?

ParM filaments and microtubules ends exist in two states: ends that are stable and growing, or ends that are unstable and rapidly shrinking (3, 4). Nucleotide hydrolysis regulates the transition between these two states in both microtubules and ParM filaments (3, 4). Growing ends are thought to be protected by a filament end "cap", consisting of nucleotide bound protomers; loss of this cap by nucleotide hydrolysis leads to catastrophe (3, 4). In microtubules, catastrophe events are frequently followed by rescue events, however rescue events have not been observed in ParM filaments (3, 4). My professor, Dyche Mullins, has developed a mathematical model that predicts a discrete ParM cap size, and suggests that ParM filaments experience minor catastrophe events, which are followed by filament rescue, and major catastrophe, events, which are followed by complete filament depolymerization. These minor catastrophe events have not been observed in previous experiments, however they are predicted to reduce the elongation rates of wild-type ParM relative to E148 ParM in a ParM concentration dependent manner. To determine if minor catastrophe events exist and if they reduce the elongation rate of wild type ParM relative to E148A in a concentration dependent manner, we are monitoring the filament dynamics and measuring the elongation rates of wild type and E148A ParM polymerized of E148A seeds (Figure 1A).

How do ParM filaments move the ParRC complex?

ParM filaments use the energy generated by nucleotide hydrolysis and protein polymerization to mechanically push the ParRC complex in the direction of ParM filament elongation(2). ParM may move the ParRC complex by acting as a polymerization motor that directly pushes on complexes attached to its end, similar to how actin is thought to push formins, or ParM filaments may use nucleotide hydrolysis to bias the 2-D diffusion of side bound ParRC complex toward ATP bound protomers present at filament ends (5). These models have strong prediction for how fast ParRC should move relative to filament ends and where it will localize. We are using the filament assay to investigate single ParM-ParRC interactions (Figure 1B).

How does the ParRC complex stabilize ParM filaments?

Formally the ParRC complex may inhibit ParM catastrophe by acting as a scaffold that prevents depolymerization, or may inhibit nucleotide hydrolysis (5). We will use this assay in conjunction with phosphate release assays to investigate these models.

Figure Legends:

Figure 1. (A) Kymograph of 2.5μM 20% alexa-488 labeled ParM polymerized of E148A seeds illustrating filament dynamics. Seeds are in red and filament ends consisting of polymerizing monomer are in green. **(B) Montage visualizing single ParRC particles attached to the end of an E148A ParM filament.** Seeds are in red and filament ends consisting of polymerizing monomer are in green. The red sphere is a single ParRC complex.

References:

1. Møller-Jensen, J., Borch, J., Dam, M., Jensen, R. B., Roepstorff, P., and Gerdes, K. (2003) *Molecular Cell* **12**, 1477–1487
2. Garner, E. C., Campbell, C. S., Weibel, D. B., and Mullins, R. D. (2007) *Science* **315**, 1270–1274
3. Kueh, H. Y., and Mitchison, T. J. (2009) *Science* **325**, 960–963
4. Garner, E. C., Campbell, C. S., and Mullins, R. D. (2004) *Science* **306**, 1021–1025
5. Salje, J., Gayathri, P., and Löwe, J. (2010) *Nat Rev Micro* **8**, 683–692

Figure 1

1A

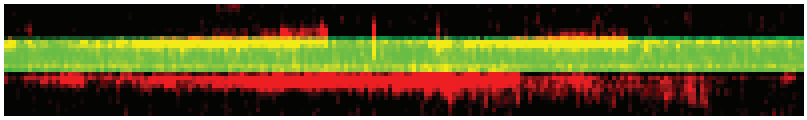

1B

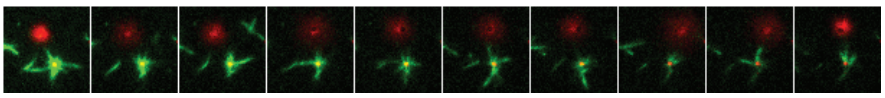

Publishing Agreement

It is the policy of the University to encourage the distribution of all theses, dissertations, and manuscripts. Copies of all UCSF theses, dissertations, and manuscripts will be routed to the library via the Graduate Division. The library will make all theses, dissertations, and manuscripts accessible to the public and will preserve these to the best of their abilities, in perpetuity.

Please sign the following statement:

I hereby grant permission to the Graduate Division of the University of California, San Francisco to release copies of my thesis, dissertation, or manuscript to the Campus Library to provide access and preservation, in whole or in part, in perpetuity.

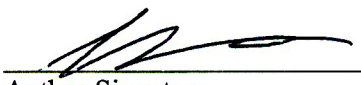

Author Signature

8/30/2011

Date